The numerical simulation of a three dimensional fluid sediment system on arbitrarily shaped domains

Dissertation

zur

Erlangung des Doktorgrades (Dr. rer. nat.)

der

Mathematisch-Naturwissenschaftlichen Fakultät

der

Rheinischen Friedrich-Wilhelms-Universität Bonn

vorgelegt von

Markus Burkow

aus

Cottbus

Bonn 2016

Angefertigt mit Genehmigung der Mathematisch-Naturwissenschaftlichen Fakultät der Rheinischen Friedrich-Wilhelms-Universität Bonn

1. Gutachter: Prof. Dr. Michael Griebel

2. Gutachter: Prof. Dr. Marc Alexander Schweitzer

Tag der Promotion: 30. Juni 2016

Erscheinungsjahr: 2016

To Hanna

Summary

Current driven sediment processes and their impact on the fluid system and on the morphology is of large interest in environmental as well as in engineering sciences. Here, the numerical simulation of the fluid flow and the related sedimentary processes helps to widen the insights and reduces the costs. There are two main parts needed for a successful and significant numerical simulation of a fluid sediment system. On the one hand one needs an efficient and robust flow solver which in turn is easily adjustable to a large variety of problems. And on the other hand a it is viable to achieve a physically correct modelling of the sediment transport and the morphological change of the sediment surface for an applicability to realistic examples.

In the first part of this thesis the existing three dimensional two phase Navier Stokes solver NaSt3D is extended by a new and variable geometry handling using a level set method. In each part of this approach the boundary conditions are set at geometries specified by a zero contour of a level set function. During the pressure projection method after Chorin (1968) Neumann boundary conditions are imposed at this zero contour and incorporated into the resulting linear system which is solved by a stabilized BiCG method. The newly developed incorporation of the Neumann boundary conditions as well as the stabilization of the linear system are employed efficiently in the parallel algorithm. For the velocities a new analogous discretization of the Dirichlet boundary conditions allows a second order discretization of the fluid velocities on arbitrarily shaped domains. Numerical convergence studies show satisfying convergence rates for the velocities as well as for the pressure. In two numerical simulations of realistic examples the applicability of the new approach is tested extensively.

The second part introduces a full current induced sediment model which includes the bed load transport and the suspension load transport. From the sediment transport results a morphological change of the sediment bed which is modellel by a bed level equation after Exner (1925). A mass conserving interchange between both sediment models is realized by boundary conditions as well as by sink and source terms near the boundary.

The whole model is discretized with high order finite difference schemes in space and time. Here, the setting follows the discretization schemes used in NaSt3D. As a further aspect a model which limits the angle of the slope is developed, discretized, and tested numerically. The coupling of the new fluid solver and the described sediment models including the slope limiter covers three parts. First, the sediment model is driven by the fluid velocities from the fluid solver. Second, the impact of the sediment concentration on the flow is realized by a Boussinesq approximation in the Navier Stokes equations. Third and finally, the change of the sediment surface due to the transport is mapped back onto the computational domain. To describes the sediment geometry in the fluid solver a level set function is constructed. Numerical convergence studies shows satisfying results for the coupled system.

Conclusively, three successive numerical examples demonstrate the wide range of applications for a full fluid sediment model for single phase flows as well as for two phase flows.

Content

1 Introduction

A thorough understanding of a moving fluid is essential to explain omnipresent processes. For example, the flow of a liquid like water induces forces which cause an erosion and a transport of the eroded material. The erosion and the transport affect the daily work in engineering and environmental sciences. If a bridge is constructed, the prediction of the impact of the structure on the river is crucial for the stability of the new bridge and for the whole river section. Additionally, the fundamental research in geosciences is engaged in the process oriented experimental research and has to identify and understand many complex fluid processes.

Therefore, the experimental research of fluid dynamics and its related phenomena are of importance in engineering, environmental, and industrial applications. On the one hand experiments in flumes are used to investigate the flow and its interaction with the surrounding under controlled conditions. On the other hand an extensive field research is necessary to provide empirical material parameters and to validate the conclusions taken from the flume experiments and vice versa. In both fields of research the fluid dynamics of the related processes are on focus. The investigation of these related processes intensifies the necessary effort. For instance, the current induced sediment transport, the resulting bed forms, the evolution of a sand dune or the erosion near a bridge pier require a deep understanding of the concurrently temporal and spatial processes.

In general, sediment transport consists of bed load transport and suspension load transport. The bed load transport comprises all material which is transported near the sediment surface. All other material is transported in the whole fluid body and is referred to as suspension load. If the velocities decrease, the transport decreases consequently and the previously transported material is deposited. This deposition leads to the formation of various morphological features. Dunes and scour marks are only two morphological features in which the deposition and erosion of the material come into effect. Beside the transport of the material the sediment specific angle of repose has to be taken into account. In this situation a granular medium forms a certain critical slope angle until

its slopes are stable. In all these considerations different space and time scales of the sedimentary processes and the fluid dynamics require a massive amount of material, financial, temporal, and personal cost. In this situation the numerical simulation is often used as an additional tool to widen the insights or to reduce the efforts used to design and conduct the experiments. Accompanied with that a numerical simulation is an auxiliary tool reducing the costs for these experiments. For this purpose a fast and reliable fluid solver in combination with a sediment model is necessary.

Fig. 1.1: Different scour marks on different scales. A scour is a depression eroded by a fluid flow and the scales for a scour reach from a few centimeters (top left) to several tens of centimeters (top right) to several meters (bottom).

In the first part of this work the basic numerical algorithm is builded by the two phase Navier Stokes solver NaSt3D developed by Griebel et al. (1998), Croce et al. (2004), Croce et al. (2009) and others. It was developed at the Institute for Numerical Simulation at the University of Bonn in the last two decades. In detail, NaSt3D uses the pressure projection after Chorin (1967) and high order finite difference discretization schemes to solve the

three dimensional two phase Navier Stokes equations on a regular cartesian staggered grid. During the projection method it is necessary to solve a discretized Poisson equation with homogeneous Neumann boundary conditions on an arbitrarily shaped domain. The domain and the obstacles are handled by a flag field technique which leads to a blocky approximation of complex structures. With the chosen domain decomposition the efficient parallelization of the algorithm is plain and simple. But the flag field approach does not converge for the surface normals at the boundaries of an arbitrarily shaped object, which in turn can destroy the convergence for homogeneous Neumann boundary conditions. In the following NaSt3D is improved such that a handling of complex obstacles is feasible and the fast and efficient implementation is retained. The idea to overcome the non convergence of the normals for the Neumann boundary conditions is to implement a level set representation for the obstacles to approximate the boundary normals. With this level set formulation the discretization of the homogeneous Neumann boundary conditions from the Poisson problem is incorporated into the matrix which arises from its discretization. Additionally, a required null space stabilization of the linear system is employed and solved by a stabilized BiCG method. Overall a convergence study at the boundary as well as in the inner domain for the Poisson equation proves the functionality of the approach. In the next step these ideas to impose the boundary conditions at an obstacle described by a level set function are pursued. Dirichlet boundary conditions are implemented for the velocities in the prediction and correction step of Chorin's method. A numerical convergence study with a spherical obstacle tests the approximation of the boundary conditions for the velocities. Due to the absence of an analytic solution of the Navier Stokes equations an overkill solution on a very fine grid is used as a reference solution. A systematic testing of the numerical algorithm illustrates its capabilities in the single phase flows as well as in the two phase flows and in combination with level set obstacles.

The second part of this thesis discusses the sediment models, the slope angle model, their implementations, and the coupling with the Navier Stokes solver from the first part. First, the modeling of the morphological change of the sediment surface due to bed load and suspension load is explained. Here, a bed level equation after Exner (1925) models the sediment bed height which changes accordingly to the sediment mass balance. Moreover, the transport of the suspended material is described by an advection diffusion equation for a sediment concentration. In addition to this advection diffusion model a gravitational settling term is added. So, a settling of the particles caused by the

gravitation is regarded. The mass interchange between both models is realized by specific sink and source terms at the boundaries which ensure that the mass is conserved. Both models are discretized by finite difference schemes on a staggered grid. At this point, the implementation follows the basic setting of NaSt3D. Beside the transport of the particles another phenomena correlated with granular media has to be modelled. Since it is impossible to pile up a granular medium arbitrarily high, a gravitational movement of the particles has to be considered. If a certain point with a specific angle of repose is reached, surplus masses slide downhill until a specific angle of repose is formed. To model this sliding behaviour, a heat equation is modified. In detail, the coefficient in the heat equation depends on the angle of the slope and therefore on the gradient of the sediment height. Thus, the heat equation transforms into a nonlinear time dependent model with a discontinuous coefficient. After that, its discretization and implementation are discussed in detail. Conclusively, a numerical convergence study verifies the implemented slope limiting algorithm.

After the description of the Navier Stokes solver and the sediment models the coupling between both is presented. Thereby, the coupling strategies are introduced shortly, followed by the extensive explanation of the loose partitioned coupling of NaSt3D with the sediment models. In this setting the time step restrictions for each instationary model in the coupling are introduced. On the one hand the impact of the suspension concentration on the fluid is covered by a Boussinesq approximation in the momentum equation of the Navier Stokes equations. On the other hand the change of the sediment bed changes the fluid domain, which is realized by a remapping of the calculated sediment surface onto the fluid domain. The functionality and the implementation are tested in a numerical convergence study for the fully coupled fluid sediment system with geometries treated by the level set approach.

Conclusively, several numerical simulations show the applicability of the developed algorithms to realistic phenomena from engineering as well as from geosciences. First, a single phase flow and the evolution of a scour mark under clear water conditions are studied. In this example the sediment bed changes due to the bed load transport that allows to study the functionality of the mapping of a new fluid domain. To document the wide range of the resolved features, the temporal evolution of the sediment as well as the flow conditions are illustrated in various visualizations of the simulation. Moreover, the magnitude of the erosion near the step and the cylindrical obstacle are presented in time dependent plots. Second, the full sediment model including the transport of the

suspension load is applied to the evolution of a barchanoid dune. In this experiment an initially cross pile of sand transforms into a crescent shaped dune body. The visualizations of the suspended material and the sediment bed demonstrate the development over time. A qualitatively comparison of the dune cross sections with results from the literature emphasizes the plausibility of the approach. Third and finally, a two phase example with a flow round two cylindrical and one rectangular obstacle concludes the numerical examples. Here, a set of bridge piers serves as a model in this example. Plausible results are taken from the simulation for the free fluid interface as well as from the simulation for the sediment bed beneath the surface.

Outline

The remainder of this thesis is organized as follows. The first part focuses on the the solution of the two phase Navier Stokes equations on arbitrarily shaped obstacles. Here, the projection technique after Chorin (1967) and its implementation in NaSt3D are explained in the second chapter. Therein, the used discretization schemes and the handling of the geometry by the so called flag field approach described in Griebel et al. (1998) are reviewed as the basis for the improvements made in this thesis. The third chapter discusses the solution of the Poisson equation with homogeneous Neumann boundary conditions on an arbitrarily shaped level set domain. Following this technique an approach to impose Dirichlet boundary conditions for the velocities at the obstacles is presented in the fourth chapter. Conclusively, the fifth chapter presents an extensive numerical convergence study and two numerical experiments. In the second part a full sediment model is introduced for the bed load as well as for the suspension load. The sixth chapter describes the two models, their parameters, and the interchange of the transported material. Moreover, the discretization of the presented sediment model is explained. Chapter seven describes the slope limiting algorithm deduced from basic geometrical considerations and a numerical convergence study. The loose partitioned coupling of the two phase Navier Stokes solver from the first part with the full sediment model is discussed and investigated in the eighth chapter. Several numerical examples in the ninth chapter demonstrate the applicability of the full algorithm to a wide range of examples. A summary and a short outlook are given in the last chapter.

Part I

A second order discretization of the two phase Navier Stokes equations on arbitrarily shaped domains

2 Discretizing and solving the Navier Stokes equations on complex geometries

In the following chapter the Navier Stokes equations and the discretization in NaSt3D, as the basic fluid solver, will be described. Here, the notation follows the official description of the problem by Fefferman (2000) from the Clay Mathematics Institute. First, the general form of the momentum equation and the continuity equation for a single phase fluid are introduced. Second, the two phase model for two interacting incompressible fluids separated by a sharp interface is described. The transient incompressible Navier Stokes equations for a single phase read as

$$\frac{\partial u_i}{\partial t} + \sum_{j=1}^{n} u_j \frac{\partial u_i}{\partial x_j} = \nu \sum_{j=1}^{n} \frac{\partial^2}{\partial x_j^2} u_i - \frac{\partial p}{\partial x_i} + f_i(x,t) \qquad x \in \mathbb{R}^n, 0 \leq t \tag{2.1}$$

$$\sum_{i=1}^{n} \frac{\partial u_i}{\partial x_i} = 0 \qquad x \in \mathbb{R}^n, 0 \leq t \tag{2.2}$$

where $x \in \mathbb{R}^n$ describes the position, $u(x,t) = (u_i(x,t))_{1 \leq i \leq n)} \in \mathbb{R}^n$ denotes the velocities and $p(x,t) \in \mathbb{R}$ denotes the pressure, and the time is denoted by $0 \leq t$. Additional forces on the fluid, for example the gravity, are described by f_i. Furthermore, the initial condition $u(x,0) = u^0(x) \quad x \in \mathbb{R}^n$ is applied to the system of equations (2.1) and (2.2). As the initial velocity $u^0(x)$ a C^∞ divergence free velocity field is used. The parameter $\nu = \mu/\rho$ denotes the kinematic viscosity with the dynamic viscosity μ and the density denoted by ρ. In summary, both equations result from first principles, where the equation (2.1) represents Newton's law for a fluid volume under the forces of f_i. The second equation (2.2) constitutes the continuity equation under the assumption of a constant density ρ. For $n = 3$ the existence and uniqueness of a solution is unknown and one of the

millenium problems (Fefferman, 2000). Therefore, the Navier Stokes equations have been a challenging topic of research for the last century. With no claim of completeness, a small selection of work in literature follows Leray (1934), Hopf (1950), Ladyzhenskaya (1969), Kato (1972), Temam (1977), Kato (1984), Masuda (1984), Farwig (1992), Galdi (1994), Amann (2000), Amann (2003), Farwig et al. (2007) and Feireisl & Novotný (2012).

A common practice is to use the dimensionless Navier Stokes equations for single phase flows. Here, the reference value for the characteristic length d, the velocity u_∞ and the viscosity ν are used to dedimensionalize the Navier Stokes equations. Its dimensionless version on a fluid domain $\Omega_f \subset \mathbb{R}^3$, written in vector calculus notation reads

$$\frac{\partial u}{\partial t} + (u \cdot \nabla)u = \frac{1}{Fr} g - \nabla p + \frac{1}{Re}\Delta u \qquad \text{in} \quad \Omega_f \in \mathbb{R}^3, \tag{2.3}$$

$$\nabla \cdot u = 0 \qquad \text{in} \quad \Omega_f \in \mathbb{R}^3. \tag{2.4}$$

Here, the gradient and the Laplace operators are defined as follows

$$\nabla = \left(\frac{\partial}{\partial x_1}, \frac{\partial}{\partial x_2}, \frac{\partial}{\partial x_3} \right), \qquad \Delta = \nabla \cdot \nabla = \sum_{i=1}^{3} \frac{\partial^2}{\partial x_i^2}.$$

The dimenionless Reynold's and Froude's number are defined as

$$Re = \frac{\|u_\infty\|_2 \cdot d}{\nu}, \qquad Fr = \frac{\|u_\infty\|_2}{\sqrt{\|g\|_2 \cdot d}}$$

where the characteristic length and velocity are denoted by d and u_∞. And the domain Ω_f is a compact subset of $\mathbb{R}^3$ and has a continuous boundary $\Gamma_{\Omega_f} = \Gamma_1 \cup \ldots \cup \Gamma_m$ which is the compact union of m boundary sets Γ_i with $i = 1 \ldots m$. On each of this subsets different boundary conditions can be specified. Dirichlet boundary conditions which specify the velocity u_D at the boundary of the fluid domain Ω are defined by

$$u|_{\Gamma_D} \stackrel{!}{=} u_D. \tag{2.5}$$

Setting $u_D = 0$ results in an adhering wall, whereas $u_D = u_{in}$ defines a velocity at the boundary, for example inflow boundary conditions are realized in this manner. In contrast to the Dirichlet boundary conditions, the Neumann boundary conditions determine a value g for the gradient of the velocity u both in the normal direction n and in the

tagential direction τ which read as

$$\left.\frac{\partial u}{\partial n}\right|_{\Gamma_N} \stackrel{!}{=} g_n \qquad \left.\frac{\partial u}{\partial \tau}\right|_{\Gamma_N} \stackrel{!}{=} g_\tau. \tag{2.6}$$

Herewith, a frictionless domain can be realized by setting $g_\tau = 0$. Another typical example for a Neumann boundary condition is to set $g_n = 0$ and $g_\tau = 0$ achieving an open boundary for an inflow and outflow boundary. Beside the spatial boundary condition a velocity field as an initial condition $u(0, x) = u^0$ is necessary. In this setting the incompressibility condition results from a constant fluid density ρ. Applying this to two fluids, the two phase Navier Stokes equations have to include two different fluid densities and viscosities ρ_l and ν_f respectively for the liquid phase and for the gas phase ρ_g and ν_g. The two phase Navier Stokes equations describe two immiscibile fluids with a sharp interface where the surface tension is active. Note here, that in the following the notation „liquid“ and „gas“ phase is used for simplicity. Independently, both phases can be every incompressible fluid. Under the assumption of the immiscibility of the two fluids the Navier Stokes equations can be applied to a system of two fluid phases interacting with each other. Systems containing oil and water are examples for two incompressible newtonian fluids affecting each other only by the surface tension at the interface of both fluids. This interaction is modelled by an additional surface force depending on the curvature of the interface and acting strictly on the interface. In summary, the two phase immiscibile incompressible Navier Stokes equations read as follows

$$\rho(x)(\partial_t u + (u \cdot \nabla)u) = \nabla \cdot (\mu(x)S) - \nabla p - \sigma(x)\kappa(x)n(x) + \rho(x)f \tag{2.7}$$

$$\nabla \cdot u = 0 \tag{2.8}$$

where the fluid stress tensor S is defined as

$$S := \nabla u + (\nabla u)^T. \tag{2.9}$$

Additionally, $\mu(x)$ denotes the dynamic viscosity of the fluid at the position $x \in \mathbb{R}^3$. In contrast to the single phase Navier Stokes equations (2.3) and (2.4), the density $\rho(x)$ also depends on the position x in the fluid domain. The curvature κ and the surface tension σ are intrinsic values of the fluid and the interface and act only at the interface Γ_f in normal direction $n(x)$. This method has been introduced by Brackbill et al. (1992) as

the continuum surface force method which introduces an additional force at the interface generated by the surface tension. With the surface tension σ_f for the interface between both fluids, for instance $\sigma_f = 0.072N/m$ for an interface between water and air, the function $\sigma(x)$ is defined as

$$\sigma(x) = \begin{cases} \sigma_f & x \in \Gamma_f \\ 0 & x \notin \Gamma_f \end{cases}. \tag{2.10}$$

To model two incompressible fluids the continuity equation (2.4) has to be fulfilled in each phase. The numerical treatment of the two phase Navier Stokes equations and the handling of the surface tension effects are discussed in numerous works, compare Mulder et al. (1992), Sussman et al. (1994), Sussman & Puckett (2000), Croce (2002), van der Pijl et al. (2005), Sussman et al. (2007), Croce et al. (2009), Croce (2010), or Griebel & Klitz (2013). Moreover, the Navier Stokes equations need boundary conditions (2.5) and (2.6) in the whole fluid domain $\Omega_f = \Omega_l \cup \Omega_g \cup \Gamma_f$. Hence, the Navier Stokes equations on the fluid domain Ω with boundary conditions are summarized in the following way

$$\begin{aligned} \rho(x)(\partial_t u(x,t) + (u(x,t)\cdot\nabla)u(x,t)) &= \nabla\cdot(\mu(x)S) - \nabla p(x,t) && (2.11)\\ &\quad - \sigma(x)\kappa(x)n(x) + \rho(x)f(x,t) \\ S &= \nabla u(x,t) + (\nabla u(x,t))^T && (2.12)\\ \nabla\cdot u(x,t) &= 0 && (2.13)\\ u(x,t)|_{\Gamma_D} &\overset{!}{=} u_D && (2.14)\\ \left.\frac{\partial u(x,t)}{\partial n}\right|_{\Gamma_N} &\overset{!}{=} g_n && (2.15)\\ \left.\frac{\partial u(x,t)}{\partial \tau}\right|_{\Gamma_N} &\overset{!}{=} g_\tau && (2.16) \end{aligned}$$

$\forall\, x \in \Omega_f \subset \mathbb{R}^3$, $\forall\, 0 \le t$ with $\Omega_f = \Omega_l \cup \Omega_g \cup \Gamma_f$, and $\Gamma_{\Omega_f} = \Gamma_D \cup \Gamma_N$

$$\sigma(x) = \begin{cases} \sigma_f & x \in \Gamma_f \\ 0 & x \notin \Gamma_f \end{cases} \tag{2.17}$$

In the following the discretization and the solution of the equations (2.17) are presented, while the handling of complex arbitrarily shaped geometries is on focus. Moreover, due to the use of the pressure projection of Chorin (1967) a Poisson problem with homogeneous Neumann boundary conditions has to be discretized and solved on these geometries.

2.1 Solving the Navier Stokes equations with Chorin's pressure projection method

This section describes the pressure projection method for solving the Navier Stokes equations after Chorin (1968). Here, the notation was adapted as it is used in the Navier Stokes solver NaSt3D which is described in the next section. In the short notation all spatial and temporal dependence are omitted. Therefore, the three dimensional two phase equations read

$$\rho_f(\partial_t u + (u \cdot \nabla)u) = \nabla \cdot (\mu_f(\nabla u + (\nabla u)^T)) - \nabla p - \sigma\kappa n + \rho_f g \tag{2.18}$$

$$\nabla \cdot u = 0 \tag{2.19}$$

where $\rho_f = \{\rho_l, \rho_g\}$ denotes the density and $\mu_f = \{\mu_l, \mu_g\}$ describes the viscosity in each fluid phase. Given a divergence free velocity field u^n at the time step t^n, the pressure projection method after Chorin (1968) is sketched like

1. Set the boundary conditions for u^n according to (2.17).

2. Compute u^* on Ω_f

$$u^* = u^n + dt\left((u^n \cdot \nabla)\, u^n + \frac{\mu_f}{\rho_f}\Delta u^n - \frac{\sigma\kappa n}{\rho_f} + g\right) \tag{2.20}$$

   It should be noted that the pressure p is omitted.

3. Calculate the right hand side for the Poisson problem $f_p = \frac{1}{dt}\nabla \cdot u^*$ on Ω_f.

4. Solve the Poisson problem for p^{n+1}

$$\nabla \cdot \left(\frac{1}{\rho_f}\nabla p^{n+1}\right) = f_p \tag{2.21}$$

   on Ω_f with homogeneous Neumann boundary conditions $\partial p/\partial n = 0$ on Γ.

5. Correct u^* with the gradient of p^{n+1} to achieve a divergence free velocity field u^{n+1} on Ω_f by

$$u^{n+1} = u^* - dt\frac{1}{\rho_f}\nabla p^{n+1}. \tag{2.22}$$

Note here, that the values for the viscosity μ_f and the density ρ_f are constant in each fluid phase and discontinious across the interface. In the second step an intermediate velocity u^* is calculated, where the pressure gradient ∇p^n is omitted. An explicit time integration scheme is used to predict the velocity u^* from the old velocities from u^n. To illustrate the method an explicit first order Euler scheme is used. Other schemes like higher order Runge-Kutta schemes are possible. To correct the intermediate velocity u^*, such that u^{n+1} fulfills the divergence free condition, the divergence operator is applied to

$$u^{n+1} = u^* - dt\frac{1}{\rho_f}\nabla p^{n+1} \tag{2.23}$$

which leads to

$$\nabla \cdot \left(\frac{1}{\rho_f}\nabla p^{n+1}\right) = \frac{1}{dt}\nabla \cdot u^*. \tag{2.24}$$

Therefore, a Poisson problem equipped with homogeneous Neumann boundary conditions has to be solved for the new pressure p^{n+1}. Solving this linear system leads to p^{n+1} which is used to correct the intermediate velocity u^* such that u^{n+1} is a divergence free velocity field

$$u^{n+1} = u^* - dt\frac{1}{\rho_f}\nabla p^{n+1}. \tag{2.25}$$

With this approach the solution of the Navier Stokes equations is reduced to the problem of solving a linear system. The properties of the matrix depend on the discretization techniques for the Poisson problem, but for standard finite differences and finite element discretization the resulting matrix has advantageous properties like sparsisity, semi-definiteness or symmetry. Therefore, the application of an appropriate linear solver is the most challenging part in the solution approach for the system (2.18) and (2.19). Here, NaSt3D provides conjugate gradient methods like a Jacobi preconditioned CG-Method as well as a stabilized BiCG method (van der Vorst, 1992). Additionally, an algebraic multigrid method is available which is applied as a preconditioner for the Poisson matrix (Metsch (2013)).

2.2 Discretization and implementation

The code package NaSt3D and its further enhancements have been developed over the last two decades. Next, the basic concepts and details are discussed. Generally, the Navier Stokes equations (2.18), (2.19), the variables $u = (u, v, w)$, and p are discretized with

finite differences on a staggered cartesian grid. The velocity components are situated at the cell faces, whereas all scalar values like the pressure p or the density ρ_f are situated at the cell midpoints. A cell is defined as the volume $[(i-1)dx, i\,dx] \times [(j-1)dy, j\,dy] \times [(k-1)dz, k\,dz]$, and the position of the variables is defined as

$$u_{ijk} = u(i\,dx, (j-\frac{1}{2})dy, (k-\frac{1}{2})dz) \tag{2.26}$$

$$v_{ijk} = v((i-\frac{1}{2})dx, j\,dy, (k-\frac{1}{2})dz) \tag{2.27}$$

$$w_{ijk} = w((i-\frac{1}{2})dx, (j-\frac{1}{2})dy, k\,dz) \tag{2.28}$$

$$p_{ijk} = p((i-\frac{1}{2})dx, (j-\frac{1}{2})dy, (k-\frac{1}{2})dz). \tag{2.29}$$

Additional scalar variables are discretized at the same position like the pressure p, that is in the middle of the cell, compare Figure (2.2). In NaSt3D the finite differences dis-

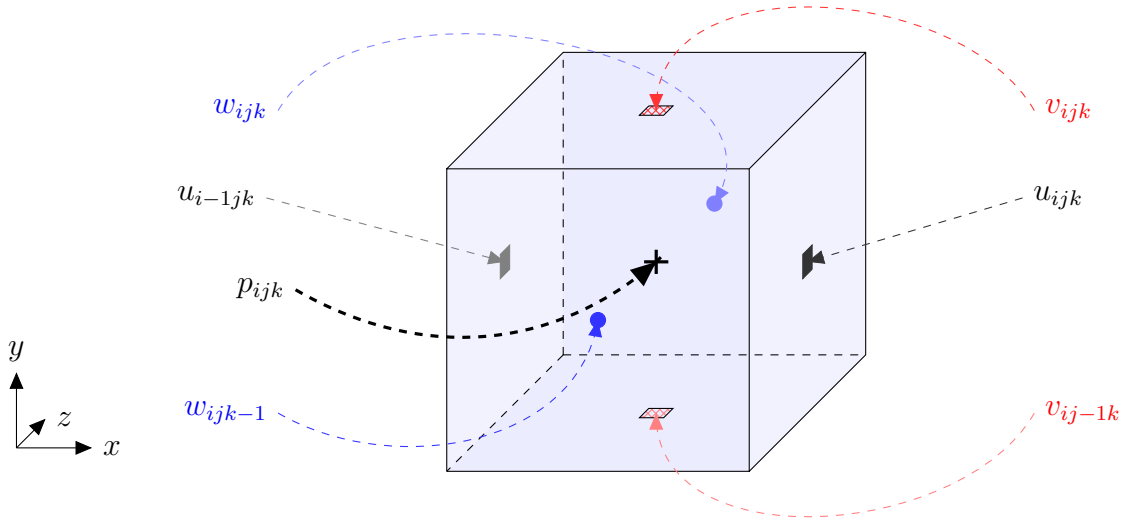

Fig. 2.1: Positions of the variables in the Navier Stokes equations on a three dimensional staggered grid. The velocities are placed on the faces of the cell. All scalar values like the pressure p_{ijk} are situated in middle of the cell.

cretization of the Navier Stokes equations on a staggered grid avoids oscillatory effects which would lead to instabilities and unphysical behaviour. For the spatial terms in (2.18) and (2.19) high order schemes are provided (SMART, QUICK, VONOS, WENO) and the temporal parts are discretized by explicit time integration schemes like a first

order Euler, a second order Adams-Bashforth, or a third order Runge-Kutta). Arbitrarily shaped obstacles are realized by a geometry approximation which follows the rectilinear grid cells. The so called flag field technique approximates obstacles by blocks with the minimum size of one cell. Figure (2.2) demonstrates an exemplary approximation of an irregular shaped obstacle by the flag field approach. The boundary conditions at the obstacles are applied by interpolation of a value for the obstacle cells from the adjacent fluid values. Thus, up to interpolation accuracy the conditions at the obstacle boundary are fulfilled. Further details about the discretization and the geometry approximation techniques used in NaSt3D are given in Griebel et al. (1998), Croce (2002), and Croce et al. (2009). The whole algorithm is parallelized by a domain decomposition approach,

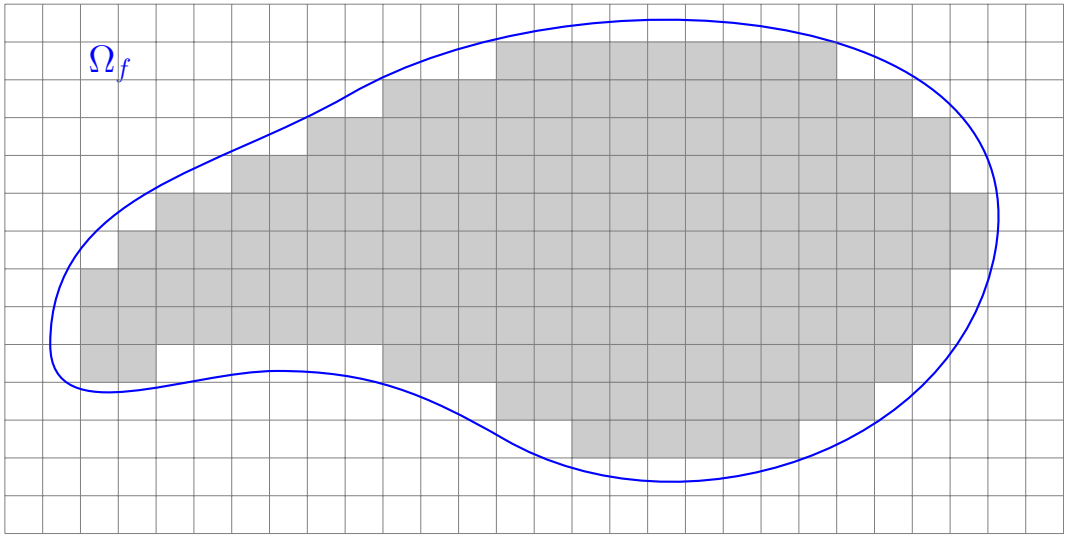

Fig. 2.2: Approximation of a two dimensional arbitrarily shaped smooth obstacle (blue). The gray blocks are obstacle cells. The flag field approach approximates obstacles by grid aligned blocks. Combined with the staggered grid discretization the flow variables (u, v, w) are situated on the boundary faces of the blocks.

where the neighboring cells has to interchange several layers of their boundary cells. The communication routines are implemented with MPI (message parsing interface) resulting in an efficient and well scaling algorithm. The scaling was investigated in several publications, for instance Griebel & Zaspel (2010) and Griebel & Rüttgers (2014). As a turbulence model the sub grid scale approach with a wall law is introduced which was proposed by Smagorinsky (1963) and Van Driest (1956). For two phase flows the

free surface is tracked by a level set function $\phi(x)$, which is a signed distance function $\phi : \mathbb{R}^3 \to \mathbb{R}$ and is defined as

$$\phi(x) = \begin{cases} < 0 & x \in \Omega_1 \\ = 0 & x \in \Gamma \\ > 0 & x \in \Omega_2 \end{cases} \qquad \text{with } \|\nabla\phi(x)\|_2 = 1. \tag{2.30}$$

Here, Ω_1 and Ω_2 define two domains separated by the zero contour of the level set function $\Gamma = \{x \in \Omega \,|\, \phi(x) = 0\}$. In the case of a two phase fluid the liquid and the gas phases are used here. The requirement $\|\nabla\phi(x)\|_2 = 1$ is called Eikonal equation and describes an intrinsic feature of a signed distance function. Given a rough estimate of a signed distance function $\phi^*(x)$ which defines a zero contour $X_0 = \{x \in \Omega_f \,|\, \phi^*(x) = 0\}$, a correct level set function ϕ with the same zero contour can be computed by solving the Hamilton-Jacobi equation

$$\frac{\partial\phi}{\partial\tau} = sgn(\phi_0)\,(1 - \|\nabla\phi\|_2) \qquad \text{with } \phi_0 = \phi^*(x), \tag{2.31}$$

where τ denotes a pseudo time. This equation can be solved up to a pseudo end time or until a fix point is reached. If a fix point is reached, the distance property and the Eikonal equation are fulfilled. Here, the fifth order WENO scheme and the third order Runge-Kutta method provide a robust and reliable discretization of the free surface. Following this method a level set function ϕ with sufficiently good distance property is provided by the solution of the equation (2.31).

All phase intrinsic parameters in the Navier Stokes equations, like ρ and μ, are smoothed as follows

$$\rho(\phi(x)) = \rho_2 + (\rho_1 + \rho_2)h(\phi(x)) \tag{2.32}$$

$$\mu(\phi(x)) = \mu_2 + (\mu_1 + \mu_2)h(\phi(x)) \tag{2.33}$$

in a band near the fluid interface with bandwidth ϵ by a heaviside function

$$h(\phi(x)) = \begin{cases} 0 & -\phi(x) > \epsilon \\ \frac{1}{2}\left(1 + \frac{\phi(x)}{\epsilon} + \frac{1}{\pi}\sin(\frac{\pi\phi(x)}{\epsilon})\right) & |\phi(x)| \le \epsilon \\ 1 & \phi(x) > \epsilon \end{cases}. \tag{2.34}$$

This techniques and the typical level set methods used in NaSt3D are described in Sussman et al. (1994), Osher & Fedkiw (2003), Croce et al. (2009), and Croce (2010). For further information about the Navier Stokes solver NaSt3D and its applicability, compare Griebel et al. (1998), Boeker et al. (2001), Croce (2002), Croce et al. (2004), Verleye et al. (2006), Strybny et al. (2006), Croce et al. (2009), Croce (2010), Griebel & Zaspel (2010), Zaspel & Griebel (2013), Griebel & Klitz (2013), Griebel & Rüttgers (2014), Adelsberger et al. (2014), Klitz (2014), Burkow & Griebel (2015), Rüttgers et al. (2015), and Zaspel (2015).

In summary, NaSt3D as a three dimensional two phase flow solver is an efficient and well tested setting. NaSt3D was tested in many applications and applied to academic as well as engineering questions. The idea will be to use this algorithm to solve a physically correct fluid flow and couple it to the problem of sediment transport. Therefore, the geometry handling in NaSt3D will be replaced by a more sophisticated approach in this thesis. And a detailled explanation and discussion of the new handling is on focus in the next chapters.

3 Solving the Poisson problem on arbitrarily shaped geometries

This chapter describes the methods which are applied to solve the Poisson problem which arises from the pressure projection method from Chorin (1968) applied to the Navier Stokes equations described in Section (2.1). In the following the flag geometry approximation technique as described in Griebel et al. (1998) is reviewed. As an improved alternative the geometry approximation by a level set function is presented and compared to flag field approach. In both techniques a linear system results from the discretization of the Poisson problem. All considerations in this chapter are for the two dimensional case because the extension to the three dimensional case is straight forward.

Here, the Poisson equation with Neumann boundary conditions reads as

$$-\Delta p = f \qquad \text{on} \quad \Omega_f \tag{3.1}$$

$$\frac{\partial p}{\partial n} = 0 \qquad \text{on} \quad \Gamma_{\Omega_f}. \tag{3.2}$$

Usually the the Poisson equation is discretized on a regular grid with finite difference stencils for the first and second derivatives. Therefore, the discretization of the first part of equation (3.1) is given by

$$\Delta p = -\frac{p_{i+1,j}}{dx^2} + \frac{2p_{i,j}}{dx^2} - \frac{p_{i-1,j}}{dx^2} - \frac{p_{i,j+1}}{dy^2} + \frac{2p_{i,j}}{dy^2} - \frac{p_{i,j-1}}{dy^2}. \tag{3.3}$$

Using an equidistant grid ($dx = dy$) the system reduces to the classical five point stencil

for the interior points of the Laplacian

$$\begin{bmatrix} & -1 & \\ -1 & 4 & -1 \\ & -1 & \end{bmatrix}. \tag{3.4}$$

The incorporation and the discretization of the Neumann boundary condition discretized by finite differences is the major challenge in the treatment of complex obstacles and will be explained in the following section of this chapter.

3.1 Incorporating complex geometries

The solution of the Poisson problem

$$\Delta p(x) = f \qquad x \in \Omega \tag{3.5}$$

has been of constant research interest for the last century. For Dirichlet boundary conditions

$$p(x) = c(x) \qquad x \in \Gamma_\Omega, c \in \mathbb{C}^\infty \tag{3.6}$$

a second order approach was presented by Shortley & Weller (1938). This approach can adapt to irregular domains on a rectangular grid. Further investigations of this discretization for Dirichlet boundary conditions were conducted by many others, for example Batschelet (1952), Bramble & Hubbard (1965), Hackbusch (1992) or Matsunaga & Yamamoto (2000). Several contributions were made to estimate the error of the finite difference approximation of the Poisson problem (3.5) with other boundary conditions on rectangular and irregular shaped domains. For example, Batschelet (1952), Bramble & Hubbard (1965), Jomaa & Macaskill (2005), Bouchon & Peichl (2007), and Jomaa & Macaskill (2005) regarded the Neumann boundary conditions on rectangular domains and mixed boundary conditions on irregular shaped domains. Here, the mixed boundary conditions are a combination of Dirichlet and Neumann boundary conditions and read as

$$\beta \frac{\partial p(x)}{\partial n} + p(x) = c \qquad \beta \in \mathbb{R}, x \in \Gamma_\Omega, c \in \mathbb{C}^\infty. \tag{3.7}$$

The error estimates for the mixed boundary conditions presented in Jomaa & Macaskill (2010) depend on β and do not admit pure Neumann boundary conditions. Furthermore, a treatment of the pure Neumann boundary conditions was regarded by Bouchon & Peichl (2007) who used local transformations which transformed the boundary interpolation problem onto a subgrid. On this subgrid a small linear system has to be solved to calculate the boundary value. This approach needs further informations about the grid and requests additional geometrical properties of the grid cell and the intersecting boundary. In the following a grid aligned approximation of the boundary is described, the so-called flag field technique. Here, the boundary is approximated by a rectangular grid, whereas a cell can be geometry or fluid domain. On the one hand the advantage of this approach is that boundary conditions are imposed on the grid lines and no interpolation or averaging is needed. On the other hand the ability to resolve the geometry is limited. After that the variable approximation of the boundary by a level set (Sussman et al., 1994) is introduced which extends ideas for the interpolation from Batschelet (1952) to incorporate Neumann boundary conditions on arbitrary domains into the system matrix of the discretized operator.

3.1.1 Constant geometry approximation with the flag field technique

For the inner points of the example from Figure (3.1) the discretization of the Poisson problem with the stencil (3.4) leads to the inner rows of the matrix A in equation (3.9). Additionally, the discretization of the Neumann boundary condition

$$\frac{\partial p}{\partial n} = \frac{p_{out} - p_{in}}{dx} \tag{3.8}$$

for a rectangular grid aligned to the domain leads to the first and the last four rows of $A \in \mathbb{R}^{4+4\times 4+4}$ which results in a 12×12 linear system.

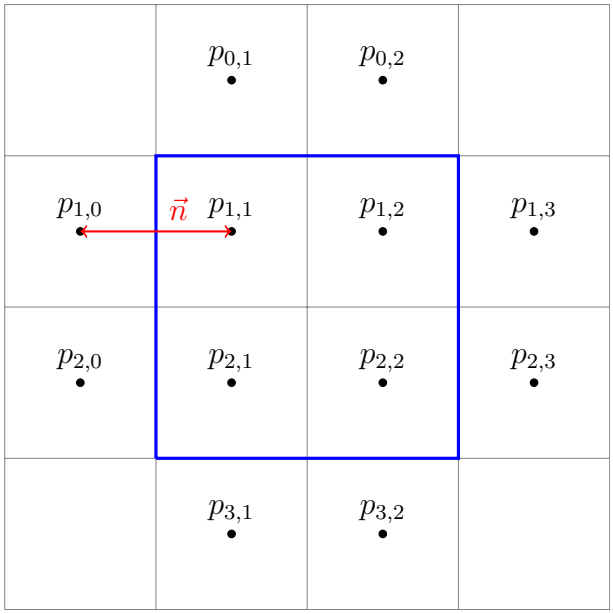

Fig. 3.1: Discretization of the Poisson problem with Neumann boundary conditions on a square domain. Here, the discretization with a 2×2 grid including all boundary ghostcells is demonstrated. The interpolation routine for the Neumann boundary condition reads $\frac{\partial p}{\partial n} = \frac{p_{1,1} - p_{1,0}}{dx} \stackrel{!}{=} 0$ and equation (3.9) presents the corresponding linear system.

$$A = \left(\begin{array}{cccc|cccc|cccc} -1 & 0 & 0 & 0 & 1 & 0 & 0 & 0 & 0 & 0 & 0 & 0 \\ 0 & -1 & 0 & 0 & 0 & 1 & 0 & 0 & 0 & 0 & 0 & 0 \\ 0 & 0 & -1 & 0 & 1 & 0 & 0 & 0 & 0 & 0 & 0 & 0 \\ 0 & 0 & 0 & -1 & 0 & 1 & 0 & 0 & 0 & 0 & 0 & 0 \\ \hline 1 & 0 & 1 & 0 & -4 & 1 & 1 & 0 & 0 & 0 & 0 & 0 \\ 0 & 1 & 0 & 1 & 1 & -4 & 0 & 1 & 0 & 0 & 0 & 0 \\ 0 & 0 & 0 & 0 & 1 & 0 & -4 & 1 & 1 & 0 & 1 & 0 \\ 0 & 0 & 0 & 0 & 0 & 1 & 1 & -4 & 0 & 1 & 0 & 1 \\ \hline 0 & 0 & 0 & 0 & 0 & 0 & 1 & 0 & -1 & 0 & 0 & 0 \\ 0 & 0 & 0 & 0 & 0 & 0 & 0 & 1 & 0 & -1 & 0 & 0 \\ 0 & 0 & 0 & 0 & 0 & 0 & 1 & 0 & 0 & 0 & -1 & 0 \\ 0 & 0 & 0 & 0 & 0 & 0 & 0 & 1 & 0 & 0 & 0 & -1 \end{array}\right) \cdot \left(\begin{array}{c} p_{0,1} \\ p_{0,2} \\ p_{1,0} \\ p_{1,3} \\ \hline p_{1,1} \\ p_{1,2} \\ p_{2,1} \\ p_{2,2} \\ \hline p_{2,0} \\ p_{2,3} \\ p_{3,1} \\ p_{3,2} \end{array}\right) = \left(\begin{array}{c} 0 \\ 0 \\ 0 \\ 0 \\ \hline f_{1,1} \\ f_{1,2} \\ f_{2,1} \\ f_{2,2} \\ \hline 0 \\ 0 \\ 0 \\ 0 \end{array}\right) \tag{3.9}$$

In the following the matrix A is used as the basic setting for the implementation of an irregular domain Ω_f. After some manipulation the stencils reduce to the following system

$$\left(\begin{array}{cccc|cccc|cccc}
-1 & 0 & 0 & 0 & 1 & 0 & 0 & 0 & 0 & 0 & 0 & 0 \\
0 & -1 & 0 & 0 & 0 & 1 & 0 & 0 & 0 & 0 & 0 & 0 \\
0 & 0 & -1 & 0 & 1 & 0 & 0 & 0 & 0 & 0 & 0 & 0 \\
0 & 0 & 0 & -1 & 0 & 1 & 0 & 0 & 0 & 0 & 0 & 0 \\
\hline
0 & 0 & 0 & 0 & -2 & 1 & 1 & 0 & 0 & 0 & 0 & 0 \\
0 & 0 & 0 & 0 & 1 & -2 & 0 & 1 & 0 & 0 & 0 & 0 \\
0 & 0 & 0 & 0 & 1 & 0 & -2 & 1 & 0 & 0 & 0 & 0 \\
0 & 0 & 0 & 0 & 0 & 1 & 1 & -2 & 0 & 0 & 0 & 0 \\
\hline
0 & 0 & 0 & 0 & 0 & 0 & 1 & 0 & -1 & 0 & 0 & 0 \\
0 & 0 & 0 & 0 & 0 & 0 & 0 & 1 & 0 & -1 & 0 & 0 \\
0 & 0 & 0 & 0 & 0 & 0 & 1 & 0 & 0 & 0 & -1 & 0 \\
0 & 0 & 0 & 0 & 0 & 0 & 0 & 1 & 0 & 0 & 0 & -1
\end{array}\right) \cdot \left(\begin{array}{c}
p_{0,1} \\ p_{0,2} \\ p_{1,0} \\ \underline{p_{1,3}} \\
p_{1,1} \\ p_{1,2} \\ p_{2,1} \\ \underline{p_{2,2}} \\
p_{2,0} \\ p_{2,3} \\ p_{3,1} \\ p_{3,2}
\end{array}\right) = \left(\begin{array}{c}
0 \\ 0 \\ 0 \\ 0 \\
f_{1,1} \\ f_{1,2} \\ f_{2,1} \\ f_{2,2} \\
0 \\ 0 \\ 0 \\ 0
\end{array}\right). \tag{3.10}$$

Here, $p = (p_{1,1}, \ldots, p_{n,n})$ is the solution of the linear system $A_{int}p = f$ consisting of the inner 4×4 matrix $A_{int} \in \mathbb{R}^{n \times n}$ and the corresponding right hand side $f = (f_{1,1}, \ldots, f_{n,n})$ which results from the discretized Poisson problem on the given domain. With this discretization the approximation of arbitrarily shaped domains leads to a matrix A_{int} which is symmetric positive semi definite. In detail, all but one of the Eigenvalues $\lambda_i \in \mathbb{R}$ are non zero. Therefore, the matrix has a one dimensional null space and the typical numerical solvers like CG methods run into problems. A theoretical fact states that if the null space does not contain the starting vector, the conjugate gradient method solves the system $Ap = f$ or at least minimizes $\|Ap - f\|_2$ (Kammerer & Nashed, 1972). But nevertheless, the numerical computation of an iterative solution can fail due to truncation and other numerical problems. To overcome this drawback and fix the null space an additional condition for the linear system is necessary. Here, the fixation of a single value or the condition

$$\int_{\Omega_f} p \, dx = 0 \tag{3.11}$$

are possible solutions. With this additional equation the linear system transforms into an over-determined $(n+1) \times n$ system and best approximation methods have to be applied.

3.1.2 Variable geometry approximation with a level set technique

To overcome the drawback of the limited geometry representation of the flag field technique, the geometry is represented by a level set function ϕ_g which is a signed distance function defined in equation (2.30). At this point the sign of ϕ_g determines wether a point is in the obstacle domain Ω_g or in the fluid domain Ω_f. Without loss of generality a positive level set value $\phi_g(x) > 0$ denotes the fluid domain, whereas a negative level set value $\phi_g(x) < 0$ denotes the geometry domain Ω_g. The boundary of the obstacle is described by the zero level set contour $X_g = \{x \in \Omega \,|\, \phi_g(x) = 0\}$. Because of the fact that

$$n(x) = \frac{\nabla \phi_g(x)}{\|\nabla \phi_g(x)\|_2} \quad x \in \Omega. \tag{3.12}$$

the computation of a normal is easy and an advantage of the level set formulation. Note that the normalisation with the euclidean norm of the gradient of the level set function is not necessary at this point due to the Eikonal equation $\|\nabla \phi_g(x)\|_2 = 1$. To avoid later problems during the discretization of the gradient and the resulting normal a renormalisation at this point is maintained. Furthermore, a second order central difference scheme is applied here to approximate the normals. A test of this approach on a spherical domain should be to calculate the error of the approximated normal from the level set function. Therefore, the error is calculated by

$$\varepsilon_n := \max_{x \in \Gamma_{\Omega_f}} \|n_h(x) - n(x)\|_2 \tag{3.13}$$

with

$$\Gamma_{\Omega_f} := \{x \in \Omega \,|\, \phi_g(x) = 0\} \tag{3.14}$$

where n_h denotes the approximated normal and n describes the analytical normal for an obstacle. Figure (3.3) demonstrates the errors for the approximation of the normal for the flag field and the level set method. Here, the approximation of the normals at an analytical given sphere is presented in Figure (3.2). Due to its design the flag field method with its grid aligned approximation of the geometry leads to normals which are exclusively vertical and horizontal. Thus, there is no convergence for the normals on a

sphere in the $\|\cdot\|_\infty$ norm. In contrast to the flag field method the level set approximation leads to a second order approximation of the normals. Both convergence results are presented in Figure (3.3). This effect can not be overcome by a rearrangement of the grid or a variation of the cells. Therefore, a convergence for the solution of the poisson problem with Neumann boundary conditions on a irregular shaped domain can not be expected for the flag field technique. Exceptions for certain geometries are possible. For example, the Poisson problem can be solved with full convergence on a domain which is composed of rectangular obstacles and therefore fully resolvable by the flag field technique. But in general, a discretization technique has to converge for the boundary normal vectors on every arbitrary domain. Otherwise it is not possible to get convergence for the Neumann boundary conditions in the Poisson problem.

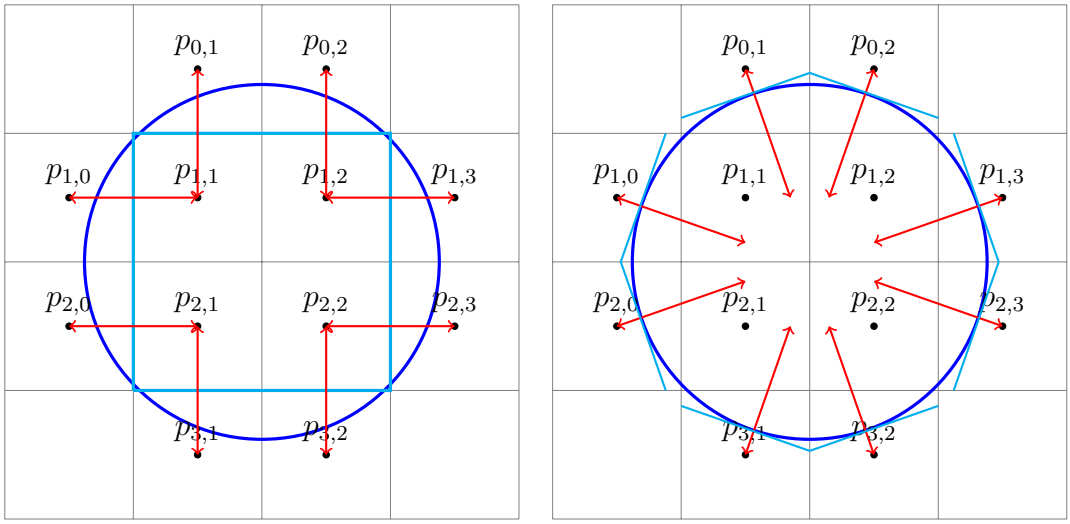

Fig. 3.2: Approximation of a circle and the boundary normals. Left: With a grid aligned approximation method there are only two possible normals, this results in no convergence for the geometry with Neumann boundary conditions. Right: The level set approach admits the approximation of arbitrary normals. In this setting the normals converge. See Figure (3.3).

After testing the approximation of the domain and analyzing in detail the boundary normals by the flag field method as well as by the new level set approach, the quality of the solution of the system (3.1) is regarded.

In the following the level set method is used to approximate the domain Ω_f and to modify the stencil (3.4) in the matrix A from (3.9) in accordance with the new geometry representation. Figure (3.4) presents a circular domain and the approximated normals

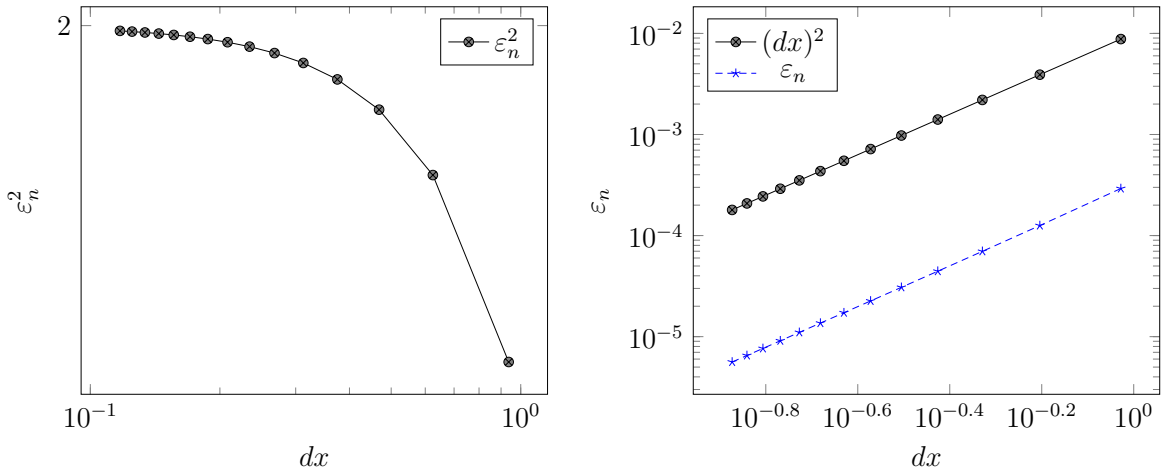

Fig. 3.3: Left: Approximation of the interface normal of a given spherical level set zero contour by the flag field method. This result shows no convergence for the normals. Note here, that the error is squared and therefore the maximum error in this two dimensional example is $\sqrt{2}$. Right: Approximation of the normals at a spherical zero level set contour X_g results in a second order approximation.

at the boundaries.

Let (i, j) be a fluid cell and without loss of generality $(i-1, j)$ denotes its neighbor out of the fluid domain. The first step is to calculate a proper normal vector at the boundary of the domain while the stencil of the fluid cell has to use the pressure value p_b at x_b in the boundary cell. Therefore, it is straight forward to approximate the intersection of the level set function on the grid line j and compute the point of intersection x_s by a linear interpolation, compare Figure (3.5). Then the normal at this position is approximated by the gradient of ϕ_g from the neighboring level set values. Given the point x_b and the normal at this position the straight line from x_b in direction of the normal intersects the x- or the y-grid lines. This point of intersection with the grid x_{int} is used to interpolate the pressure value p_{int} by linear interpolation from the neighboring pressure values. Thus, p_{int} is used to impose the Neumann condition

$$\frac{\partial p}{\partial n} = \frac{p_b - p_{int}}{x_b - x_{int}} \stackrel{!}{=} \tilde{g} \tag{3.15}$$

for the cell out of the domain. In detail, Figure (3.5) demonstrates the discretization and the interpolation of the Neumann boundary conditions at the zero level set contour.

In general, the algorithm is summarized as

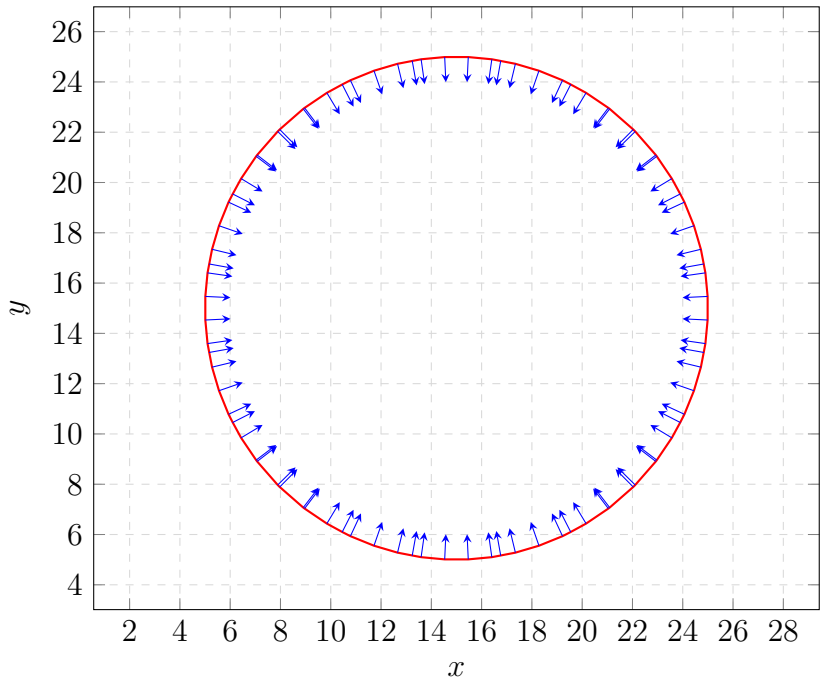

Fig. 3.4: Approximation of a circular domain by the level set method including boundary normals.

1. Approximate the intersection x_s
2. Approximate the normal $n(x_s) = \left(n_i, n_j, n_k \right)^T$
3. Scale $n(x_s)$ s.t $\tilde{n}(x_s) = c \cdot n(x_s)$ such that $\max\{\tilde{n}_i, \tilde{n}_j, \tilde{n}_k\} = dx$
4. Compute the interpolation position$x_{int} = x(p_b) + \tilde{n}(x_s)$
5. Interpolate $p(x_{int})$ from the neighboring fluid values.
6. $\frac{\partial p}{\partial n} = \frac{p_{int} - p_b}{\|\tilde{n}(x_s)\|_2} = \tilde{g}$

For example, the Neumann condition applied for p_{int} at x_{int} with a geometry neighbor $p_b = p_{i-1j}$ at $x_b = x_{i-1j}$ reads

$$\frac{\partial p}{\partial \tilde{n}} = \frac{p_{int} - p_{i-1j}}{x_{int} - x_{i-1j}} \stackrel{!}{=} \tilde{g}. \tag{3.16}$$

For homogeneous Neumann boundary conditions $\tilde{g} = 0$ is set. If x_{int} lies on the i grid

line between j and $j-1$, the interpolation for p_{int} reads

$$p_{int} = w_{ij}p_{ij} + w_{ij-1}p_{ij-1} \overset{(3.16)}{\Rightarrow} \tag{3.17}$$

$$0 = w_{ij}p_{ij} + w_{ij-1}p_{ij-1} - p_{i-1j} \tag{3.18}$$

As an implicit incorporation into the matrix A_{int} the coefficients from the linear lagrangian interpolation are added to the stencil from (3.4). In detail, the stencil and the entries for $p_{i,j}$ of the matrix reduce to

$$\begin{bmatrix} & 1 & \\ 0 & -4 + w_{ij} & 1 \\ & 1 + w_{ij-1} & \end{bmatrix} \tag{3.19}$$

Note here, if the normal in this case is parallel to the y line, i.e. $w_{ij} = 1$ and $w_{ij-1} = 0$, the standard five point stencil is recovered. The north, west, and east neighbors are modified in the same way. For the diagonal neighbors the situation changes. Here, additional entries in the stencil emerge leading to a flexible adjustment to the normal vectors. For example, if the normal vector from x_{i-1j} intersects the grid line x_i between y_j and y_{j-1} the weights of the interpolation ω_{ij} and ω_{ij-1} are added to the stencil weights -4 and 1 of the standard stencil, compare Figure (3.5). However, a normal vector at x_{i-1j} which intersects the grid line y_{j+1} between x_{i-1} and x_i results in an additional entry in the stencil at the diagonal position, see Figure (3.6), and the stencil reads as

$$\begin{bmatrix} w_{i-1j+1} & 1 + w_{ij+1} & \\ 0 & -4 & 1 \\ & 1 & \end{bmatrix}. \tag{3.20}$$

Incorporating the newly calculated stencil into the new system matrix $\tilde{A}_{int}$, the symmetry is destroyed. At least for the circular domain $\tilde{A}_{int}$ is centrosymmetric

$$a_{i,j} = a_{n-i+1,n-j+1} \qquad \forall i,j \leq n \qquad A = (a_{ij})_{1\leq i,j\leq n} \in \mathbb{R}^{n\times n} \tag{3.21}$$

and the Eigenvalues are complex.

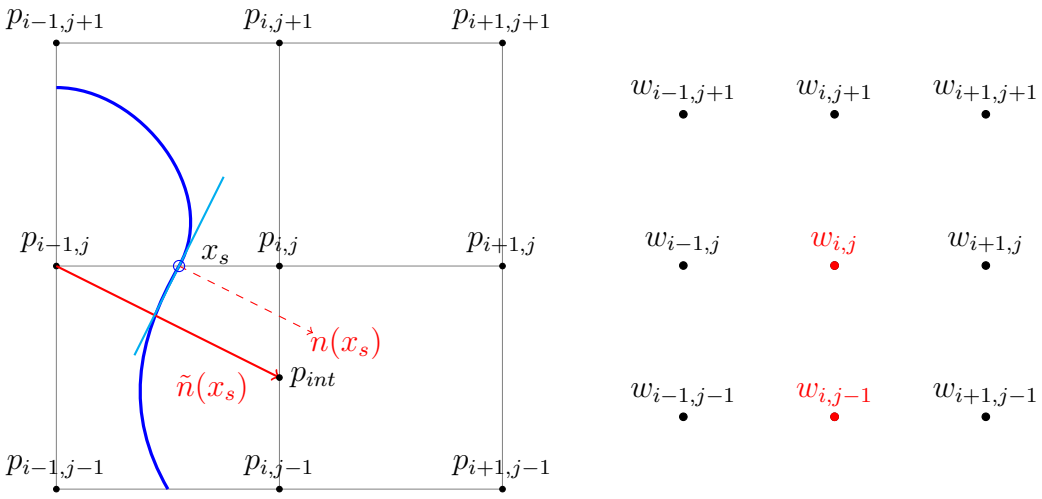

Fig. 3.5: Left: Grid points involved in the stencil, when imposing boundary conditions. Here, the south neighbor p_{ij-1} needs to be modified. The normal intersecting the grid line determines which coefficients of the neighbors have to be modified. Right: The main and south coefficient of the stencil are influenced by the boundary interpolation routine.

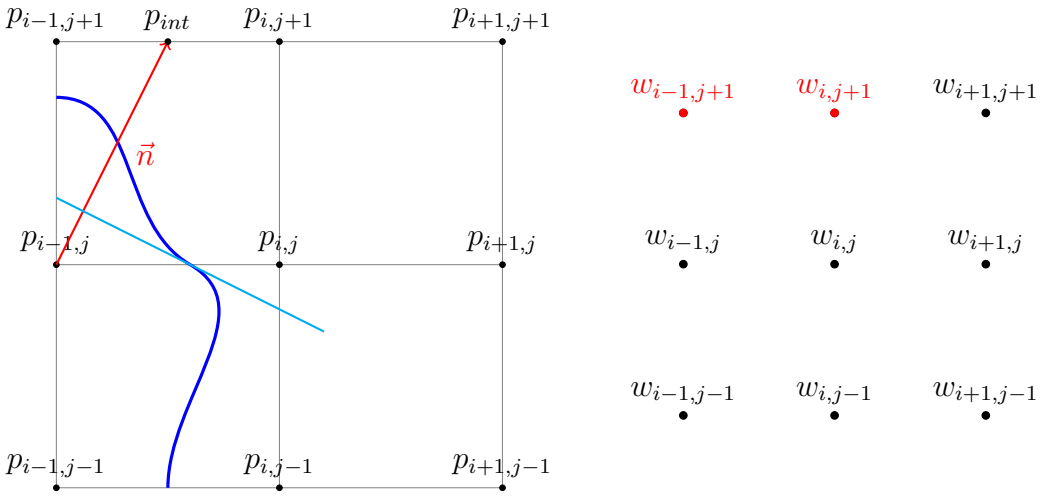

Fig. 3.6: Left: Grid points involved in the stencil, while imposing boundary conditions. Here, the north-west neighbor needs to be modified. In contrast to the previous setting from the grid aligned discretization in Figure(3.1) the normal intersects the grid between the north and the north west neighbor. In contrast to the case described in Figure (3.5), non zero coefficients are affected additionally. Right: The coefficients of the stencil influenced by the boundary interpolation routine. In addition to the classical 5 point stencil coefficients an extra coefficients is non zero.

Similarly to the matrix A_{int} originating from the flag field method, the new matrix $\tilde{A}_{int}$ contains a single null space. Regarding the example of the approximation of a circular domain the matrix resulting from the level set method reads as

$$\tilde{A}_{int} = \left(\begin{array}{cccc|cccccc|c}
-3.3276 & 1.3276 & 0 & 0 & 0.7082 & 1.2918 & 0 & 0 & 0 & 0 & \dots \\
1.0000 & -3.1086 & 1.1086 & 0 & 0 & 0 & 1.0000 & 0 & 0 & 0 & \dots \\
0 & 1.1086 & -3.1086 & 1.0000 & 0 & 0 & 0 & 1.0000 & 0 & 0 & \dots \\
0 & 0 & 1.3276 & -3.3276 & 0 & 0 & 0 & 0 & 1.7082 & 0.2918 & \dots \\
\hline
0 & 0 & 0 & 0 & -3.4165 & 1.7082 & 0 & 0 & 0 & 0 & \dots \\
1.0000 & 0 & 0 & 0 & 1.0000 & -4.0000 & 1.0000 & 0 & 0 & 0 & \dots \\
0 & 1.0000 & 0 & 0 & 0 & 1.0000 & -4.0000 & 1.0000 & 0 & 0 & \dots \\
0 & 0 & 1.0000 & 0 & 0 & 0 & 1.0000 & -4.0000 & 1.0000 & 0 & \dots \\
0 & 0 & 0 & 1.0000 & 0 & 0 & 0 & 1.0000 & -4.0000 & 1.0000 & \dots \\
0 & 0 & 0 & 0 & 0 & 0 & 0 & 0 & 1.7082 & -3.4165 & \dots \\
\hline
\vdots & \ddots & \ddots & \ddots & \ddots & \ddots & \ddots & \ddots & \ddots & \ddots & \ddots
\end{array}\right).$$

The spectrum of $\tilde{A}_{int}$ contains a single zero Eigenvalue $|\lambda_n| = 0$ and is illustrated in Figure (3.7).

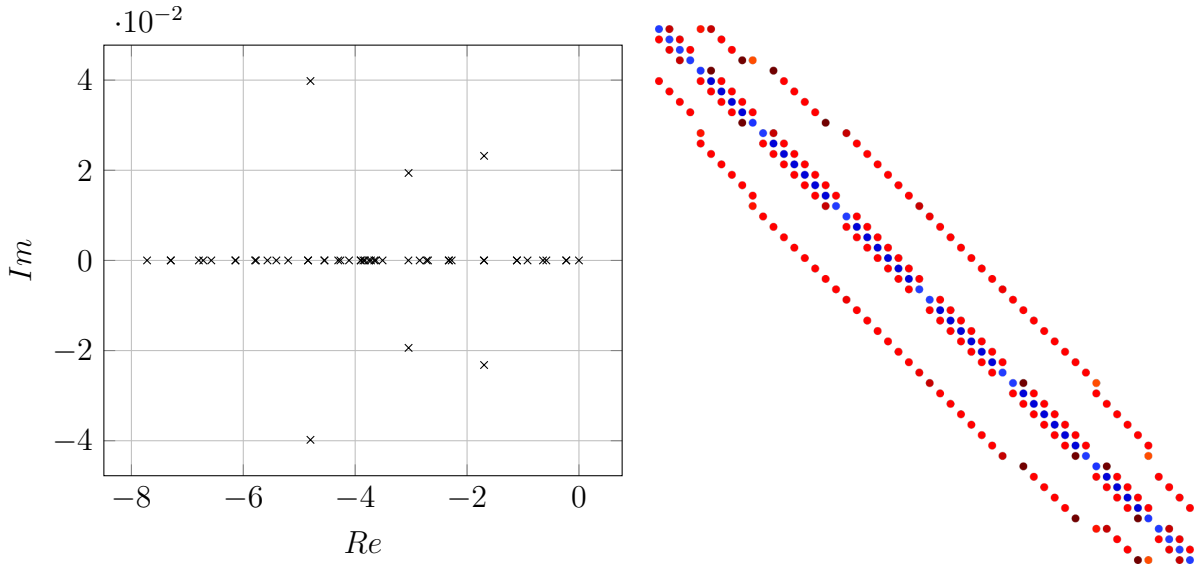

Fig. 3.7: Left: The spectrum of the modified matrix $\tilde{A}_{int}$ contains complex Eigenvalues and a single $|\lambda_n| = 0$. Right: Visualization of the matrix $\tilde{A}_{int}$ with Matlab's spy() function. The sparsity and the band structure of the matrix are obvious.

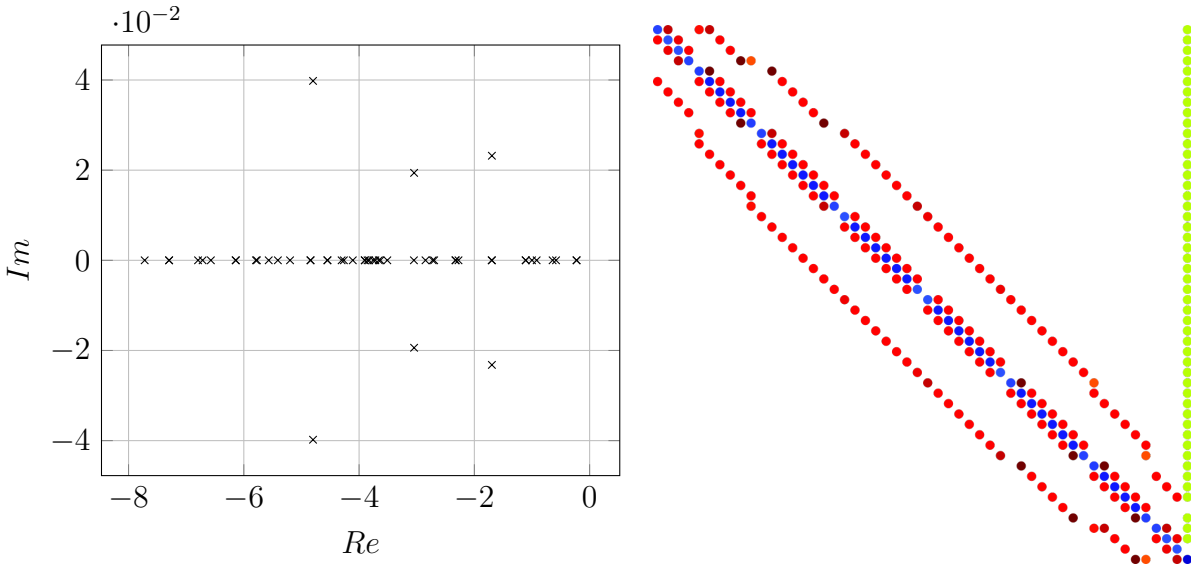

Fig. 3.8: Left: The stabilization leads to a non singular matrix with a spectrum which still has complex Eigenvalues. Right: Visualization of the stabilized matrix $\tilde{A}_s$ with Matlab's spy() function. Except the last column which is full, the sparsity and band structure are preserved. Obviously there is no symmetric structure left which leads to the use of the stabilized BiCG method.

Here, the typical techniques to eliminate this null space are applied. For examples, if one pressure value is fixed by imposing the following additional conditions

$$p_n = p_0, \tag{3.22}$$

and this condition is added to all rows in the linear system the matrix has full rank. Now, the full system reads

$$\left(\tilde{A}_{int} + (0 \dots 0|1)\right) p =: \tilde{A}_s p = \tilde{f} + p_0 \tag{3.23}$$

and without any loss of generality p_0 is chosen as $p_0 = 0$. Other choices are analogous and lead to additional terms on the right hand side $\tilde{f}$. This leads to the system $\tilde{A}_s p = \tilde{f}$. Applying this stabilization technique to the matrix the last column of the matrix is full and therefore the centrosymmetric property is also lost, see Figure (3.8). The solution of the resulting system $\tilde{A}_s p = \tilde{f}$ is computed by a stabilized BiCG method after Sleijpen & Fokkema (1993) which is a stabilized version of the previously presented BiCG method from van der Vorst (1992). Other methods for the solution of systems with non symmetric

matrices with complex Eigenvalues and other modifications of the BiCG method were presented in Sleijpen et al. (1994).

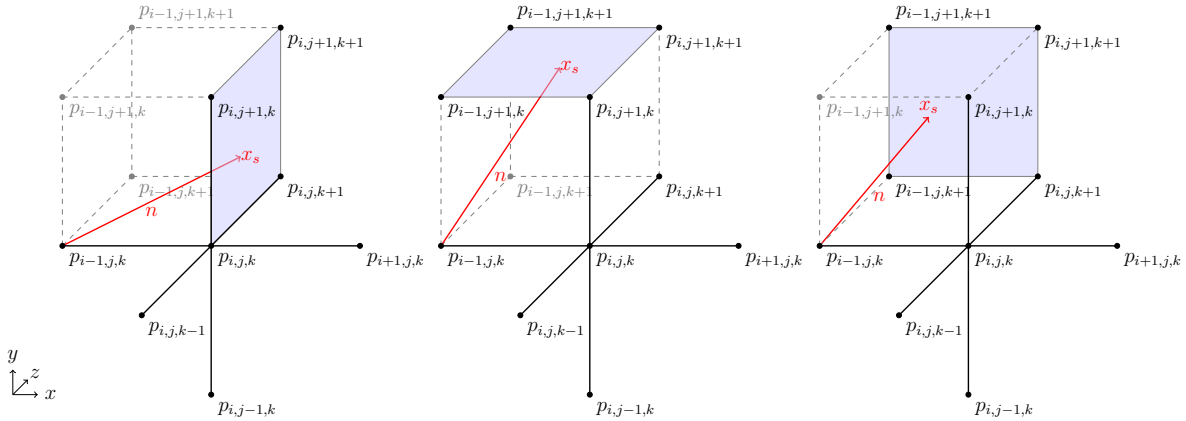

Fig. 3.9: Extension of the interpolation schemes to the three dimensional case. Three different scenarios are possible where the normal intersects different faces of the cell. In the first case only $p_{i,j+1,k+1}$ as an additional entry is used in the interpolation of the value $p_{i-1,j,k}$ and is added to the matrix. For the second and third case three additional values enter the interpolation scheme and therefore the matrix.

This stabilization of the original matrix leads to an additional overhead during the computation of a solution $\tilde{A}_s p = \tilde{f}$ on a parallel cluster grid. Applying a parallel BiCG method requires a full communication of p_n to all other processes in each matrix vector product from the process which iterates over the n-th column in the matrix. Moreover, this communication over all processes in the cluster grid slows down processes were the matrix vector product is already computed. Here, other processes have to wait for the completion of the matrix vector product on the process containing p_n. The general algorithm from van der Vorst (1992) as implemented in NaSt3D is extended by an additional global communication that is necessary before every matrix vector product. Thus, four global communication routines are added in each iteration step, which affect the performance negatively.

But the full influence of this communication routine on the full Poisson solver can not be divided from two facts. The arbitrary structure of the matrix $\tilde{A}_s$ and the modifications due to the new obstacle approximation create complex Eigenvalues and a large condition number which result in additional numerical costs.

The extension of the presented interpolation scheme and the incorporation to a three

dimensional case is illustrated in Figure (3.9). With this sketch for $p_{i-1,j,k}$ all other cases for the interpolation of a proper value along the normal n are straight forward and will not be discussed further.

3.2 Numerical convergence test

In the following, the new approach is tested numerically at a modified two dimensional Poisson problem $\tilde{A}_s p = \tilde{f}$ on level set domains equipped with Neumann boundary conditions

$$-\Delta p = f \qquad \text{on} \quad \Omega_f \subset \mathbb{R}^2 \tag{3.24}$$

$$\frac{\partial p}{\partial n} = 0 \qquad \text{on} \quad \Gamma_f. \tag{3.25}$$

A stabilized BiCG method is used to solve the Poisson equation on a irregular shaped domain given by a zero level set contour Γ_f. For the evaluation of the new boundary discretization approach described above, the corresponding analytical function for p is chosen as

$$p = -\cos\left(\frac{\pi}{50}\left((x-15)^2 + (y-15)^2\right)\right) \quad (x,y) \subset \Omega_f. \tag{3.26}$$

With this choice the function p has its center in $c = (15, 15)$ with $\frac{\partial p}{\partial n} = 0$ at the circle around c with radius $r = 10$. Figure (3.10) illustrates the analytical solution p for the Poisson problem from equation (3.24). Equation (3.26) is constructed such that it fulfills the requested Neumann boundary conditions from equation (3.25). Given the analytical p, the right hand side f can be calculated as follows

$$\begin{aligned} f = -\frac{4\pi}{100}\Bigg(&2\sin\left(\frac{\pi}{50}\left((x-15)^2 + (y-15)^2\right)\right) \\ &+ 4\cdot\left((x-15)^2 + (y-15)^2\right)\cdot\cos\left(\frac{\pi}{50}\left((x-15)^2 + (y-15)^2\right)\right)\Bigg). \end{aligned} \tag{3.27}$$

To calculate the approximation error and to derive a convergence rate the analytical solution p is evaluated at the grid points x_{ij} of each simulated solution p_{ij}. In summary, there are three errors calculated from the simulations, where the errors between the

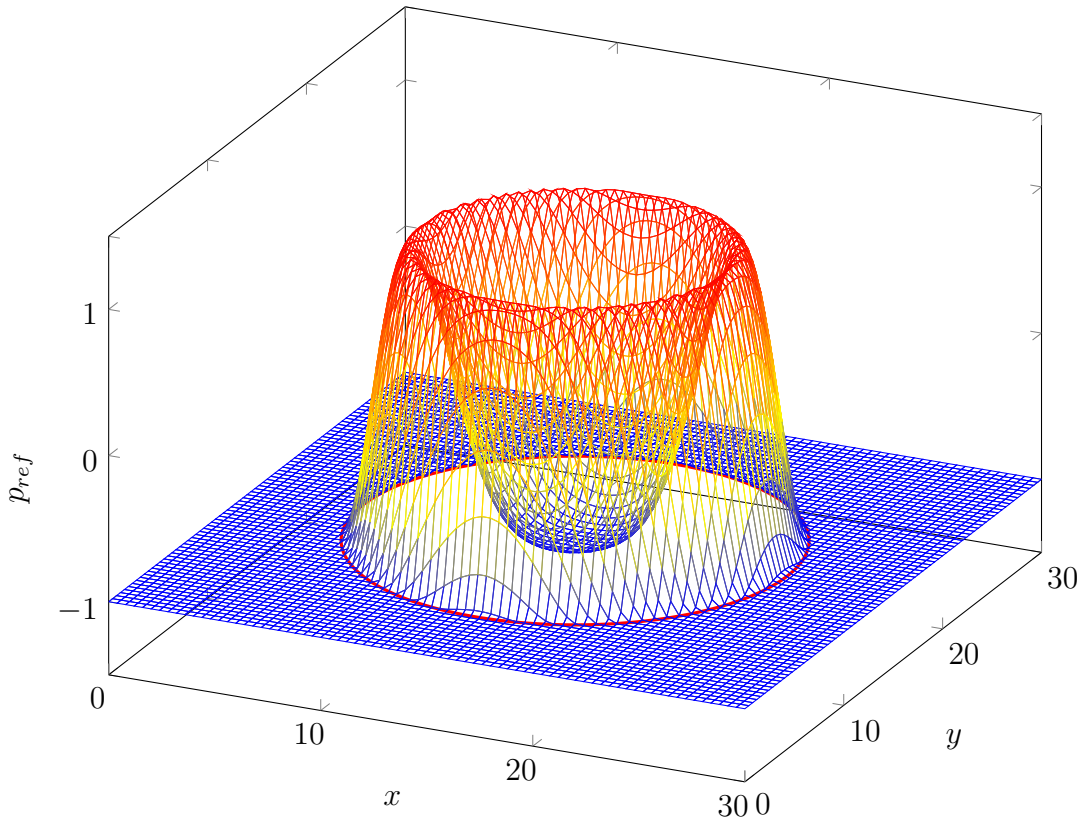

Fig. 3.10: The constructed analytical solution p from (3.26) of the Poisson problem with Neumann boundary conditions using f from (3.27) as right hand side on a circular domain (red).

simulated solution p_{ij} and the sampled solution $p_{ref_{ij}} = p(x_{ij})$ are calculated as follows

$$\|\cdot\|_\infty := \max_{i,j} |p_{ij} - p_{ref_{ij}}|, \tag{3.28}$$

$$\|\cdot\|_1 := \frac{1}{mn} \sum_{i,j}^{m,n} |p_{ij} - p_{ref_{ij}}| \tag{3.29}$$

and

$$\|\cdot\|_2 := \sqrt{\frac{1}{mn} \sum_{i,j}^{m,n} \left(p_{ij} - p_{ref_{ij}}\right)^2}. \tag{3.30}$$

Figure (3.11) shows the errors computed on $\Omega_{in} = \{x \in \Omega_f \,|\, dx \leq \phi(x_{ij})\}$ which represents the interior points with no neighbors outside of the domain Ω_f. Furthermore, Figure (3.11) illustrates the errors of the solution of the system (3.24) and (3.25) near the boun-

dary with the domain discretized on the one hand by the original flag field approach and on the other hand by the new level set approach. In detail, in the third and the fourth error plot of Figure (3.11) the errors (3.28), (3.29), and (3.30) are only computed on points x_{ij} where $0 \leq \phi(x_{ij}) \leq dx$. In the first two error plots of Figure (3.11) a second order convergence is obvious in all three error norms for both approximation techniques on the interior points. This analogous behaviour for both approaches matches the setting of a second order approximation of the Laplacian at the interior points with the standard five point finite difference stencil (3.4). Compared with the convergence on the interior points, the convergence on points near the boundary for the flag field technique is destroyed completely, compare Figure (3.11). But the new level set approach gives a first order convergence rate. This boundary approximation in the level set approach is realized with a linear interpolation scheme as described in equation (3.15). Therefore, the first order convergence near the boundary is plausible and improves the old method for arbitrarily shaped obstacles. Further interpolation schemes are not tested here. Higher polynomial interpolation schemes would require more points inside the domain, which would lead to an even more dense structure of the matrix. Other interpolation methods would need additional assumptions on the solution like smoothness or derivatives which are not at hand or have to be approximated by other points in the domain.

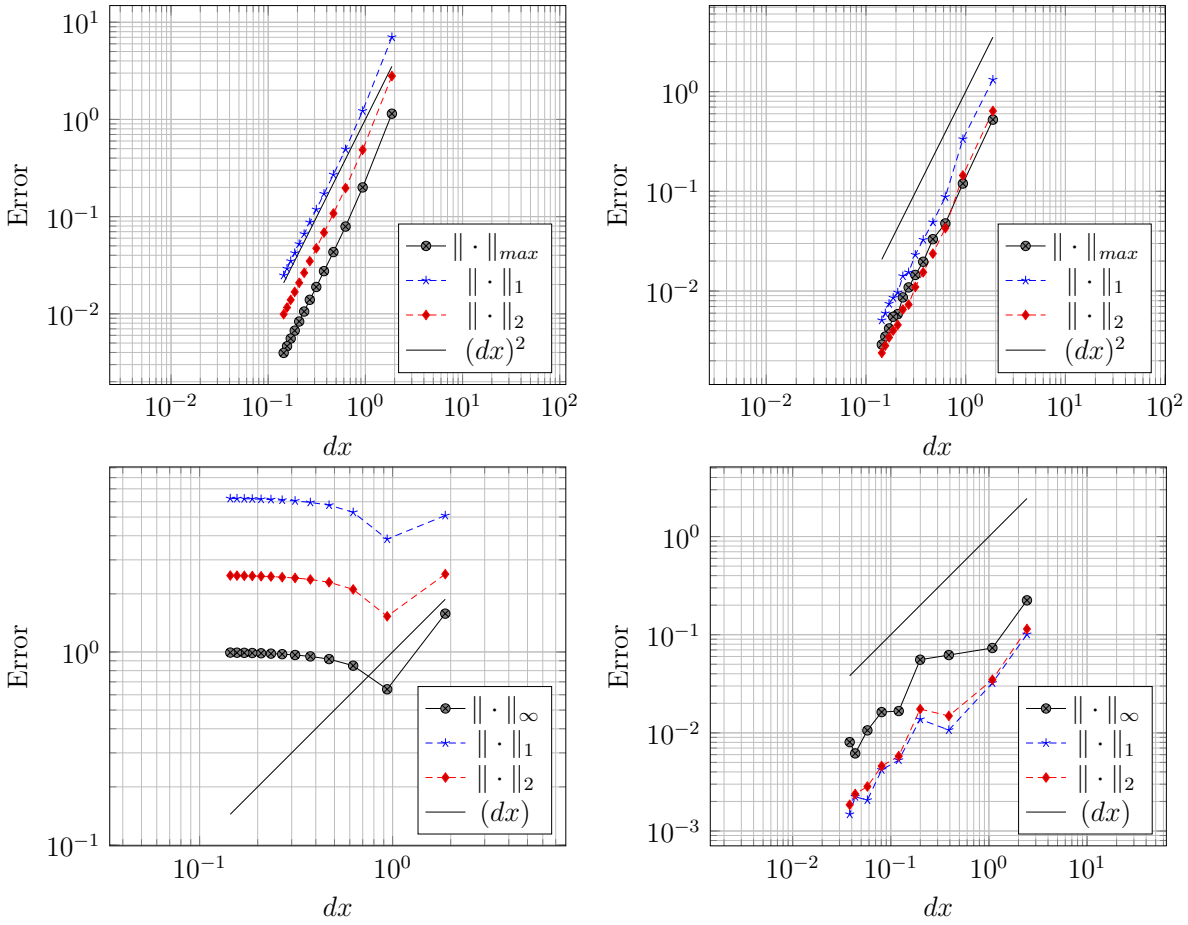

Fig. 3.11: Error convergence of the Poisson problem discretized by the flag field (left) and the level set (right) technique. All three errors show a second order error convergence for the interior points (top). In contrast to the interior points there is no convergence at all for the flag field technique (bottom left). But the level set approach on the points near the boundary yields first order convergence rates for all errors (bottom right).

4 Modified correction projection method to solve the Navier Stokes equations

In the following chapter the algorithm to solve the Navier Stokes equations on level set domains is described. As a short reminder, the transient incompressible dimensionless Navier Stokes equations for a single phase in three dimensions read as follows

$$\frac{\partial u}{\partial t} + (u \cdot \nabla)u = \frac{1}{Fr}g - \nabla p + \frac{1}{Re}\Delta u \qquad in \quad \Omega_f \in \mathbb{R}^3, \tag{4.1}$$

$$\nabla \cdot u = 0 \qquad in \quad \Omega_f \in \mathbb{R}^3. \tag{4.2}$$

where $x \in \Omega_f \subset \mathbb{R}^3$ describes the position, $u(x,t) = (u_i(x,t))_{1 \leq i \leq 3} \in \mathbb{R}^3$ denotes the velocities, $p(x,t) \in \mathbb{R}$ describes the pressure, and the time is denoted by $t \geq 0$. The parameter Re denotes the Reynold's number and Fr the Froude's number. For simplicity, all additional forces are dropped $f_i = 0$ in (2.3) and (2.4). In a next step, the modifications in Chorin's pressure projection are explained and discussed. In general, the correction projection method after Chorin (1968) is well known in the literature and was investigated and applied in numerous numerical studies, compare Temam (1968), Temam (1977), Jamet et al. (1970), Guermond (1994), Guermond & Quartapelle (1998), Temam (2001), and Guermond et al. (2006).
Given a divergence free velocity field u^n, the modified splitting scheme is sketched like the following

1. Compute u^* on $\Omega_{in} = \Omega_f \setminus \Omega_\varepsilon$ with $\Omega_\varepsilon := \{x \in \Omega_f \mid 0 \leq \phi(x) \leq \varepsilon\}$

$$u^* = u^n + dt\left((u^n \cdot \nabla)\, u^n + \frac{1}{Re}\Delta u^n\right) \tag{4.3}$$

Note here, that the pressure p is omitted and $\varepsilon = \sqrt{dx^2 + dy^2 + dz^2}$.

2. Interpolate u^* on $x \in \Omega_\varepsilon$ such that the boundary conditions are fulfilled

$$u^* \,|_\Gamma = 0 \tag{4.4}$$

on the boundary $\Gamma := \Gamma_{\Omega_f}$.

3. Calculate the right hand side for the Poisson problem $f_p = \nabla \cdot u^*$ on Ω_{in}.

4. Interpolate f_p on $x \in \Omega_\varepsilon$ such that the divergence free condition

$$\nabla \cdot u^* = f_p \,|_\Gamma = 0 \tag{4.5}$$

for u^* is prescribed at the boundary Γ.

5. Solve the Poisson problem $\Delta p^{n+1} = f_p$ on Ω_f with $\partial p / \partial n = 0$ on Γ.

6. Correct u^* to achieve a divergence free velocity field u^{n+1} on Ω_{in}.

$$u^{n+1} = u^* - dt \nabla p^{n+1} \tag{4.6}$$

7. Interpolate u^{n+1} on $x \in \Omega_\varepsilon$ such that the boundary condition

$$u^{n+1} \,|_\Gamma = 0 \tag{4.7}$$

is prescribed in close proximity to the boundary.

In the following, the details of every step in this algorithm will be explained. The modifications in this approach compared to the originally proposed scheme are necessary to handle the boundary conditions at the level set domain boundaries Γ. By calculating u^* in Step 1 only on the interior points Ω_{in} the preliminary velocities u^* are available at the interior points to impose the desired boundary conditions near Γ. Dirichlet conditions $u^*|_{\Omega_\varepsilon} = 0$ are imposed by an appropriate interpolation scheme. In general, Neumann boundary conditions for the velocities are not viable for this approach. Here, the staggered grid discretization for the velocity components $u = (u, v, w)$ and the Neumann condition $\nabla u \cdot n = 0$ lead to additional unknowns and to an under-determined linear system for the interpolation. In the third and fourth step analogous ideas are pursued. In

particular in Step 3 the right hand side $f_p = \nabla \cdot u^*$ for the Poisson problem is computed only on the inner domain Ω_{in}. The boundary condition for f_p on Ω_ε is imposed by an interpolation scheme in Step 4, which uses the available values from the inner domain. In the end, the new velocity field u^{n+1} has to fulfill the divergence free condition (2.19). Thus, a Dirichlet boundary condition $f_p|_\Gamma = 0$ for f_p is imposed on $x \in \Omega_\varepsilon$ which constitutes a divergence free field u^* on Γ. In the fifth step the aforementioned solver for the Poisson problem on an arbitrarily shaped level set domain is applied. Step 6 and the seventh step are necessary to guarantee a velocity field u^{n+1} on Ω_f with the proposed boundary conditions.

In summary, this scheme is an adapted version of the Chorin (1968) scheme, where differences were made to impose the boundary conditions. By forcing the boundary conditions by interpolation, it is assured that the velocity fields u^* and u^{n+1} as well as the right hand side of the Poisson problem f_p fulfill all boundary conditions required in each step.

4.1 Boundary conditions for the velocities

In detail, the Dirichlet boundary reads

$$u^*(x_\Gamma) = g \qquad x_\Gamma \in \Gamma_{\Omega_f}. \tag{4.8}$$

Again a two dimensional example is chosen to demonstrate the algorithm. As already mentioned in the Poisson solver the extension to a three dimensional treatment is straight forward and all schemes apply accordingly. The boundary is represented by the zero contour of the signed level set function $\phi_g(x)$ as before. Thus, the fluid domain can be distinguished by the sign of ϕ_g. Without loss of generality the fluid domain is represented by $\Omega_f = \{x \in \mathbb{R}^3 \,|\, \phi_g(x) \geq 0\}$. Following this notation, the boundary of the fluid is defined as $\Gamma_{\Omega_f} = \{x \in \Omega_f \,|\, \phi_g(x) = 0\}$. To reconstruct the zero contour and its position x_Γ it is essential to use an appropriate interpolation function f_{int}. Thus, the boundary domain Γ_{Ω_f} is calculated by an iterative second order Newton method

$$x_{n+1} = x_n - \frac{f_{int}(x_n)}{f'_{int}(x_n)} \tag{4.9}$$

which utilises a third order polynomial interpolation to calculate $f_{int}(x_n)$. In this setting the interpolating polynomial $f_{int}(x)$ is given in its Lagrange basis formulation

$$f_{int}(x) = \sum_{i=0}^{3} f_i a_i(x) \tag{4.10}$$

with

$$a_i(x) = \prod_{\substack{0 \leq m \leq 3 \\ m \neq i}} \frac{x - x_m}{x_i - x_m}. \tag{4.11}$$

Therefore, it is obvious to derive all factors for the derivative of the polynomial $f'_{int}(x)$ in advance to reduce the computational costs. With a reconstructed x_Γ on the interface the boundary conditions can be imposed at the interface for the intermediate velocities u^* as follows.

Here, the idea is to calculate u^* on the interior points

$$\Omega_{in} = \left\{ x \in \Omega_f \,|\, \phi_g(x) > \sqrt{dx^2 + dy^2 + dz^2} \right\} \tag{4.12}$$

as given in (4.4). Therefore, the calculation only considers points which are in the fluid domain and is represented in Figure (4.1). With the calculated values for u at this interior points the values $u(x_\varepsilon)$ at the almost interior point are determined such that the boundary conditions are fulfilled at Γ. The velocities for the values at $\tilde{x} \in \Omega_\varepsilon$ are interpolated along the boundary normal. In detail, the line from x_Γ along the scaled normal $\tilde{n}$ is used to calculate the intersection x_s with the adjacent faces generated by the interior points. With a calculated x_s the linear interpolation scheme along the surface normal for the Dirichlet boundary condition from the interior points reads as follows

$$u(t) = \frac{u(x_s) - g}{\|x_s - x_\Gamma\|_2} t + g \qquad t \in [0, \|x_s - x_\Gamma\|_2]. \tag{4.13}$$

The desired value for u_{ij} is set for $t = (\phi_g)_{ij}$ which denotes the level set value $\tilde{x}_{ij}$ and represents the distance to the zero contour ϕ_g. With the fact that $\|x_s - x_\Gamma\|_2 = \|x_s - \tilde{x}_{ij}\|_2 + (\phi_g)_{ij}$ and $t = (\phi_g)_{ij}$ the interpolation (4.13) reduces to

$$u_{ij} = \frac{u(x_s)(\phi_g)_{ij} + g\|x_s - \tilde{x}_{ij}\|_2}{\|x_s - \tilde{x}_{ij}\|_2 + (\phi_g)_{ij}}. \tag{4.14}$$

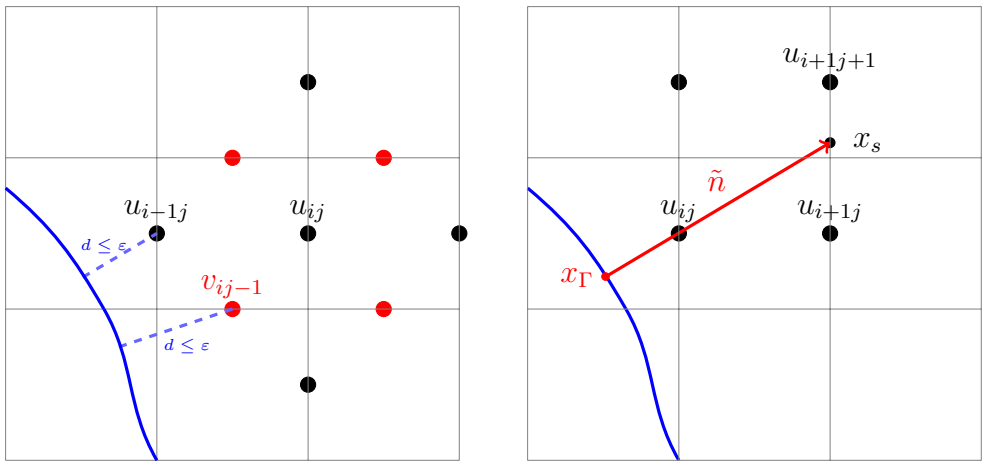

Fig. 4.1: Left: All points involved in the calculation u^* for u_{ij} for the interior point $x_{i,j} \in \Omega_{in}$. The example demonstrates the calculation for the u component in two dimensions. Adjacent values of the v component are marked in red, whereas the involved values of the u component are black. Here, u_{i-1j} and v_{ij-1} are near boundary points. Right: The boundary condition are imposed by interpolating the near boundary values $\tilde{u}(\tilde{x}_{i-1j}) = u_{i-1j}$ along the normal from the interior points u_{ij+1} and u_{ij}. Note here, that these interpolation routines are applicable for all velocity components separately.

For the calculation of $u(x_s)$ this approach applies a linear interpolation, which uses the velocity values on the grid line. In summary, all velocities at the interior points Ω_{in} are calculated from known values at inner points. All other fluid points Ω_ε which are near the boundary are interpolated in normal direction, such that the Dirichlet conditions are fulfilled in every point. This method is used to impose the correct boundary conditions on $x \in \Omega_\varepsilon$ in the prediction step u^* (4.4) for the right hand side f_p of the Poisson equation (4.5) as well as in the correction step for the new timestep u^{n+1} (4.7). Note here, that the condition for the right hand side f_p of the Poisson equation is given by

$$f_p := \nabla \cdot u^*(x) = 0 \qquad x \in \Omega_\varepsilon. \tag{4.15}$$

Therefore, imposing Dirichlet boundary condition for $f_p = 0$ is reasonable. With this choice the approximation of f_p and therefore u^* already fulfills the requested divergence free condition from the Navier Stokes equations at the boundary.

Furthermore, the implementation of a wall boundary law for a turbulence model after Van Driest (1956) is not discussed at this point. Due to the large variety of different tur-

bulence modeling approaches, the choice of the turbulence model and the wall law depend on the intended purpose. Therefore, the choice, the discussion and the implementation of a turbulence model are omitted in this thesis and the focus is on the handling of the complex geometries and a robust numerical implementation of the boundary conditions.

4.2 Numerical results for the Navier Stokes solver on level set geometries

To test the new algorithm, the example in Figure (4.3) is calculated for eleven different resolutions. Due to the absence of an analytical solution for the Navier Stokes equations a reference solution $u_{ref} = (u, v, w)$ is computed on a $500 \times 100 \times 100$ grid which results in a spatial grid size $dx = 0.005$. Three error norms L_∞,L_1 and L_2 are calculated and approximated, here for the u-component of u_{ref}, by

$$\|\cdot\|_\infty := \max_{i,j,k} |u_{ijk} - u_{ref_{ijk}}|, \tag{4.16}$$

$$\|\cdot\|_1 := \frac{1}{i_m j_m k_m} \sum_{i,j,k}^{i_m j_m k_m} |u_{ijk} - u_{ref_{ijk}}|, \tag{4.17}$$

and

$$\|\cdot\|_2 := \sqrt{\frac{1}{i_m j_m k_m} \sum_{i,j,k}^{i_m j_m k_m} \Big(u_{ijk} - u_{ref_{ijk}})\Big)^2} \tag{4.18}$$

where u_{ijk} denotes the computed solution on the coarser grid which was interpolated to the fine grid of u_{ref} by the Matlab function interp3(). Therefore, the indices of the finest grid are $(i_m, j_m, k_m) = (500, 100, 100)$. In general, the relative error

$$\varepsilon_{\infty,1,2} := \frac{\|u - u_{ref}\|_{\infty,1,2}}{\|u_{ref}\|_{\infty,1,2}}. \tag{4.19}$$

is considered. The general setting and the parameters for this example are summarized in Table (4.1), where the computational domain is set to $(2.5\,m \times 0.4\,m \times 0.4\,m)$ with a Reynold's number $Re = 500$. The physical end time is set as $t_{fin} = 2.0\,s$. For the temporal and spatial discretization a second order Adams Bashforth and a second order SMART scheme are used with a time step $dt = 0.25\,s/m^2 \cdot dx^2$. Therefore, an overall

Table 4.1: Computational parameters and setting for the benchmark problem presented in Figure (4.3).

Dimensions	Tfin	Re	Temporal	ConvectiveTerms	PoissonSolver	it_{max}	ε
$2.5 \times 0.4 \times 0.4$	2.0	500	AdamsBash2nd	SMART	BiCGStab	5000	10^{-12}

Table 4.2: Error norms for the benchmark of the Navier Stokes solver on level set geometries.

	u-Component			v-Component			w-Component		
dx	$\max\lvert\cdot\rvert$	$\lVert\cdot\rVert_1$	$\lVert\cdot\rVert_2$	$\max\lvert\cdot\rvert$	$\lVert\cdot\rVert_1$	$\lVert\cdot\rVert_2$	$\max\lvert\cdot\rvert$	$\lVert\cdot\rVert_1$	$\lVert\cdot\rVert_2$
0.016667	0.26847	0.068787	0.095689	1.5289	0.91615	1.0221	2.2	1.1654	1.2396
0.014286	0.23289	0.055208	0.076946	1.6157	0.73242	0.8331	2.4113	1.0397	1.1492
0.0125	0.1613	0.037338	0.051084	0.94615	0.47955	0.52207	1.4542	0.63621	0.6929
0.011111	0.13913	0.030406	0.042654	0.78024	0.39815	0.42444	1.2713	0.53618	0.5804
0.01	0.12708	0.026795	0.038289	0.77655	0.30659	0.3519	1.0827	0.49807	0.54409
0.0090909	0.065995	0.016603	0.021669	0.2915	0.16396	0.16387	0.44613	0.28129	0.267
0.0083333	0.098131	0.019346	0.027838	0.52981	0.22236	0.24848	0.8771	0.36938	0.40171
0.0076923	0.067768	0.014785	0.020187	0.36025	0.15416	0.1561	0.57066	0.28869	0.29439
0.0071429	0.05934	0.011907	0.015347	0.29615	0.13024	0.12263	0.40696	0.19897	0.18562
0.0066667	0.058899	0.012838	0.017178	0.33847	0.13894	0.13194	0.55506	0.26562	0.27941
0.00625	0.06232	0.014256	0.019086	0.17059	0.13411	0.12676	0.40697	0.22097	0.21996
Rate	**1.6806**	**1.8263**	**1.8776**	**2.1312**	**2.1548**	**2.345**	**1.902**	**1.8069**	**1.9103**

second order scheme is expected. As described before, a stabilized BiCG method for level set geometries is applied with a residual error criterium of $\varepsilon = 10^{-12}$. An analytical level set function for a sphere is chosen as an obstacle and a double parabolic profile is applied to the left inflow boundary. At the opposite face a Neumann boundary condition acts as an inout boundary condition. Regarding the sphere as an obstacle, all directions of the interpolation and discretization routines can be tested. Thus, the full performance of the algorithm is examined and all three errors are presented in Table (4.2) and in Figure (4.2). All data plots approximately show a second order convergence rate for the algorithm. After two seconds the vortex system around the sphere has fully developed and is visualized with streamlines and contour plots in Figure (4.3). Additionally, a detailled zoomed view of the vortex system and the pressure situation is presented in Figure (4.4).

In summary, this new approach presented a technique to impose Dirichlet boundary conditions for the Navier Stokes equations which is able to resolve the geometry given by

a zero level set. With this approach a second order discretization of the fluid velocities was described and investigated. The interpolation schemes are easy to implement and to extend to higher order schemes or other interpolation techniques.

4.3 Extension to two phase flows

The extension of the presented approximation for imposing Dirichlet boundary conditions on level set obstacles to a two phase flow is straight forward. Here, the interpolation of the continuous velocities follows the same schemes as for the single phase situation.
In the two phase flow solver the fluid level set function $\phi : \mathbb{R}^3 \to \mathbb{R}$ is used to track the free surface of the two fluid phases, gas and liquid. Therefore, the level set function is transported by the fluid velocities u in each time step by the transport equation

$$\frac{\partial \phi}{\partial t} + u \cdot \nabla \phi = 0. \tag{4.20}$$

For further details on the transport of the level set function compare Croce et al. (2004), Croce et al. (2009) and Croce (2010). Additionally, the fluid level set function has to be reinitialized after the transportation, such that the signed distance property is reconstructed by solving the Hamilton Jacobi equation (2.31). In both methods homogeneous Neumann boundary conditions

$$\frac{\partial \phi}{\partial n} = 0 \tag{4.21}$$

for a scalar ϕ has to be imposed at the obstacles. For such scalar values Neumann boundary conditions are imposed similarly as in the Poisson solver. The interpolation routine (3.18) is used to calculate the values for ϕ at the boundary such that the homogeneous Neumann boundary conditions are fulfilled. In contrast to the implicit incorporation into the local finite differences stencil, as described in the Poisson solver, the interpolated values are set for the grid values in the interior of the obstacle. This procedure can be extended to the transport of any scalar value. Temperature and concentration transport are only a few examples for typical scalar transport problems in the field of fluid dynamics. Likewise, the adaption of this approach to Dirichlet boundary conditions is easy at hand and follows the ideas already presented for the velocity components in equation (4.14).

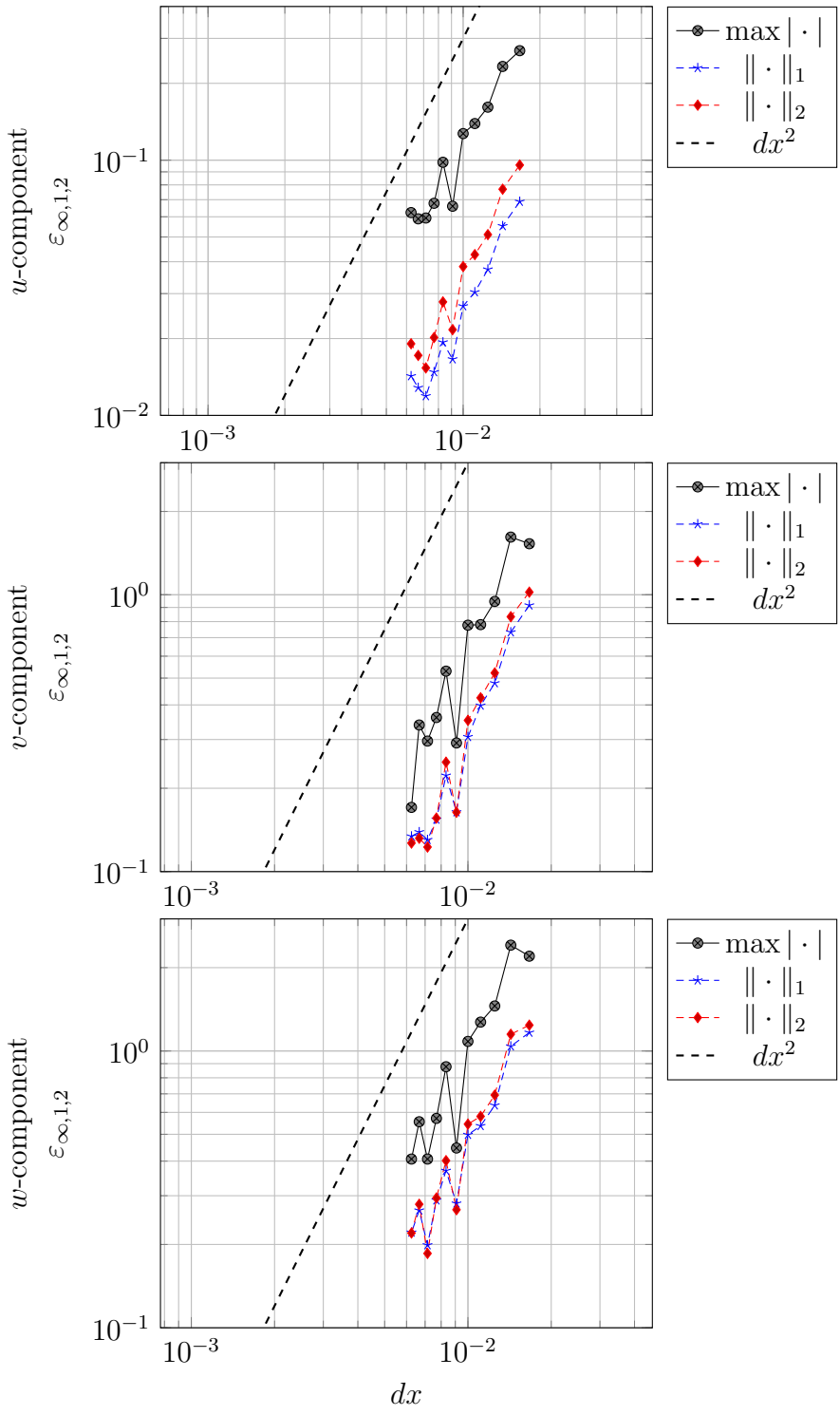

Fig. 4.2: The error norms for the velocity components in the benchmark problem. In each velocity component a second order convergence is observed, which is confirmed by the exact results for the errors presented in Table (4.2).

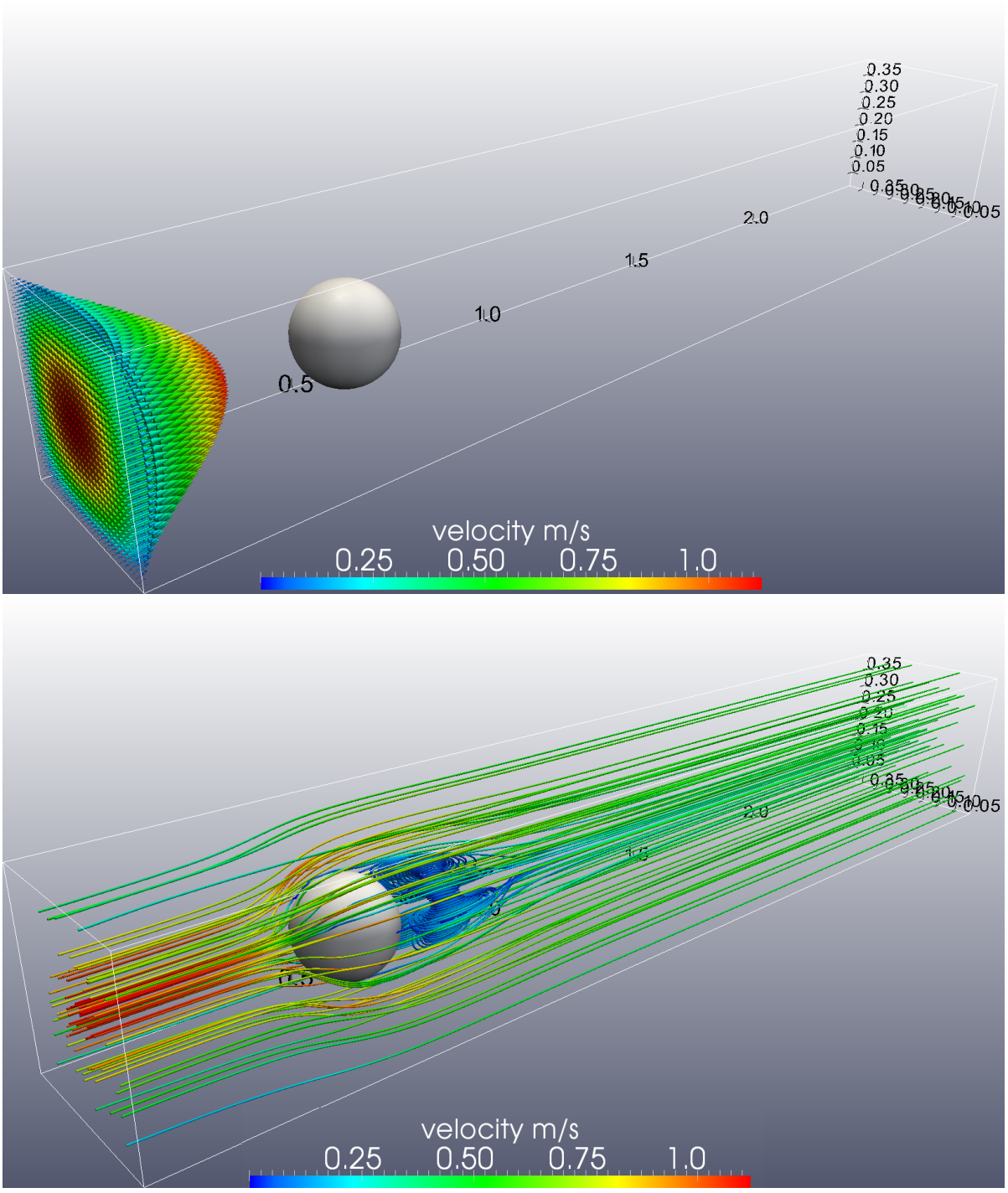

Fig. 4.3: Top: Start configuration for the benchmark problem of a flow round a sphere approximated by the level set technique. A double parabolic profile at the left wall is set as inflow profile and the right side acts as an open end. The boundary condition at the surface of the sphere is set by the described interpolation scheme. Bottom: Simulated flow situation after 2 s visualized by streamlines in ParaView. A recirculating zone behind the sphere has evolved. This stationary vortex has a complex structure of subvortices.

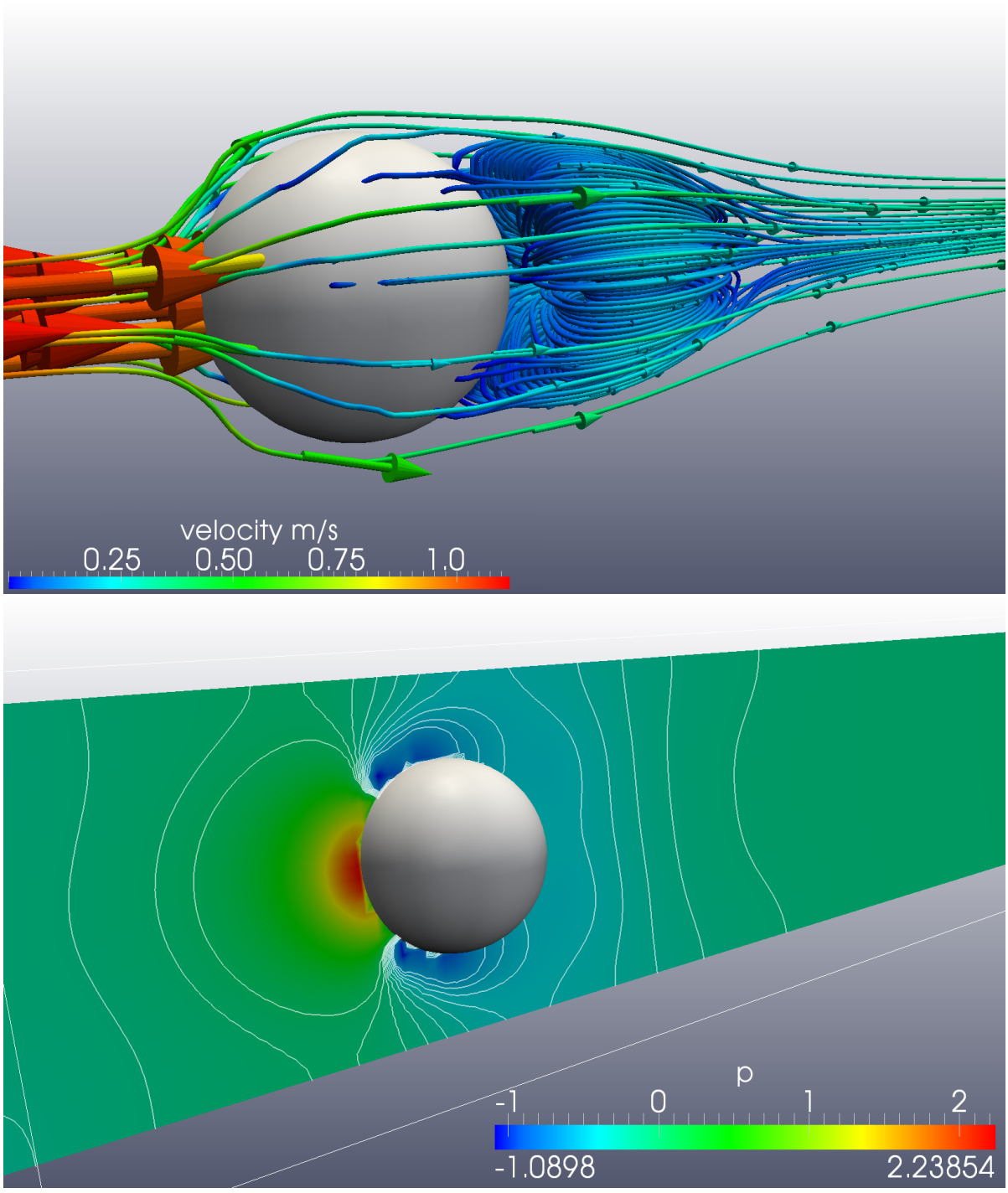

Fig. 4.4: Top: A detailed view at the streamlines demonstrating the recirculating vortex system behind the spherical obstacle. Intersecting streamlines with the obstacle can be considered as visualization artefacts. Bottom: Contour plot of the pressure distribution on a vertical cross section. As expected, a pressure peak in front of the obstacle emerges and at the lateral sides two low pressure zones are formed.

5 Numerical results for the Navier Stokes solver

To demonstrate the new geometry approach and its applicability to relevant examples in the field of fluid dynamics, two numerical fluid simulations are presented. The first example shows a single phase flow round a combination of objects in an elongated channel and the second simulation presents the two phase flow round a tripodal object.

5.1 Single phase flow around complex object

At first the applicability to a real fluid flow including complex obstacles is demonstrated. In the following the single phase model is applied to simulate the flow round several combinations of objects which combine all possible challenges for the geometry handling. Curved surfaces, kinks, and complex unions are chosen to test the flexbility of the approach in one example.

5.1.1 Experimental setting

The first example a combination of three obstacles is regarded. First, a tilted cylinder is chosen which intersects the grid lines and does not follow the grid structure. Further downstream the union of two spheres builds a second asymmetric object with sharp bends and kinks. Third and finally, a union of two perpendicular cylinders is placed behind of the spheres. All together, three objects placed behind each other are treated by the presented level set geometry approach. The modified pressure projection is used to solve the Navier Stokes equations, whereas the described new methods to treat the boundary conditions are applied. All used parameters and the whole setting are summarized in Table (5.1) with a spatial resolution of $(150 \times 20 \times 20)$ grid cells. Figure (5.1) summarizes the starting configuration for this example.

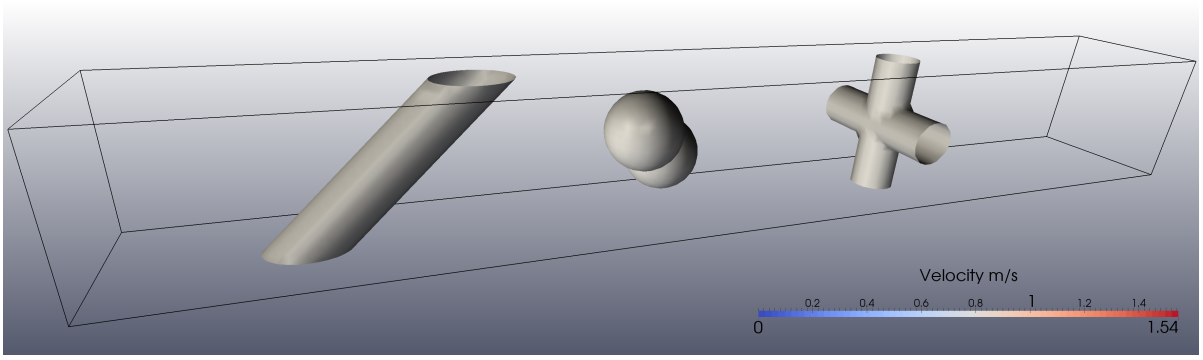

Fig. 5.1: Top: Starting configuration for the single phase flow round complex obstacles. The flow direction is from the left to the right and a constant velocity $u = 0.45$ is set to the left wall. A tilted cylinder, two intersecting spheres, and a cross composed of two perpendicular cylinders are placed in the channel whose dimensions are $3.0 \times 0.4 \times 0.4$. All obstacles are treated by the new level set geometry approach. At the sides Dirichlet boundary conditions $\mathbf{u} = 0$ are imposed to model the noslip walls. As in already seen in the previous examples, a homogeneous Neumann boundary condition is set to create an open outlet at the right end of the channel.

Table 5.1: Computational parameters and setting for the single phase problem presented in Figure (5.1).

Dimensions	Tfin	Re	Temporal	ConvectiveTerms	PoissonSolver	it_{max}	ε
$3.0 \times 0.4 \times 0.4$	8.0	3000	Euler 1st	VONOS	BiCGStab	5000	10^{-12}

5.1.2 Evaluation and discussion of the numerical result

The described example is calculated on three nodes of the Siebengebirge HPC cluster in the Institute for Numerical Simulation, University of Bonn. Each node consists of four eight-core Intel Xeon 2.226 Ghz processors with 512 GB RAM. This results in 96 CPUs total. All nodes are connected by an Infiniband 56 Gb/sec network which ensures a highly parallel computation system. The computational time for this simulation on this system is 56 Minutes. Moreover, in Figure (5.2) the number of iterations is plotted needed by the BiCGStab to solve the Poisson matrix in each time step up to the residual error $\varepsilon \leq 10^{-12}$. In general the average number of iterations needed in each step is $\overline{n} = 1437$. Furthermore, the time step width dt is chosen adaptively during this simulation and the mean time step is $\overline{dt} = 0.004797$. Figure (5.4) demonstrates the temporal evolution of the flow field in the channel, where the first three images present the initial first second.

After an initial phase the flow stabilizes and only small differences occur. The vortices behind the cylinder and the spheres evolve during the first $0.5\,s$ of the simulation and become steady, while the lateral flow passing the cross and the complex eddy behind the cross forms gradually. After $1.4\,s$ the vortex construct containing eight contrarotating vortices has developed at the back of the cross and persists in its basic form for the rest of the simulation, compare Figure (5.5) and Figure (5.6).

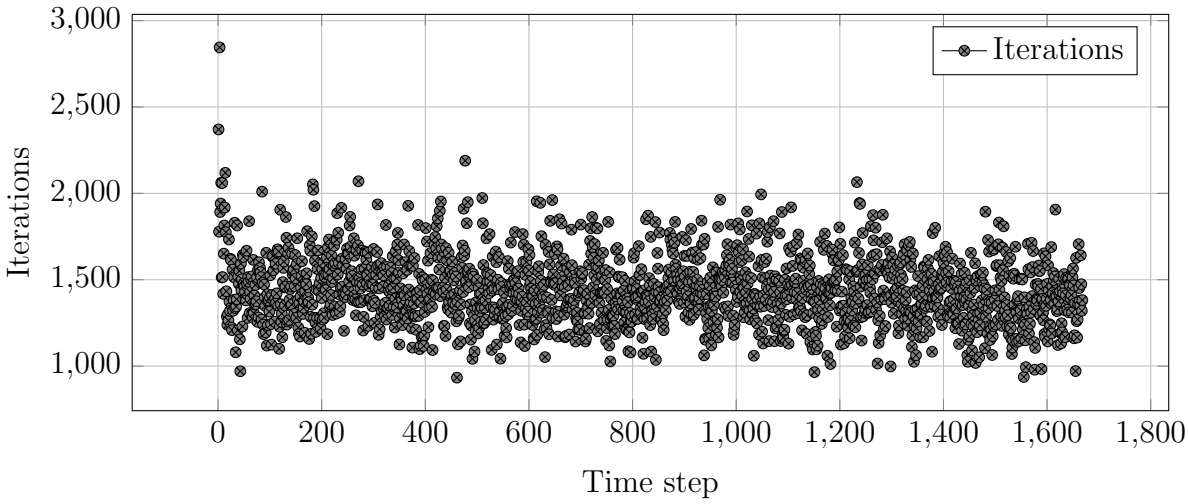

Fig. 5.2: Numbers of iterations needed in the BiCGStab solver to solve the Poisson matrix in each time step up to $\varepsilon \leq 10^{-12}$. The average number of iterations to solve the problem is $\overline{n} = 1437$ with an average time step width $\overline{dt} = 0.004797$.

5.1.3 Conclusion

The numerical simulation with the level set geometry approximation provides satisfactory results despite the complex structure of the obstacles and this relatively coarse resolution. The complex union of the spheres and the not grid aligned obstacles are resolved sufficiently in this resolution. In detail, Figure (5.7) shows a zoomed view of the flow near the spheres. Fine structures near the geometry surface like vortices and the flow separation are well resolved. Furthermore, regarding the resolution of the obstacles the level set approach has considerable advantages in comparison to the flag field geometry approach. Figure (5.3) compares the same geometrical setting in both techniques. On the one hand the geometry is resolved by the flag field approach and on the other handled by the described level set geometry technique. Obviously the flag field technique

is not able to reproduce crucial properties of the obstacles. Bent surfaces and not grid aligned straight parts are only captured by the new level set approximation. Moreover, the new algorithm to impose the boundary conditions leads to an exact interpolation of the boundary values up to the order of the interpolation scheme.
In summary, a single phase simulation of a flow round arbitrarily shaped obstacles is feasible with the presented geometry approximation and leads to satisfactory results even on coarse grid resolutions.

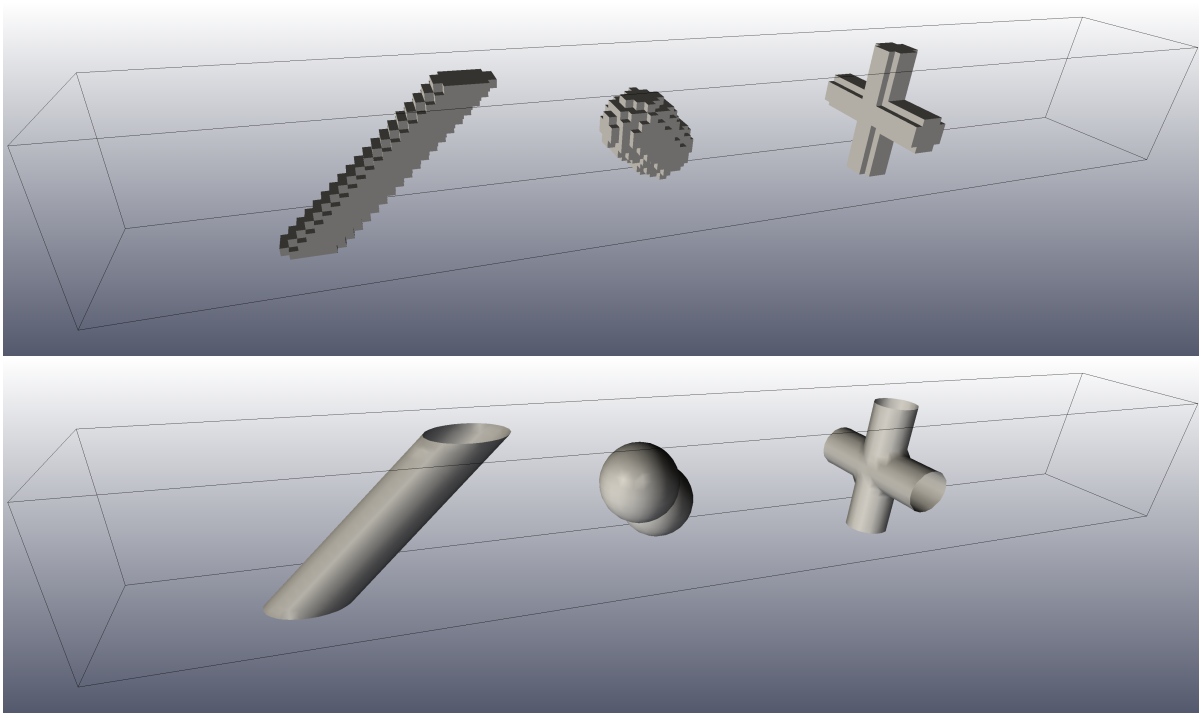

Fig. 5.3: Direct comparison between the flag field technique (top) and the new developed level set approach (bottom) to discretize the obstacle on the same grid resolution. Obviously the flag field technique is not able to resolve the bent surfaces, kinks, or straights which are not grid aligned. Here, the level set approach sufficiently resolves all obstacles and provides a robust method to simulate the flow round arbitrarily shaped objects on coarse resolutions.

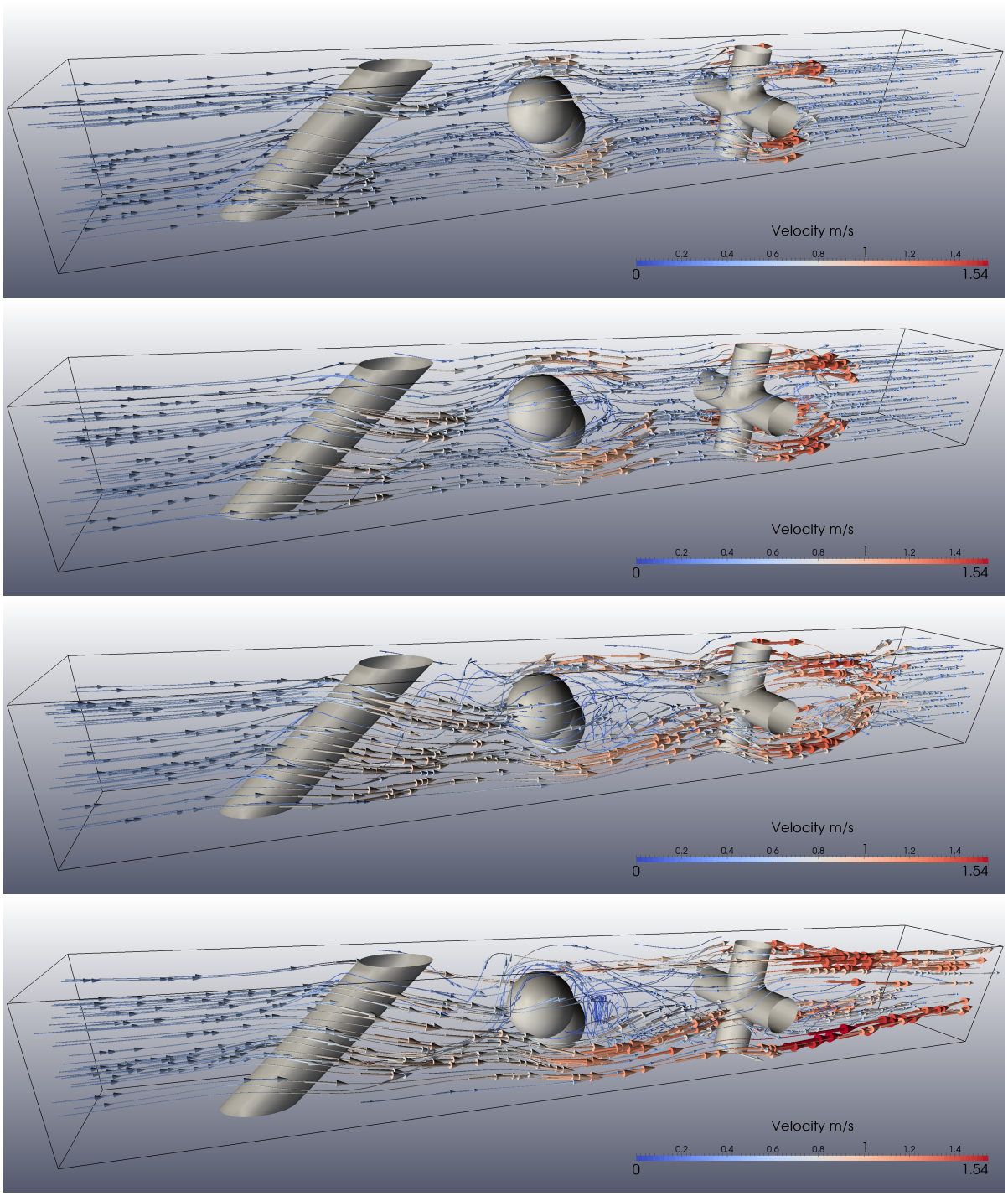

Fig. 5.4: Temporal evolution of the flow field and the streamlines in the channel. The simulation time steps $t = \{0.2\,s, 0.5\,s, 1.0\,s, 8.0\,s\}$ from top to bottom illustrate the unfolding of the current. After $0.5\,s$ the eddy system has established behind the first two obstacles. Further downstream the current splits to pass the cross. Behind that cross there develops a complex symmetric vortex. For a more detailled description of this vortex see Figure (5.6).

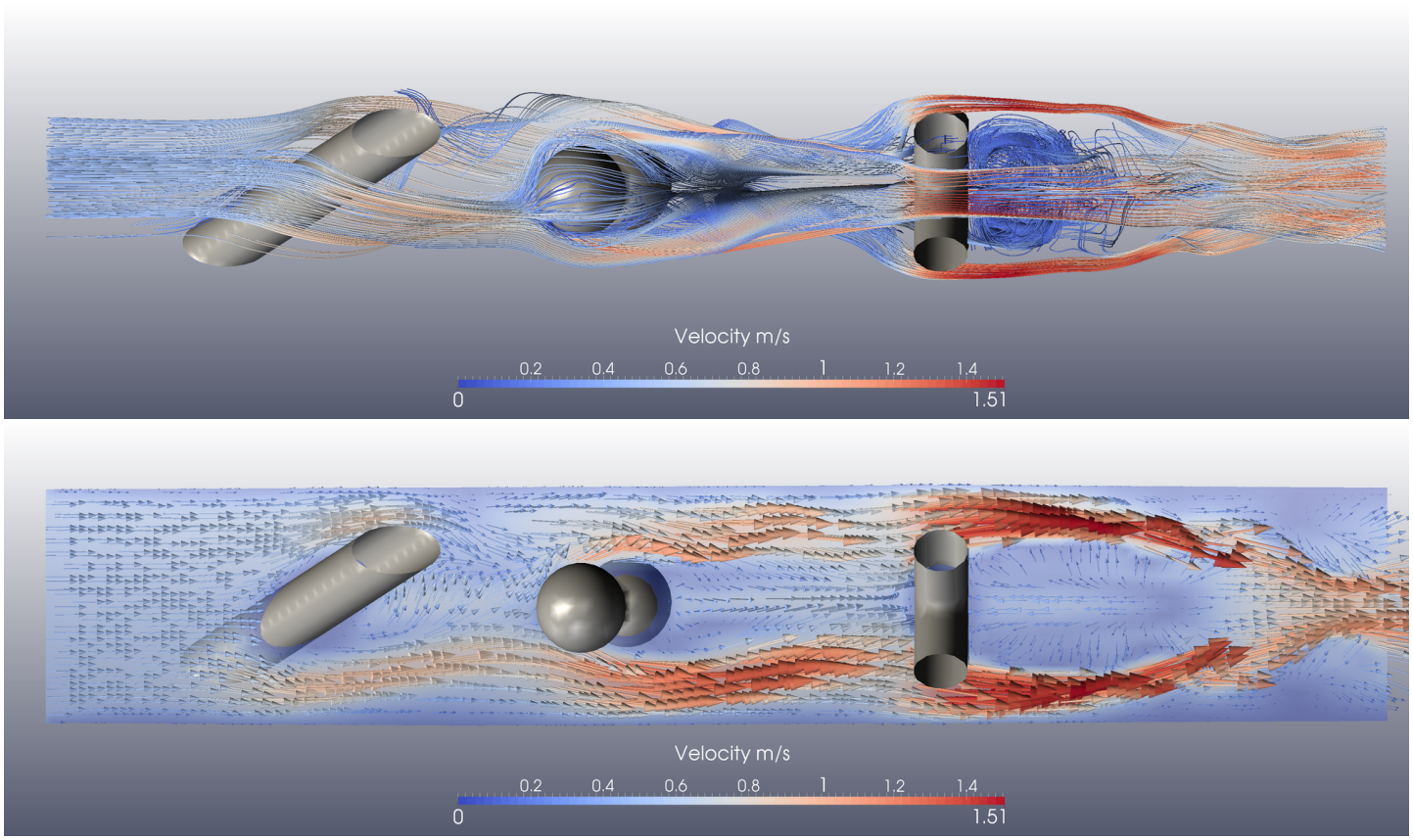

Fig. 5.5: Top: Streamlines visualisation of the flow at $t = 1.4s$. A complex vortex and flow structure evolves around the level set obstacles. The flow direction is from the left to the right. Due to the tilted arrangement of the cylinder an upward vortex develops behind the first obstacle. The spheres affect the flow, such that it forms a recirculating vortex zone which transitions into the upstream flow of the cross. Here, the flow separates into four parts. Each part passes through one quarter of the cross and forms two contrarotating vortices. Consequently, a vortex system consisting of eight subvortices arises when the flow combines behind the obstacle.
Bottom: The visualisation of the velocity vectors on a slice through all obstacles demonstrates the recirculating zones behind the obstacles of the lateral flows. Here, an acceleration of the lateral flows is observed.

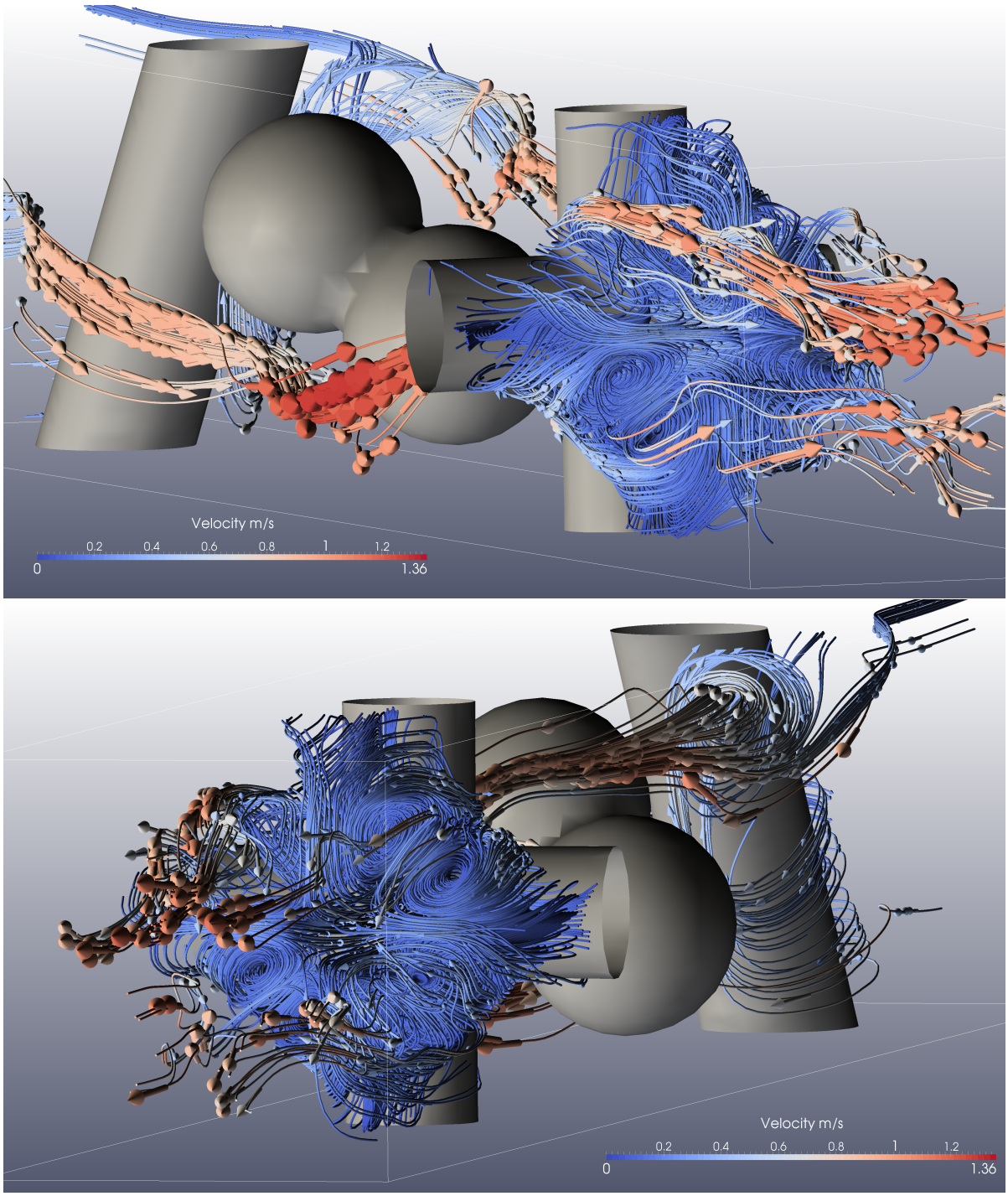

Fig. 5.6: Visualisation of the flow field near the level set obstacles at the time step $t = 1.4\,s$ from the right (top) and the left (bottom). After passing the tilted cylinder and the spheres the flow separates to flow round the cross composed of two cylinders. Behind the cross eight contrarotating vortices form a complicated flow structure. In each quarter of the region there are two vortices that rotate in opposite directions.

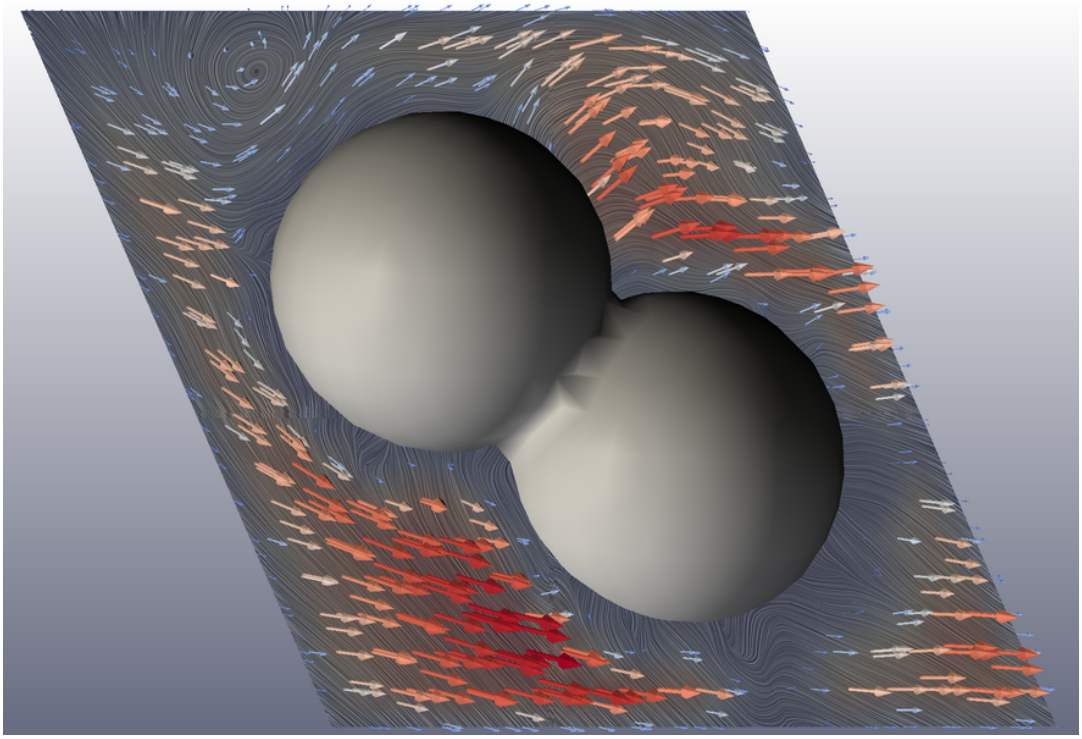

Fig. 5.7: Surface LIC visualisation of the velocity field near the union of the spheres. The slice cuts the spheres in their middle. In the upper left corner a vortex is visible. Similarly, small scale structures have emerged in the lower right section of the slice. Additionally, the three dimensional velocity vectors at the cut of the slice with the flow field highlight the complex flow situation near the obstacle.

5.2 Two-phase flow round tripodal complex object

In contrast to the single phase example before, a two phase flow needs a sufficiently well transported free surface. Here, the geometry approach shows its advantages in a coarse resolution for the boundary condition treatment of the free surface level set function ϕ_f. Inspired from the flow over a weir, and the flow round an obstacle the example is composed as follows.

5.2.1 Experimental setting

The obstacle is constructed from three tilted cylinders which underpin a spherical obstacle. Thus, a union of four level set obstacles results in a tripodal obstacle which is positioned

Table 5.2: Computational parameters and setting for the two phase flow problem and the flow round the tripodal object presented in Figure (5.8).

Dimensions	Temporal scheme	Convective scheme	PoissonSolver	it_{max}	ε
$12.0\,m \times 3.6\,m \times 4.0\,m$	AdamsBashforth 2nd	QUICK	BiCGStab	3200	10^{-9}

surface tension σ	μ_l	μ_g	ρ_l	ρ_g	Tfin
$7.2 \cdot 10^{-2}\,N/m$	$10^{-3}\,kg/(m \cdot s)$	$1.7 \cdot 10^{-5}\,kg/(m \cdot s)$	$1000\,kg/m^3$	$1.3\,kg/m^3$	$20.0\,s$

in the middle of a channel such that the free surface of the fluid intersects at the middle of the sphere. Additionally, a backward facing step is placed at the inflow inlet of the channel. This step is fully resolved by the flag field technique. The use of this step is to create a recirculating vortex such that a realistic flow situation can evolve. Here, the spatial dimensions are $12\,m \times 3.6\,m \times 4.0\,m$ with a grid resolution of $120 \times 36 \times 40$ which results in an equidistant grid size $dx = dy = dz = 0.1\,m$. The inflow velocity is set to $1\,m/s$. All density and viscosity values are chosen such that a realistic air and water system is realized. The surface tension $\sigma = 7.2 \cdot 10^{-2} N/m$ is chosen likewise. All numerical and physical parameters are listed in Table (5.2).

5.2.2 Evaluation and discussion of the numerical results

The numerical simulation is calculated on six nodes of the Atcama HPC cluster in the Institute for Numerical simulation, University of Bonn. Each node consists of 4 Intel(R) Xeon(R) CPU E5-2650v2 with $2.60\,GHz$ which are quad core CPUs with $64GB$ RAM. This results in 96 CPUs total. The nodes are connected by an Infiniband $56\,Gb/s$ network which ensures a highly parallel computation system. The computational time for the simulation on this system is $7\,h$ with an average time step width of $\overline{dt} = 0.003907$. For the solution of the Poisson equation an average number of iterations is calculated as $\overline{n} = 1704$.

In Figure 5.9 the temporal evolution of the free surface and the vortex system in the liquid phase are presented. A wake near the tripod is visible and generates waves and disturbances at the side and behind of the obstacle. A symmetric vortex in the liquid phase establishes and a symmetric wake of the surface round the obstacle. In the liquid phase two counter rotating vortices evolve behind the tripod. This symmetric wake pattern passes the obstacle during the simulation. A similar evolution of the vortex system in the liquid phase is visualized by streamlines. Here, the symmetric vortex emerges as

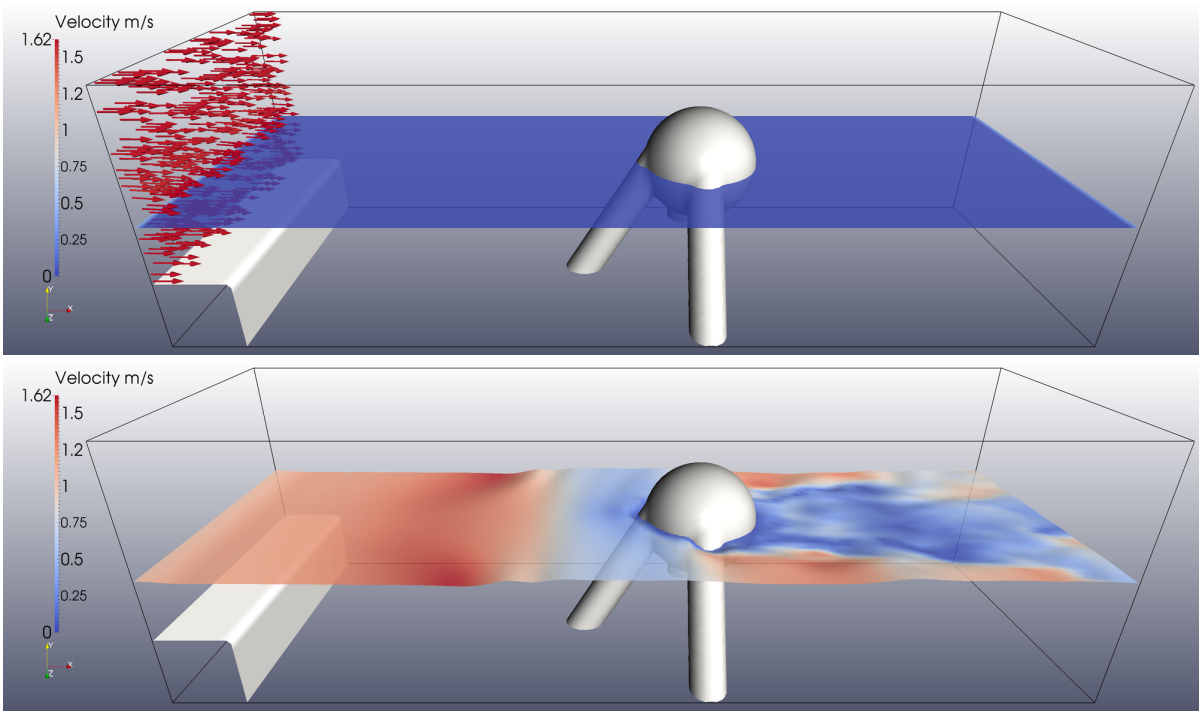

Fig. 5.8: Top: Starting configuration for the two phase flow round a tripodal obstacle treated by the level set geometry approach. Initially the liquid phase and the gas phase in the domain are in rest. With a constant inflow velocity from the left to the right a flow establishes near the obstacle.
Bottom: Final simulated flow situation after 20 s. A symmetric wake at the obstacle has evolved. For simplicity the inflow profile is not visualized again, because it is constant over time.

observed in the free surface. After the initial phase both visualisations show a steady flow adjusting round the obstacle.

5.2.3 Conclusion

Similar to the single phase flow example, a flow round a complex level set obstacle is simulated. But in this example the interaction of a two phase flow is also studied. A correct boundary handling for the transport of the level set function and the reinitialisation process is demonstrated. Additionally, the computational resolution of the domain is moderate. Due to the presented obstacle handling approach by a level set technique the tripodal obstacle and the flow are well resolved. Furthermore, a realistic water and air flow simulation is presented in a manageable grid resolution.

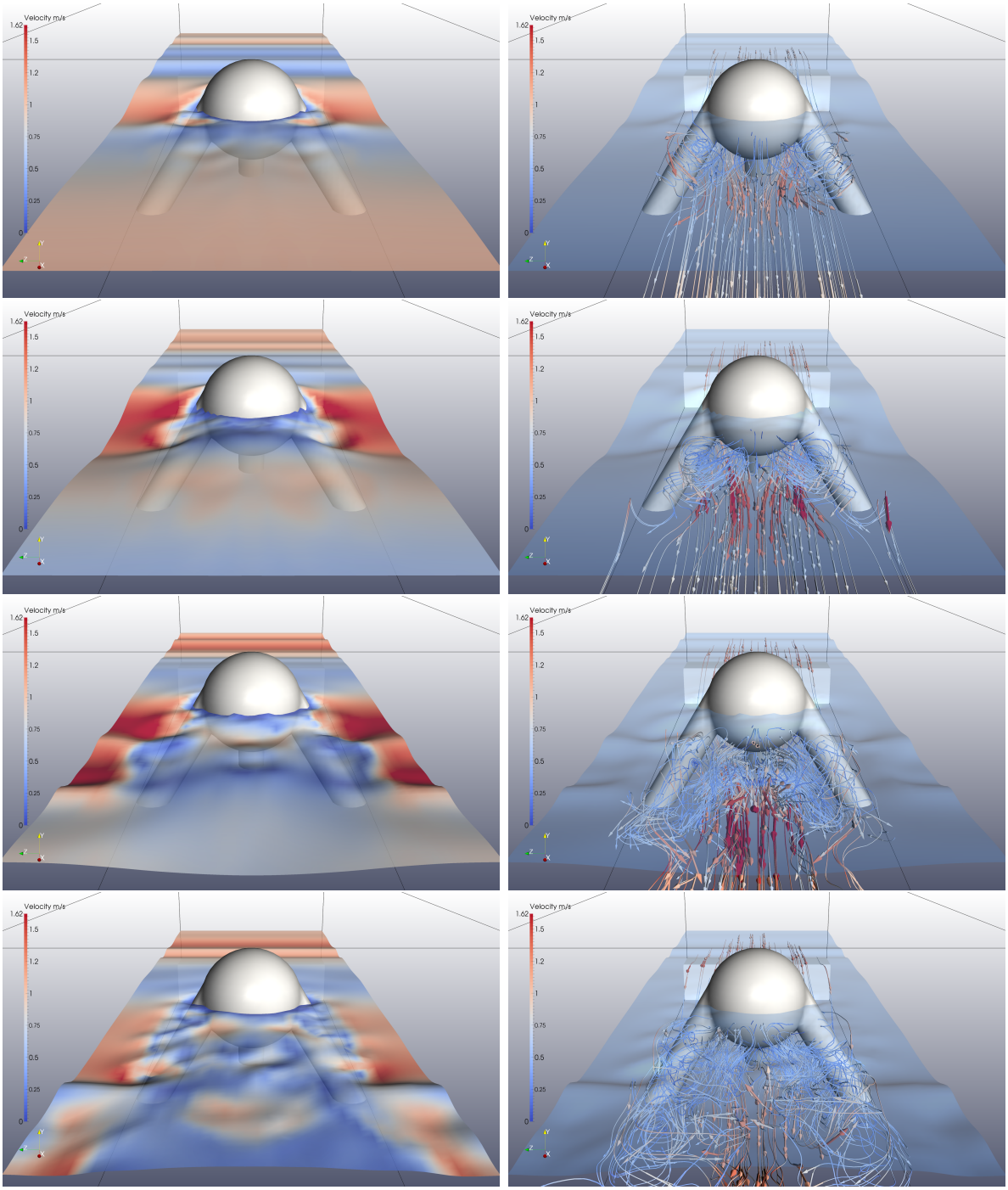

Fig. 5.9: Visualisation of the flow field around the tripodal level set obstacles at the time steps $t = \{3.70\,s, 4.95\,s, 7.45\,s, 9.95\,s\}$. The flow is into the viewers direction. On the left the free surface is colored in the velocity magnitude of the surface velocity vectors. The right column shows the free surface and the streamlines visualisation of the flow in the liquid body (water).

Part II

Sediment transport models for two phase fluid flows

6 Sediment models for the suspension and the bed load transport

In the following chapter the Navier Stokes solver on arbitrary domains from the first part is used to simulate current driven sediment transport processes. In this connection two sediment models are introduced and used to model the two major parts of the sediment transport caused by a moving fluid. Both models arise from first principles. In general, the sediment transport is separated into the bed load and the suspension load. On the one hand the bed load transport comprises the material which is transported near the sediment bed and has at least periodical contact with the sediment bed. On the other hand every other material which is in motion and has no contact to the sediment bed is collectively termed as suspension load. In the bed load equation the balancing of incoming and outgoing masses results in a changing sediment surface. Likewise, the conservation of mass is the main idea for an advection diffusion equation to model the suspension concentration transport. With the aid of empirically derived formulas and parameters the fluid velocity is the main input value in both models. In both equations the fluid velocity represents a transport velocity and with the transported material the sediment surface changes over time. Furthermore, the interchange of the masses between both models by the source and the sink terms, and also all the necessary boundary conditions are discussed.

6.1 Bed load model

The bed load as the first part of the sediment transport is described by transport formulas. These formulas are derived from experimental and field work and have ranges of applicability. Beside these ranges of applicability the shear stress is an important factor in these transport formulas. Both, the concept of shear stress and the transport formulas are empirically derived or equipped with empirical constants. As a consequence of the

bed load transport the sediment surface changes and typical bedforms evolve. The following section discusses the temporal evolution of the sediment surface which is described and modelled by Exner's bed level equation. After that selected transport formulas and shear stress models are presented.

6.1.1 Exners bed level equation

The sediment bed beneath a running water is modelled as an elevation level from an underlying plane $P = \left\{(x_i)_{i=\{1,2,3\}} \in \mathbb{R}^3 \,|\, x_2 = 0\right\}$. Every point $x = (x_i)_{i=\{1,2,3\}}$ on the sediment surface Ω_s defines a distance or in this case a height $h(x_p)$ from the point $x_p \in P$. The sediment surface Ω_s represents the interface between the sediment body and the fluid body. This height h is defined as

$$h(x_p) = x_2 \quad h : \mathbb{R}^2 \longrightarrow \mathbb{R}, \tag{6.1}$$

i.e. the length of the perpendicular line from P to the sediment surface is given by the second coordinate x_2. Thus, the sediment surface Ω_s is defined as

$$\Omega_s = \left\{x \in \mathbb{R}^3 \,|\, x = (x_1, h(x_p), x_3) \text{ with } x_p = (x_1, x_3)\right\}. \tag{6.2}$$

Figure (6.1) illustrates the bed level setting for the sediment surface.
In the following, the temporal evolution of the height function h will be modelled by the bed level equation from Exner (1925). In this model the change of the height h is caused by a difference of the incoming and outgoing sediment masses in a control volume. From the conservation of mass, Exner (1925) derived the following equation

$$\frac{\partial h}{\partial t} = -\nabla \cdot q_s(\tau(u)) \qquad \forall x \in P \tag{6.3}$$

where h denotes the aforementioned height function and q_s represents the transport formula which depends on the shear stress $\tau(u)$. Furthermore, the shear stress depends on the fluid velocity u. In the literature several derivations of equation (6.3) were presented, compare Exner (1925), Van Rijn (1984), Knighton (1998), or Zanke (2002). Coleman & Nikora (2009) derived the bed level equation (6.3) starting from a temporal and spatial averaging process. A lot of previous morphological and sedimentary studies used Exner's equation to predict or calculate the morphological changes of the sediment bed due to

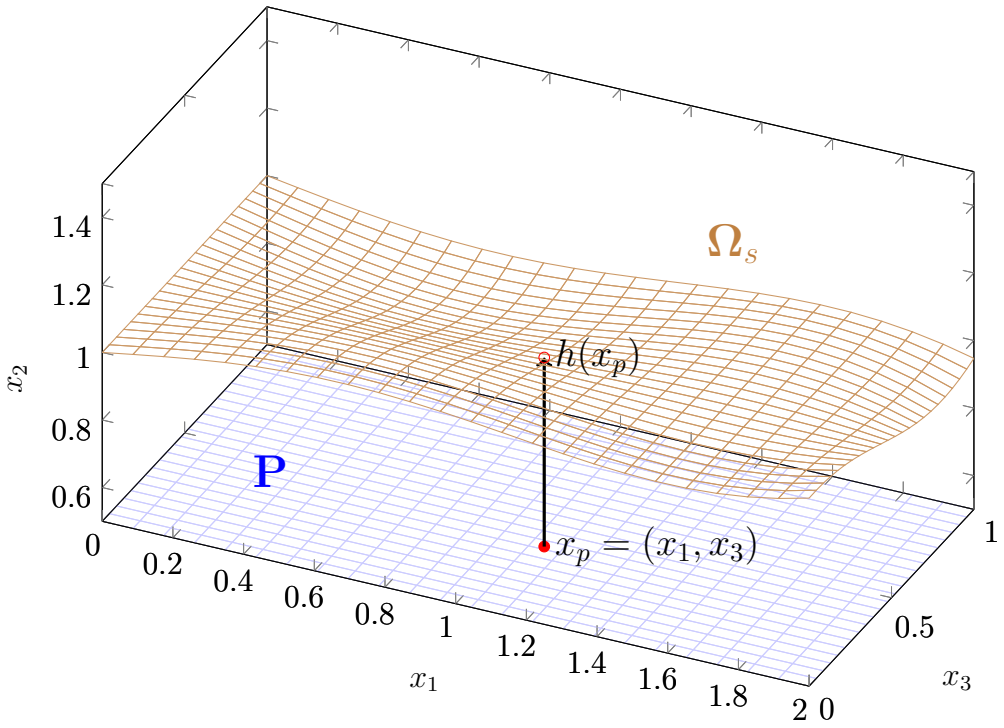

Fig. 6.1: Schematic view of the sediment surface Ω_s with the underlying plane P. The height value $h(x_p)$ represents the distance from the point x_p from Ω_s.

sediment transport. Without any claim of completeness in the following studies Exner's bed level equation was used as the morphological model, compare Parker (2004), Paola & Voller (2005), Zhang et al. (2005), Roulund et al. (2005), Kubatko et al. (2006), Kubatko & Westerink (2007), Long et al. (2008), Khosronejad et al. (2011), Khosronejad et al. (2012), and Dixen et al. (2013).

In equation (6.3) the possibility to introduce source and sink terms was omitted. However, if two additional terms Q_b and S_b are added on the right hand side of the bed level equation, the coupling of the bed surface model with a suspension load model and vice versa is achieved. Note here, that two terms are added. One term Q_b represents the sources and the second term S_b denotes the sinks. Therefore, the sign of the terms is fixed and both terms are positive.

A typical choice for the boundary condition is the homogenous Neumann boundary condition which reflects the natural behaviour of the sediment in a box. The bed level

equation extended by Q_b and S_b and the related boundary conditions read as

$$\frac{\partial h}{\partial t} = -\nabla \cdot q_s(\tau(u)) + Q_b - S_b \qquad 0 \leq Q_b, S_b, \forall x \in P \tag{6.4}$$

$$\frac{\partial h}{\partial n} = 0 \qquad \forall x \in \Gamma_P \tag{6.5}$$

where the boundary normal is denoted by n. The sink S_b and the source Q_b are discussed in detail in Section (6.3).

Table 6.1: Grain size categories after DIN 4022

Size terms		**Diameter** in mm
Boulders	boulders	$200 < d$
	cobbles	$63 < d < 200$
Pebbles	coarse	$20 < d < 63$
	medium	$6,3 < d < 20$
	fine	$2 < d < 6,3$
Sand	coarse	$0,63 < d < 2$
	medium	$0,2 < d < 0,63$
	fine	$0,063 < d < 0,2$
Silt	coarse	$0,02 < d < 0,063$
	medium	$0,0063 < d < 0,02$
	fine	$0,002 < d < 0,0063$
Clay	coarse	$0,00063 < d < 0,002$
	medium	$0,0002 < d < 0,00063$
	fine	$0 < d < 0,0002$

6.1.2 Transport formulas

The transport formulas q_s which determine the amount of bed load transported by a certain velocity are a topic of extensive research for decades (e.g. Shields (1936), Meyer-Peter & Müller (1948), Einstein (1950), Engelund & Hansen (1967), Bagnold (1966), Yang (1972), Ackers & White (1973), Van Rijn (1984), and Pacheco-Ceballos (1989)). Therefore, numerous transport formulas for various different application types are availa-

ble. A comprehensive summary can not be presented here, but a few hydraulic engineering standard references are named, where a detailled discussion of the different bed load formulas is presented (Van Rijn (1993), Knighton (1998), Roberson et al. (1998), Chanson (1999), Zanke (2002), White (2003), and Sedimentation & River Hydraulics Group (2006)). Many authors of transport formulas use the concept of a critical shear stress value τ_c that determines the limit for a motion of the sediment, e.g. Shields (1936), Meyer-Peter & Müller (1948), Van Rijn (1993), and Zanke (2002). When the shear stress τ reaches the critical value τ_c the transport starts and the sediment is transported. This value for τ_c depends on several intrinsic factors. The size, the shape, the roughness, the packing structure, cohesive forces and other biological components change τ_c in the fluid. Here, the empirical character of the models is conveyed. The concept of a critical shear stress is closely related to a critical velocity acting on the sediment surface. In Figure (6.2) the empirically derived Hjulstroem diagram (Hjulstroem, 1955) presents the dependence of the transport state of a particle on the velocity and the medium grain size d_{50}. Moreover, Julien (1995) collected different values for the size categories of the sediment particles which are summarized in Table (6.2).

Table 6.2: Critical shear stress for the grain size categories, compare Julien (1995). Note here, the differences in each category are caused by different shape, roughness, density, and other parameters.

			$0,029$				
			$0,033$		$0,047$		
Clay	$0,165$	Silt	$0,048$	Sand	$0,044$	Pebbles	$0,052$	Cobbles	$0,054$
	$0,250$		$0,072$		$0,042$		$0,050$		
			$0,109$		$0,039$				

The transport model after Meyer-Peter & Müller (1948) is the first transport formula which is discussed in detail. The formula was empirically derived from experimental data by Meyer-Peter & Müller (1948). In its commonly used form the Meyer-Peter & Müller formula reads as follows

$$q_s = \begin{cases} \sqrt{(s-1)gd_s^3} \cdot \left(\frac{4\tau}{\rho(s-1)gd_s} - \tau_c\right)^{\frac{3}{2}} & \tau_c \leq \tau \\ 0 & \text{else} \end{cases}, \tag{6.6}$$

where τ denotes the shear stress, d_s describes the medium grain size, ρ denotes the

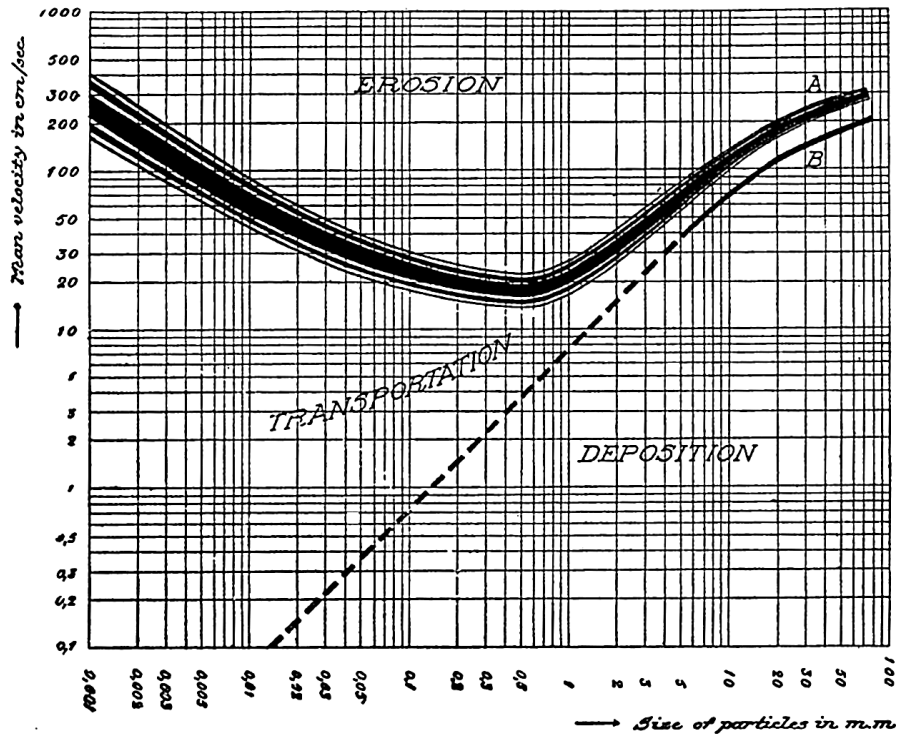

Fig. 6.2: The Hjulstroem diagram describes the transport state resulting from the velocity in correlation to the grain size. On the x-axis the grain size is given in mm, whereas on the y-axis the mean velocity is given in cm/s, compare Hjulstroem (1955). The dashed line represents the settling velocity of particles of a certain grain size. Above that line particles are transported. Accordingly the deposition starts when the mean velocity drops below. Note, that silt particles are moved with the lowest velocity. In contrast, smaller clay particles form more stable phases due to cohesive effects.

fluid density and $s = \rho_s/\rho$ defines the ratio of the sediment density ρ_s and the fluid density. Additionally, the gravity is denoted by g and the critical shear stress by τ_c. Furthermore, the concept of a critical threshold for the motion of particles is obvious in equation (6.6). The Meyer-Peter & Müller formula was used as transport formula in previous morphological studies to calculate the bed load. For example, Mewis (2002), Zhang et al. (2005), Link (2006), Bechteler (2008), and Mewis (2009) calculated the bed load with the Meyer-Peter & Müller formula and investigated the sedimentary processes under various situations, like the scouring at obstacles or the redeposition of entrained material. In contrast to the Meyer-Peter & Müller formula, Engelund & Hansen (1967) proposed a formula which does not incorporate a concept for a critical shear stress. In a

natural river the grain size distribution comprises all grain size categories and therefore a constant movement of single particles is present at any velocity. To this end, the range of application of this model is different in scale and property of the sediment compared to the Meyer-Peter & Müller formula. The Engelund & Hansen formula reads

$$q_s = \frac{0.1}{f_{eh}} \cdot \left(\frac{\tau \cdot \rho_f}{g d_s (\rho_s - \rho_f)} \right)^{\frac{5}{2}} \tag{6.7}$$

where τ denotes the shear stress, the fluid and the sediment densities are in turn described by ρ_f and ρ_s. The medium grain size is denoted by d_s and the gravity by g. Additionally, a friction coefficient after Engelund & Hansen (1967) is denoted by f_{eh} which choice is empirically. The usage of the Engelund & Hansen formula was widely investigated and validated, compare Heathershaw (1981), Van Rijn (1993) Bayram et al. (2001), and Wu & Julien (2004). In summary, the Engelund & Hansen formula acts as one alternative draft in the wide range of approaches to transport formulas which use the concept of a critical shear stress.

6.1.3 Shear stress models

The shear stress τ is calculated as the gradient of the velocity in the normal direction n to the surface evaluated at the boundary. In general, given the fluid viscosity μ, the shear stress τ is defined as

$$\tau(x) = \mu \frac{\partial u}{\partial n} \qquad \forall x \in \Omega_s. \tag{6.8}$$

While the experimental measurement of the shear stresses is not feasible on the bed at any location, the computation of the shear stress is an major issue in the calculation of the sediment transport. Therefore, several approaches for estimating τ in a water body were presented in the literature. Knighton (1998), Roberson et al. (1998), Chanson (1999), and Zanke (2002) present different empirical or semi empirical models. Here, the shear stress model after Chanson (1999) is exemplary and demonstrates the difficulties accompanied with the usage of these empirical models. The approach reads as

$$\tau(x) = \frac{1}{8} \rho_f f \|u\|_2^2 \tag{6.9}$$

where the fluid density is given by ρ_f and f denotes an empirical factor which is presented in Table (6.3).

Table 6.3: Empirical models for the friction coefficient f given by Chanson (1999), p 77. Reynold's number Re is the main component in these models. The terms 'turbulent conditions' and 'more turbulent conditions' illustrate the dependence of this empirical derived model to the experience of the users of the formula. Here, R denotes the hydraulic radius and k_s the friction factor after Manning (1891) and Strickler (1923).

$Re < 2000$	$f = \frac{64}{Re}$
$Re < 10000$	$f = \frac{0.3164}{Re^{\frac{1}{4}}}$
$Re > 10000$	$\frac{1}{\sqrt{f}} = 2.0 \cdot \log_{10}\left(Re \cdot \sqrt{f}\right) - 0.8$
'turbulent conditions'	$\frac{1}{\sqrt{f}} = 2.0 \cdot \log_{10}\left(\frac{k_s}{3.71 \cdot R} + \frac{2.51}{Re \cdot \sqrt{f}}\right)$
'strong turbulent conditions'	$\frac{1}{\sqrt{f}} = 2.0 \cdot \log_{10}\left(\frac{R}{k_s}\right) + 1.14$

In the following, due to its locality property and the easy calculation of the gradient at the boundary, equation (6.8) is used to calculate τ. This represents a significant advantage in comparison to empirical approaches like the equation (6.9).

6.2 Suspension load model

The suspension load as the second major part in the total amount of the transported material comprises all material which is transported in the whole fluid. Here, the distinction between bed load and suspension load is unclear. Jumping particles leaving the sediment surface for a short time and settling down again after some distance travelled are part of the bed load even if these particles leave the original bed load layer. An advection diffusion model is used to describe the transport of the suspended material. Moreover, a gravitational term describes the settling of particles due to gravity forces.

6.2.1 Advection diffusion model

Since only very fine grains are transported as suspended material, the common approach to model suspension load is to regard all the entrained material as a concentration of mass c in the fluid domain. Similar to the bed level equation, the advection diffusion model for the suspended material can be derived from the conservation of mass and

momentum. Malcherek (2004) presents a suspension model as follows

$$\begin{aligned} \frac{\partial c}{\partial t} + u \cdot \nabla c + w_g \frac{\partial c}{\partial y} &= K \Delta c \qquad c(x,t) : \Omega_f \times [0:T] \longrightarrow \mathbb{R} \\ \frac{\partial c}{\partial n} &= 0 \qquad\qquad x \in \Gamma_{\Omega_f} \\ c &= c_{ref} \qquad\qquad x \in \Omega_s \end{aligned} \tag{6.10}$$

where the fluid velocity is denoted by u, the diffusion coefficient is described by K. Typical values for K are very small. Officer (1982) deduced values in the magnitude of $10^{-7}\, m^2/s$ from experimental studies. To take a gravitational transport of particles into account a velocity w_g is added as an additional advection velocity component. On the one hand the Neumann boundary condition in equation (6.10) models a closed border of the fluid domain Ω_f. On the other hand the boundary condition at the sediment surface Ω_s reflects the idea that the layer next to the sediment body has a concentration c_{ref} which is the maximum concentration near Ω_s. This model and similar forms were used to model the transport and the diffusion of the suspended material in various applications and experimental approaches, compare Campos (2001), Marek (2001), Wu et al. (2005), Yoon & Kang (2005), Sedimentation & River Hydraulics Group (2006), Kantoush et al. (2008), Razmi et al. (2009), and James et al. (2010). In all this considerations a single phase flow is regarded.

To extend the advection diffusion model to a two phase flow system with a free surface one needs a model which allows a transport of a concentration across this free surface. A change in the density or the viscosity of the fluids across the interface could be treated by a smooth transition function like the heaviside function (2.34) which was already used in the Navier Stokes solver (Croce, 2002). Nevertheless, the influence of a concentration on the surface tension and the resulting forces cannot be described by this smoothing function. A short selection from several approaches in the literature studying the adsorption and desorption of surfactants from the bulk into the surface can be found in Diamant et al. (2001), Teigen et al. (2011), Garcke et al. (2014), and Barrett et al. (2015). Based on the lack of a model for the adsorption of a sediment concentration, the suspension model is only used in single phase flows which covers most of the practical applications.

6.2.2 Gravitational component

In the advection diffusion equation (6.10) the settling of single particles and its impact on the transport is modelled by a velocity w_g which results from particles settling due to the gravitational forces. A particle is modelled as a falling sphere in a fluid. With Stokes' law as stated in Daintith (2009) a terminal velocity for fine spherical particles can be calculated from

$$w_g = \frac{(\rho_s - \rho_f)/\rho_f g d_s^2}{C_1 \nu}, \tag{6.11}$$

where ρ_f and ρ_s denote the material densities. The gravity, the viscosity, and the grain size are denoted by g, ν, and d_s. Furthermore, the theoretical constant $C_1 = 18$ is only valid for perfect spheres. Additionally, Stokes' law is only valid in low Reynold's number regimes, i.e. $Re \leq 1$. Therefore, many authors developed experimental formulas for different shapes, roughnesses, and velocity regimes, e.g. Hallermeier (1981), Dietrich (1982), Van Rijn (1993), Cheng (1997), and Ferguson & Church (2004). In the following a semi empirical formula presented by Ferguson & Church (2004) is used which reads as

$$w_g = \frac{(\rho_s - \rho_f)/\rho_f \cdot g \cdot d_s^2}{C_1 \nu + \sqrt{0.75 \cdot C_2 \cdot (\rho_s - \rho_f)/\rho_f \cdot g \cdot d_s^3}}. \tag{6.12}$$

This model is an extension of Stokes' law and was fitted to real experimental data from Raudkivi (1998) and Hallermeier (1981). After Ferguson & Church (2004) the second constant C_2 is an asymptotic value for the drag coefficient of the particle. Furthermore, experiments showed that C_2 can reach from 0.4 to 1.2 for shapes varying from spherical to naturally shaped particles. It was tested for different combinations of both constants and in regimes for a higher Reynold's number, i.e. $Re \geq 1000$. For natural sand grains Ferguson & Church (2004) suggest $C_1 = 18$ and $C_2 = 1.0$ but also hint for a maximum limit of $C_1 = 24$ and $C_2 = 1.2$ for extremely angular grains. With this approach the gravitational velocity is constant in the whole fluid domain and the term $\frac{\partial(w_g c)}{\partial y}$ reduces to $w_g \frac{\partial c}{\partial y}$ as presented in equation (6.10). This term is added to a plain advection diffusion equation and leads to model (6.10).

6.3 Interchange between bed load and suspension load

In the complete sediment transport model the masses have to be conserved during the interchange between the bed load and the suspension load depending on the velocity. This interchange is modelled as a source term respectively a sink term in the bed level model. For the advection diffusion equation (6.10) the boundary conditions have to be modified. Here, the concept of a conserving interchange leads to source and sink terms in the bed level equation (6.3). The sink term is motivated by calculating the masses entrained into the suspension load by a velocity v_n normal to the boundary Γ_s. A calculation of this mass leads to a volume which can be recalculated directly into a height difference. A modified approach for the mass flux from the sediment bed into the concentration model proposed by Malcherek (2004) is used here, which reads as

$$S_b = M \cdot (\tau - \tau_c) \frac{\tau}{(\rho_s - \rho_f) g d} \qquad \left[kg/(s \cdot m^2)\right], \tag{6.13}$$

where $M = 2.2 \cdot 10^{-3} s/m$ denotes an empirical material parameter. Therefore, a mass which is set as an source term in the suspension model causes a height loss in the bed level model. This source term is only active if the shear stress τ is bigger than the critical shear stress τ_c. The reverse direction is modelled from the idea that a maximum reference concentration c_{ref} has adjusted in the layer near the boundary. Consequently, the sink term Q_b for the suspension model is defined as

$$Q_b = \max(c(x,t) - c_{ref}, 0) \qquad \left[kg/m^3\right]. \tag{6.14}$$

If the difference between the ambient concentration $c(x,t)$ and the reference concentration is positive, the height difference h_{set} for the bed level equation due to settled or entrained sediment results from the calculation

$$h_{set} = Q_b \cdot dx \cdot dy \cdot dz / (\rho_s \cdot dx \cdot dz) = Q_b \cdot dy / \rho_s \qquad [m]. \tag{6.15}$$

where the control volume is calculated by $dx \cdot dy \cdot dz$.
Both terms are applied only near the boundary. The concept of a maximum concentration near the boundary is valid under the assumption that only the surplus mass Q_b can settle down from the fluid and this consequently results in a height difference h_{set}. Vice versa the reference concentration prevails as long as the sediment bed Ω_s is erodible. Therefore,

the Dirichlet boundary condition in equation (6.10) is introduced. Furthermore, it is common to add a source term in the concentration model from the mass flux S_b with the velocity v_n in normal direction. Thus, the system in (6.10) including the source and sink terms reads as

$$\begin{aligned} \frac{\partial c}{\partial t} + u \cdot \nabla c + w_g \frac{\partial c}{\partial y} &= K \Delta c && c(x,t) : \Omega_f \times [0:T] \longrightarrow \mathbb{R} \\ \frac{\partial c}{\partial n} &= 0 && x \in \Gamma_{\Omega_f} \\ c &= c_{ref} + \frac{S_b}{|v_n|} - Q_b && x \in \Omega_s \end{aligned} \tag{6.16}$$

In summary, an advection diffusion equation is used to model the transport of a concentration of suspended material. This advection diffusion model is equipped with Neumann boundary conditions at the non sediment boundary domains and modified Dirichlet boundary conditions including sink and source terms at the sediment boundary. With this model the interchange between both transport stages is realized and the bed load and the suspension load can transition into each other. An empirically derived diffusion coefficient K, the modelling of the settling velocity w_g, and the empirical mass flux S_b reflect the empirical influence in this model which has to be taken into account during the simulation of the transport process.

6.4 Discretization of the sediment model

This section presents shortly the used discretization techniques. Additionally the resulting time step restrictions and other details of the used schemes are explained.

6.4.1 Exner's bed level equation

The bed level equation and the transport equation are discretized on the same staggered grid like the Navier Stokes solver NaSt3D. The height h is located in the middle of the cell and the fluxes

$$q_s = \begin{pmatrix} q_{sx} \\ q_{sy} \end{pmatrix} \tag{6.17}$$

are situated on the faces of the cells. Figure (6.3) summarizes the locations for the variables.

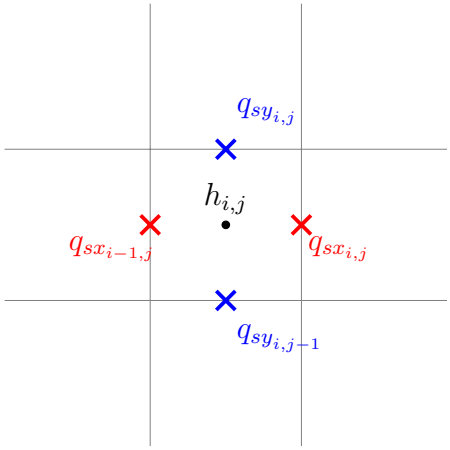

Fig. 6.3: Discretization of the variables h (red) and q_s (blue) from the bed level equation on a staggered grid. The surface height h is located at the cell center, whereas the normal transport fluxes q_s are situated at the edges of the cell.

With this setting the finite differences schemes from the fluid solver are easily applicable. The spatial schemes are restricted to a two dimensional setting, whereas the temporal schemes are applied in the same way as in the discretization of the Navier Stokes equations. For the spatial terms there are schemes like donor cell, SMART, QUICK, or VONOS available. Likewise, an Adams-Bashforth second order time stepping method is applied. For a detailled description of the applied schemes implemented in the setting in NaSt3D compare Griebel et al. (1998) and Croce (2002). As a time step restriction for the explicit Adams-Bashforth scheme the most restrictive CFL condition is used, such that

$$dt = \frac{dx^2 + dy^2}{\max_{ij} \|q_s\|_2}, \tag{6.18}$$

where dx and dy are the spatial grid sizes in case of graded grids. Other less restrictive choices for the time step are discussed in Deriaz (2012). This combination provides a robust full second order method for the bed level equation.

6.4.2 Suspension load model

As already mentioned before, the suspension load model is a modified advection diffusion equation with an additional settling term. As before, the setting from the Navier Stokes is equally applicable. On the one hand the full spectrum of the convective schemes from NaSt3D can be used for the advection term. On the other hand the diffusion term is discretized by the standard laplacian for scalars. Reusing the staggered grid in full three dimensions leads to the same setting as for the bed level equation or the Navier Stokes equations. The scalar concentration c is situated in the cell center, whereas the advection velocity u and the gravitational settling velocity w_g are located at the cell faces. Furthermore, a second order explicit Adams-Bashforth scheme is applied for the time discretization. Choosing this explicit scheme leads to the typical time step restriction for an advection diffusion equation extended by the time step induced by the gravitational settling velocity w_g

$$dt = \min\left(dt_{adv}, dt_{diff}, dt_{w_g}\right). \tag{6.19}$$

Here,

$$dt_{adv} = \frac{dx}{u_{max}}, \qquad dt_{w_g} = \frac{dx}{\max w_g} \tag{6.20}$$

denote the CFL conditions for the advection term and the time step influenced by the additional settling term. The diffusive CFL condition with the diffusion coefficient K is denoted by

$$dt_{diff} = \frac{1}{2K} \cdot \frac{1}{\left(\frac{1}{dx^2} + \frac{1}{dy^2} + \frac{1}{dz^2}\right)}. \tag{6.21}$$

In case of an equidistant grid this condition reduces to

$$dt_{diff} = \frac{dx^2}{6K} \tag{6.22}$$

Note, that the time step restriction arising from the advection term dt_{adv} is the same as the CFL condition for the fluid velocity u.

In summary, a full sediment transport model is developed, discretized, and available. Mass interchanges are modelled by sink and source terms which allow a mass conserving transformation into each other.

7 Slope limiter models

Beside the transport of the particles the critical angle of repose of the sediment has to be modelled. This material specific slope angle denotes a stability criteria for a granular medium. Here, a time dependent diffusion model with a non linear discontinuous coefficient is discretized and solved to obtain a stationary solution for the morphology which obeys all slope limits. In the following a PDE model is developed which describes the change in the surface caused by the sliding of masses following the gradient. On the basis of this slide model a slope limiting model is constructed. Furthermore, the numerical discretization and the solution of the model are discussed.

7.1 Slope properties of granular media

Sand and any other granular media cannot be piled up arbitrarily high. Furthermore, sand or gravel consist of loose particles which follow a force resulting from gravitational and frictional forces. At a certain point the failure of the pile is unavoidable and the masses slide down and form the slopes of the pile of sand. During this process a critical angle of repose α_c evolves and limits the slope angle α, compare Figure (7.1). There are several factors determining α_c, the grain size, the shape of the grain, the roughness and the moisture, to name but a few. Typical values for the angle of repose can be found in Möller et al. (2002) and are summarized in Table (7.1)

Table 7.1: Typical values for the angle of repose depending on the size, the shape and the wetness of the particles following Möller et al. (2002)

Sand	dry	$20 - 30°$
	wet	$20 - 45°$
Pebbles	roundness	$30 - 50°$
Silt and clay	shape and surface properties	$20 - 60°$

In the following all considerations are restricted to an underlying x–z plane P. The function

$$H(x) : P \subset \mathbb{R}^2 \longrightarrow \mathbb{R} \tag{7.1}$$

defines a height function which represents the surface of the granular media. Here, $H(x)$ represents the distance of this surface to the underlying plane P. Consequently, the gradient of H is defined as

$$\nabla H(x) : \Omega \subset \mathbb{R}^2 \longrightarrow \mathbb{R}^2. \tag{7.2}$$

The norm of the gradient $\nabla H(x)$ is a measure for the slope of the scalar field $H(x)$ at the point x. Therefore, the angle α can be derived from

$$\|\nabla H\|_2 = \tan(\alpha) \quad \Rightarrow \quad \alpha = \arctan(\|\nabla H\|_2) \tag{7.3}$$

where $\|\cdot\|_2$ denotes the euclidean length of the vectors. Figure (7.1) illustrates the calculation of the slope angle α.

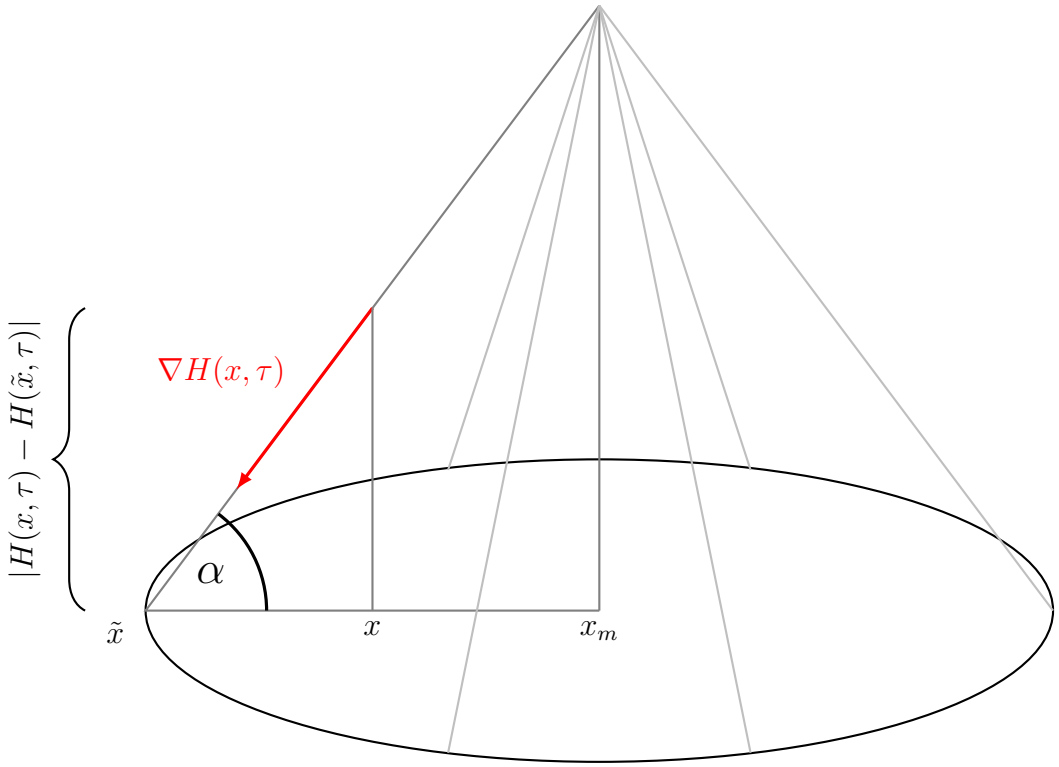

Fig. 7.1: Calculation of α in the x–z plane from the gradient $\nabla H(x,\tau)$ at the point (x,τ) from the tangent of α.

7.2 PDE–Slope Limiter Model

From the conservation of mass a mathematical model for the slope failure process is deduced from first principles. This model is deduced generally and does not depend on a fluid flow which transports the sediment masses.
Starting with a given initial surface height function

$$H_{init}(x) : P \longrightarrow \mathbb{R} \tag{7.4}$$

which does not necessarily obey the critical angle condition

$$\alpha(x) \leq \alpha_c \quad \forall x \in P. \tag{7.5}$$

For every point $x \in P$ the angle α is given by equation (7.3). Therefore,

$$\mathbb{S} := \{x \in P \,|\, \alpha_c < \alpha\} \tag{7.6}$$

is defined as the set which comprises all points $x \in P$ violating the critical angle condition (7.5) and thus

$$\alpha_c \leq \arctan\left(\|\nabla H_{init}(x)\|_2\right) \quad \forall x \in \mathbb{S}. \tag{7.7}$$

With an artificial time τ a temporal evolution of the surface can be regarded as follows. The function

$$H(x, \tau) : P \times [0, T] \longrightarrow \mathbb{R} \tag{7.8}$$

describes the surface height at an artificial time τ. For $\tau = 0$ the initial surface height is used as $H(x, 0) = H_{init}(x)$. Given an underlying plane the height H is a conserved quantity and therefore the continuity equation

$$\frac{\partial H}{\partial \tau} + \nabla \cdot F = 0 \tag{7.9}$$

has to be fulfilled in every control volume P_i with $\bigcup_i P_i = P$. Here, F denotes the total flux into the control volumes P_i. And the total flux F is defined as

$$F := -c\nabla H + \mathbf{v}H \tag{7.10}$$

where c is the diffusive coefficient and $\mathbf{v}$ denotes an advective velocity. In the setting

that the sediment surface only evolves due to gravitational processes following the slope, there is no advection which acts on the surface. Therefore, $\mathbf{v} = 0$ and with equation (7.10) equation (7.9) transforms into a diffusion equation with variable coefficient and reads as

$$\frac{\partial H}{\partial \tau} - \nabla \cdot (c \nabla H) = 0. \tag{7.11}$$

This model describes the general temporal evolution of the height $H(x, \tau)$. By definition the conservation of mass is ensured at every time τ. In the following the diffusive coefficient c is modified to incorporate the angle of repose α_c into this model. Furthermore, the slope angle α is incorporated into c by setting

$$c\left(\nabla H(x,\tau)\right) := \begin{cases} 1 & 0 \leq \alpha_c - \alpha \\ 0 & \alpha_c - \alpha \leq 0 \end{cases} \quad \text{with } \alpha = \arctan(\|\nabla H(x,\tau)\|_2). \tag{7.12}$$

With this choice for c the diffusive coefficient depends on the gradient $\nabla H(x, \tau)$ of the surface which results in a nonlinear model and a discontinuous coefficient. And having reached a steady state at time T the angle α is limited by the angle of repose α_c

$$\alpha(x) \leq \alpha_c \quad \forall x \in P,\, \tau = T. \tag{7.13}$$

For a well posed problem boundary conditions at the boundary of a closed domain Γ_P are required. Thus, there should be no flux across the boundary. Consequently, homogenous Neumann boundary conditions

$$\frac{\partial H}{\partial n}(x) = 0 \quad \forall x \in \Gamma_P \tag{7.14}$$

are imposed at the boundaries of P which ensures that no flux across the border is possible. The full partial differential equation including the boundary conditions in distributional sense reads as

$$\frac{\partial H}{\partial \tau} - \nabla \cdot \left(c\left(\nabla H(x,\tau)\right) \nabla H\right) = 0 \quad \forall x \in \Omega, \tau \in [0, T] \tag{7.15}$$

$$\frac{\partial H}{\partial n}(x, \tau) = 0 \quad \forall x \in \Gamma_\Omega, \tau \in [0, T], \tag{7.16}$$

where $c\left(\nabla H(x,\tau)\right)$ is defined as in equation (7.12). Accordingly a nonlinear diffusive model with discontinuous diffusion coefficients has to be solved. Given an initial value

$H_{init}(x,0)$ with $\mathbb{S} \neq \emptyset$ the steady state solution of the system (7.15) and (7.16) is reached at time $\tau = T$, where T is defined as

$$T := \inf\{\tau \in [0,\infty) : \mathbb{S} = \emptyset\}. \tag{7.17}$$

Having reached $\tau = T$ the diffusive coefficient in (7.15) vanishes and $H(x,\tau)$ has reached a steady state solution and all gradients obey the angle condition (7.5) with $\mathbb{S} = \emptyset$.

7.3 Discretization and Implementation of the hill slope model

In the following the implementation and discretization of the equations (7.15) and (7.16) are described. Here, the hill slope model is discretized with finite differences on a rectangular grid. Within this setting the finite difference approach can also be regarded as a finite volume discretization on rectangular cells.

First, this approximation chooses a linearization which uses the old time step H^n to calculate the gradient on each edge of the cell $(i \pm \frac{1}{2}, j \pm \frac{1}{2})$. With a first order explicit Euler time stepping scheme the discretized equation reads as

$$\frac{H^{n+1} - H^n}{d\tau} - \nabla \cdot \left(c\left(\nabla H^n(x,\tau)\right) \nabla H^n\right) = 0. \tag{7.18}$$

Second, the diffusive term is discretized with a central scheme and the full discretization is

$$\frac{H^{n+1} - H^n}{d\tau} = \left(\frac{F_{i+\frac{1}{2},j} - F_{i-\frac{1}{2},j}}{dx} + \frac{F_{i,j+\frac{1}{2}} - F_{i,j-\frac{1}{2}}}{dy} \right), \tag{7.19}$$

where the fluxes $F_{i\pm\frac{1}{2},j}$ and $F_{i,j\pm\frac{1}{2}}$ are defined as follows

$$F_{i\pm\frac{1}{2},j} = c_{i\pm\frac{1}{2},j} \frac{H_{i\pm\frac{1}{2},j} - H_{i,j}}{x_{i\pm\frac{1}{2}} - x_i} \qquad F_{i,j\pm\frac{1}{2}} = c_{i,j\pm\frac{1}{2}} \frac{H_{i,j\pm\frac{1}{2}} - H_{i,j}}{y_{j\pm\frac{1}{2}} - y_j}. \tag{7.20}$$

Both coefficients are set $c_{i\pm\frac{1}{2},j}$ and $c_{i,j\pm\frac{1}{2}}$ as in (7.12). This slope condition is calculated at each edge of the cell, where an interpolation for the gradient $\nabla H^n_{i\pm\frac{1}{2},j\pm\frac{1}{2}}$ is needed. Therefore, $\nabla H^n_{i\pm\frac{1}{2},j\pm\frac{1}{2}}$ is approximated by linear interpolation from all six adjacent values.

For example, $\nabla H^n_{i+\frac{1}{2},j}$ is approximated by

$$\nabla H^n_{i+\frac{1}{2},j} = \begin{pmatrix} \frac{H_{i+1,j}-H_{i,j}}{dx} \\ \left(\frac{H_{i+1,j+1}+H_{i,j+1}}{2} - \frac{H_{i+1,j-1}+H_{i,j-1}}{2}\right)/(2dx) \end{pmatrix}. \tag{7.21}$$

Note here, that the direct neighbors cancel out during the interpolation and discretization. In addition, an illustration of this interpolation and discretization is presented in Figure (7.2). Furthermore, the jumps in the gradient of the height function $\nabla H(x)$ and the coefficient c are smoothed out by a heaviside function comparable to Equation (2.34). Herewith, continuously differentiable gradients and coefficients are achieved and enter the hillslope model (7.18).

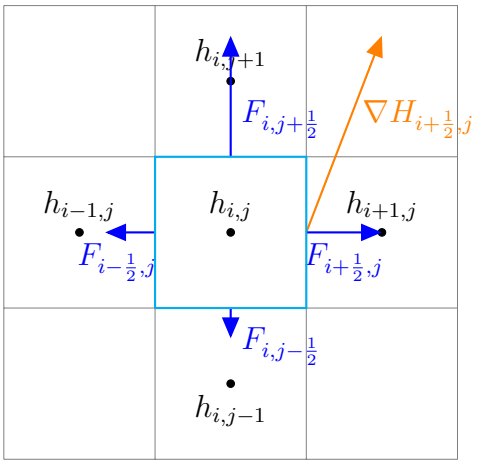

Fig. 7.2: Discretization of the hill slope model on a rectangular grid

7.4 Numerical Tests

In this section a convergence test for the presented slope limiter is designed and the results are discussed. In the following, α_c denotes the angle of repose as stated above in equation (7.5). Beside the slope limiting property, a major requirement on our slope limiter algorithm is the conservation of mass. A test situation constructs a pile of sand which has a conical shape. Therefore, the initial starting configuration is a given volume V_c which is piled up with its center at x_m. This example mimics the rilling of sand from an outlet. A typical example is illustrated in Figure (7.3).

Fig. 7.3: Sand rilling from an outlet. A typical conical pile evolves and forms the critical angle of repose, which could be extracted from this experiment.

(Source: http://i.ytimg.com/vi/SIkRUv39SoI/maxresdefault.jpg)

Given a critical angle $0° < \alpha_c < 90°$ and the volume of the cone V_c, the shape of a conical pile of sand is calculated from basic geometric consideration. The volume V_c of the cone in Figure (7.4) is calulated by

$$V_c = \frac{1}{3} \cdot A \cdot h_c, \tag{7.22}$$

where h_c denotes the height of the cone and A the base area. The base area is calculated by

$$A = \pi \cdot r^2. \tag{7.23}$$

With the critical angle α_c the radius r of the cone is defined as

$$r = \frac{h_c}{\tan(\alpha_c)}. \tag{7.24}$$

Substituting both equations into equation (7.22) yields

$$V_c = \frac{1}{3} \cdot \pi \cdot \frac{h_c^3}{\tan^2(\alpha_c)}. \tag{7.25}$$

Furthermore, the height $h(x)$ is calculated by the intercept theorem (Figure 7.4)

$$h(x) = h_c - \frac{h_c}{r}\|x - x_m\|_2 \tag{7.26}$$

where $x, x_m \in P$ and $h_c, r \in \mathbb{R}$ are lengths.

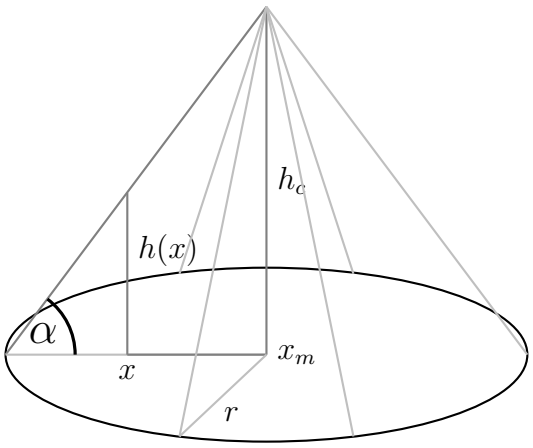

Fig. 7.4: Calculation of a reference solution $h(x)$ by the intercept theorem. $\frac{h_c}{r} = \frac{h(x)}{r - \|x - x_m\|_2}$

With this construction a comparison of the analytical solution to the numerical solution is possible. For example, given a volume V_c and a critical angle for the sand, a computed surface h' can be compared to $h(x)$. For simplicity $h(x)$ is extended to the whole domain by setting $h(x)$ to a reference value h_{ref} outside of the cone as base level. The analytical surface reads as

$$h(x) = \begin{cases} h_c - \frac{h_c}{r}\|x - x_m\|_2 + h_{ref} & \|x - x_m\|_2 \leq r \\ h_{ref} & else \end{cases} \tag{7.27}$$

Without loss of generality this reference height is set as $h_{ref} = 1$. From the Volume V_c the height of the cone h_c can be calculated from equation the (7.22). In the following three different errors are calculated for this problem. First, the error of the tip of cone is calculated by

$$\varepsilon_{h_{tip}} := |h'_c - h_c|, \tag{7.28}$$

where h' denotes the simulated surface. Additionally, the L_1 and L_2 norms are approxi-

mated by

$$\|\cdot\|_1 := \frac{1}{nm}\sum_{i,j}^{n,m} |h'_{i,j} - h(x_i, y_j)| \tag{7.29}$$

and

$$\|\cdot\|_2 := \sqrt{\frac{1}{nm}\sum_{i,j}^{n,m} \left(h'_{i,j} - h(x_i, y_j)\right)^2} \tag{7.30}$$

where $h(x_i, y_j)$ denotes the reference value at

$$(x_i, y_j) := \left((i - \frac{1}{2})dx, (j - \frac{1}{2})dy\right). \tag{7.31}$$

To ensure stability the time step is chosen as $dt = (dx)^3$. Figure (7.6) shows the convergence error and the number of iterations of the algorithm. An symptotic first order for the sediment height is obvious and the number of iterations needed to reach the fix point grows with dx^3. In all computations the error in the mass conservation is below 0.1% and is not of further interest.

In this chapter, a model is developed which limits all angles and conserves the sediment mass. A heat equation is modified such that a non linear model with discontinuous coefficients emerges. In a numerical convergence study a first order convergence for the presented approach is found.

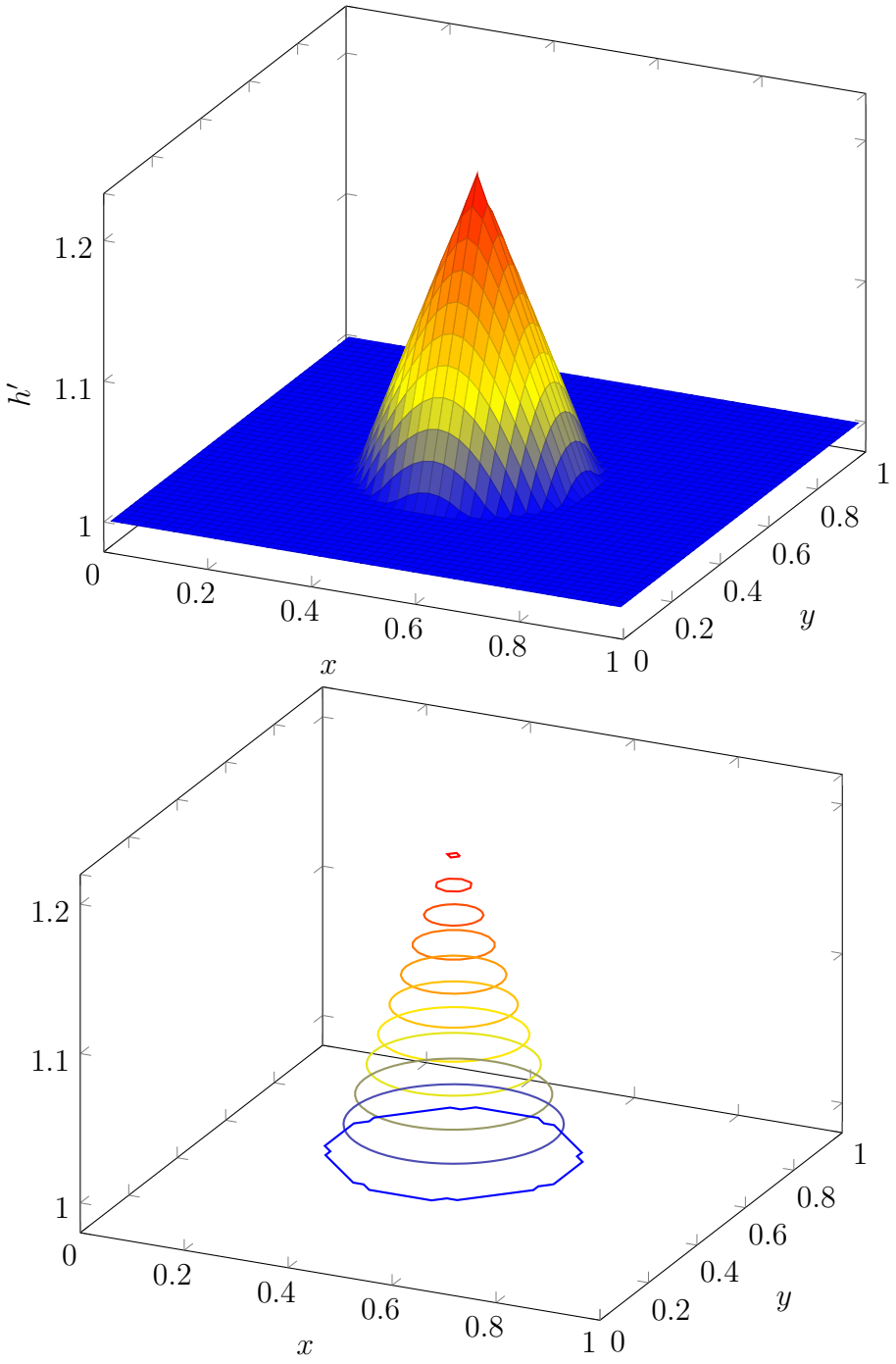

Fig. 7.5: Reference solution of a conical pile of sand with the volume $V_c = 0.01$, $h_{ref} = 1$, and an angle of repose $\alpha_c = 45°$

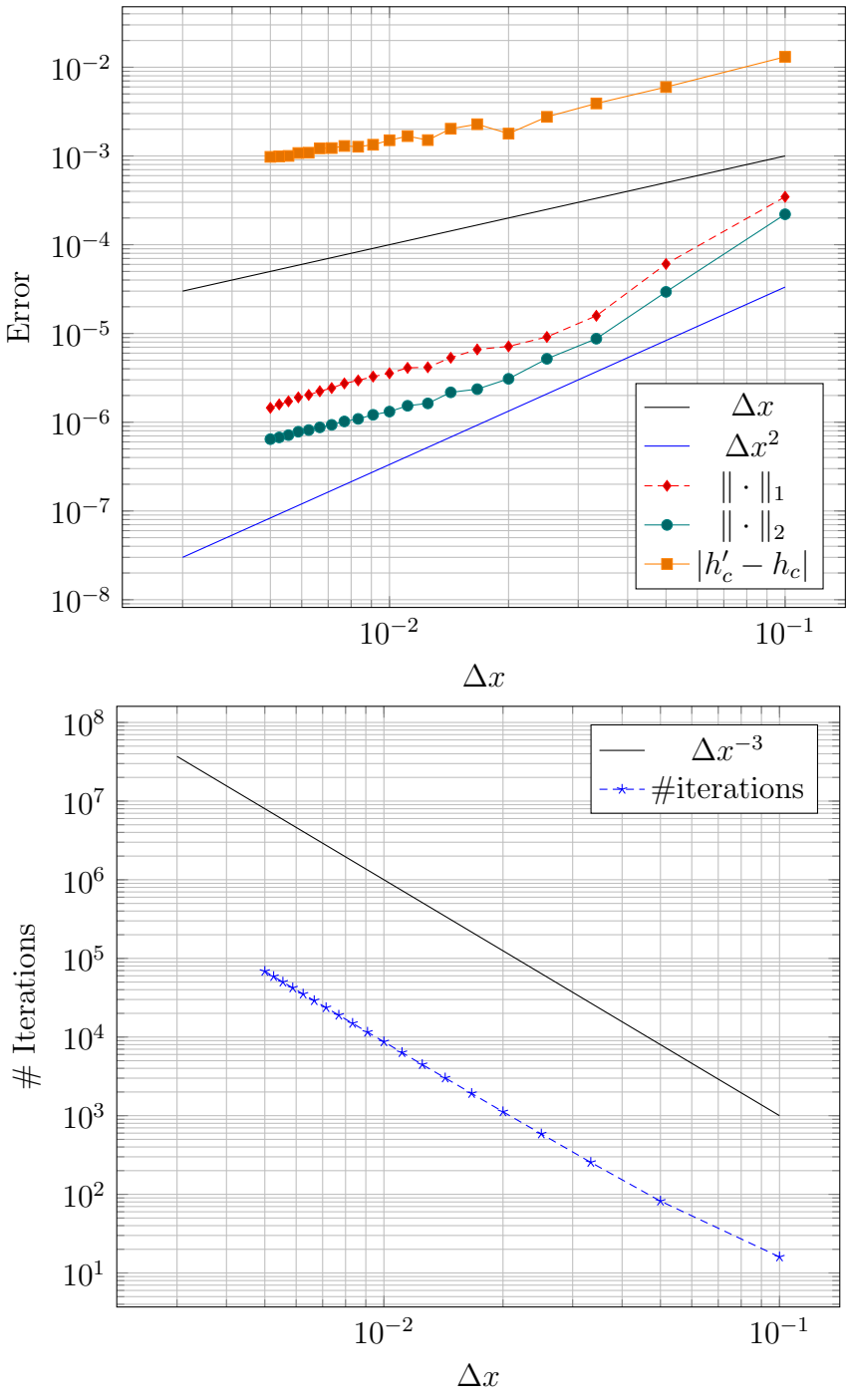

Fig. 7.6: Convergence results of the central difference discretization of (7.19) for $V_c = 0.01$ and $\alpha_c = 45°$. Top: The errors were computed following (7.29) and (7.30). Here, the error of the first order time discretization dominates asymptotically. Bottom: The number of iterations needed to reach a steady state scales linearly with the time step $\Delta t = \Delta x^3$.

8 Coupling to the Navier Stokes equation

After the modelling and the description of the sediment and the fluid models, the bed load, the suspension load, the slope limiter, and the Navier Stokes equations on arbitrary domains should be coupled with the sediment models. First, the coupling of the suspension load with the Navier Stokes equations by a gravitational source term is presented. Here, the suspension load exerts an additional force onto the momentum equation of the Navier Stokes. Second, the temporal evolution of the sediment surface changes the computational domain and has to be taken into account. Altogether, a loosely partitioned coupling technique is chosen, which leads to a robust coupling of the presented models.

8.1 Suspension induced gravitational volume forces on the fluid

The next step is to incorporate the bidirectional coupling of the suspension load and the fluid. Here, a buoyancy term formulation for an additional force is chosen. This additional term results in a new local density

$$\tilde{\rho} := \rho_f + c \tag{8.1}$$

where ρ_f represents the fluid density and $c := c(x,t)$ denotes the suspension load concentration. By multiplying the gravity force terms g in the Navier Stokes equations with $\tilde{\rho}/\rho_f$ a Boussinesq approximation for a buoyancy term

$$\tilde{g} = \frac{\tilde{\rho}}{\rho_f} g. \tag{8.2}$$

is incorporated into the Navier Stokes momentum equation. This approximation was previously introduced by Boussinesq (1903) for temperature driven currents which resulted from density differences due to temperature differences. The Boussinesq approximation assumes only small differences between the density $\tilde{\rho}$ and the original density ρ_f. Thus, the idea here is that only the gravity term in the system is influenced by the change of the density. In all other terms of the momentum equation and the continuity equation the fluid density ρ_f is assumed to be constant. This assumption justifies the retention of the continuity equation $\nabla \cdot u = 0$ for an incompressible fluid. The usage of this approach and its application to gravity currents was widely investigated over the last century, compare Spiegel & Veronis (1960), Benjamin (1968), Mahr (1986), Bonnecaze et al. (1993), D'Alessio et al. (1996), and Shin et al. (2004). A typical suspension load concentration is in the range of $10^{-4} - 10^{-1} kg/m^3$ (Rolinski, 1999). Therefore, the assumption of small density differences is valid and justifies the use of the Boussinesq approximation for density changes. In the following, the approximation for gravity currents presented in Moodie (2002) is used. The experimental analysis of the coupling is presented in Figure (8.1). Here, a spherical volume of suspended material is placed in a closed cubical domain without any velocity inducing conditions, like inflow or outflow boundary conditions. The suspended material spreads due to the self induced velocities in the domain and settles down. After the settling of the material at the bottom all velocities decrease.

8.2 Temporal evolution of the sediment–fluid domain

The sediment surface Ω_s changes over time. These changes result from the forces exerted by the fluid on the sediment surface which results in a transport capacity. With this transport the sediment masses are redistributed and therefore the sediment surface $\Omega_s(t)$ is time dependent. The full system consisting of the Navier Stokes equations (2.17) and the sediment models (6.3) and (6.10) including their boundary conditions reads as

$$\rho(\partial_t u + (u \cdot \nabla)u) = \nabla \cdot (\mu S) - \nabla p - \sigma \kappa n + \rho \tilde{g} \qquad \forall (x,t) \in \Omega_f \times [0,T) \tag{8.3}$$

$$S = \nabla u + (\nabla u)^T \tag{8.4}$$

$$\nabla \cdot u = 0 \tag{8.5}$$

$$\frac{\partial c}{\partial t} + u \cdot \nabla c + w_g \frac{\partial c}{\partial y} = K \Delta c \qquad \forall (x,t) \in \Omega_f \times [0,T) \tag{8.6}$$

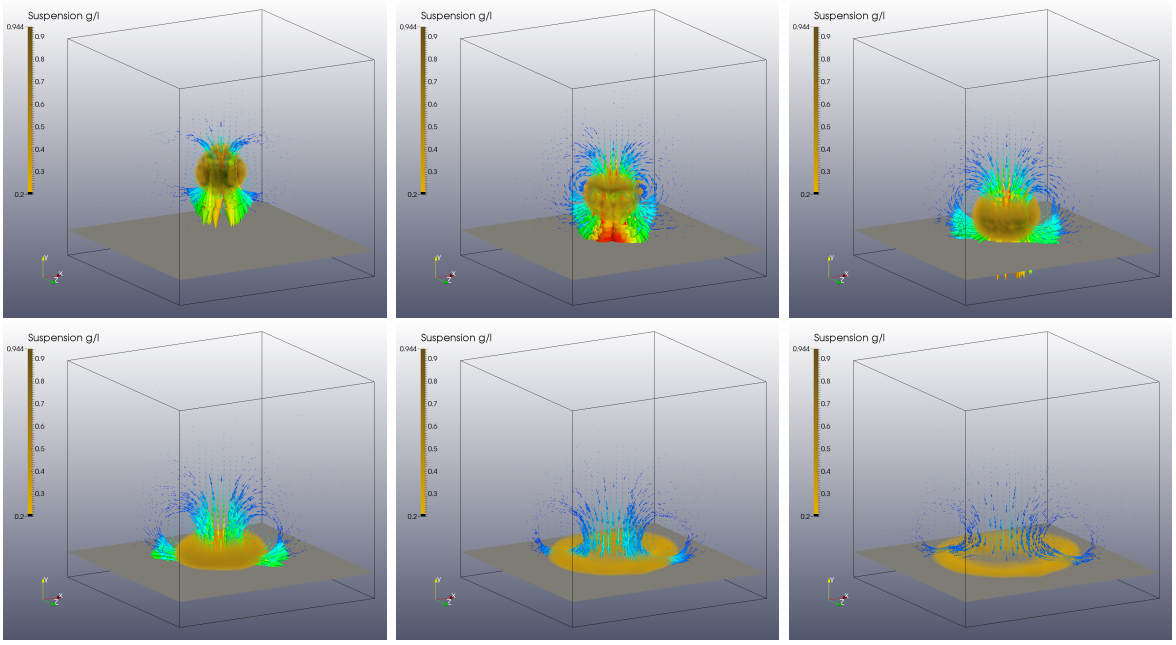

Fig. 8.1: Settling of the suspension load starting from a spherical volume of fine grained particles. The coupling of the suspension load model with the momentum equation of the Navier Stokes equations induces the velocities. After the settling of the material the velocities decrease and fade out.

$$\frac{\partial h}{\partial t} = -\nabla \cdot q_s(\tau(u)) + Q_b - S_b \qquad \forall (x,t) \in P \times [0,T) \tag{8.7}$$

$$u|_{\Gamma_D} = u_D, \quad \left.\frac{\partial u}{\partial n}\right|_{\Gamma_N} = g_n, \quad \left.\frac{\partial u}{\partial \tau}\right|_{\Gamma_N} = g_\tau \tag{8.8}$$

$$\frac{\partial c}{\partial n} = 0 \qquad x \in \Gamma_{\Omega_f} \tag{8.9}$$

$$c = c_{ref} + \frac{S_b}{|v_n|} - Q_b \qquad x \in \Omega_s \tag{8.10}$$

$$\frac{\partial h}{\partial n} = 0 \qquad x \in \Gamma_P. \tag{8.11}$$

In this notation the spatial and temporal dependence of the variables u, p, h, and c are omitted. All other parameters, for instance ρ and μ, are also presented without x and t in the notation. Additionally, the distinction between the tangential component τ in the boundary condition and the shear stress $\tau(u)$ in the sediment model is obvious and needs no further explanation. In detail, the used domains are denoted by $\Omega_f = \Omega_l \cup \Omega_g \cup \Gamma_f$ for the fluid phases, liquid and gas, Ω_s denotes the sediment surface, and

the plane P is described for the sediment bed level equation (8.7). To solve the coupled system (8.3 - 8.11) different approaches in literature are described, compare Felippa & Geers (1988), Farhat et al. (1995), Felippa et al. (2001), Matthies & Steindorf (2003), Borazjani et al. (2008), and Brenk et al. (2008). For time dependent fluid domains the typical approaches are partitioned coupling algorithms (Felippa & Geers (1988), Brenk et al. (2008), Borazjani et al. (2008), Yang et al. (2008), Yang & Stern (2009), and Khosronejad et al. (2011)). There are two types of partitioned algorithms the loose or explicit partitioned algorithm and the strong or implicit partitioned algorithm. In detail, the fluid model as well as the sediment models are spatially and temporally dependent.

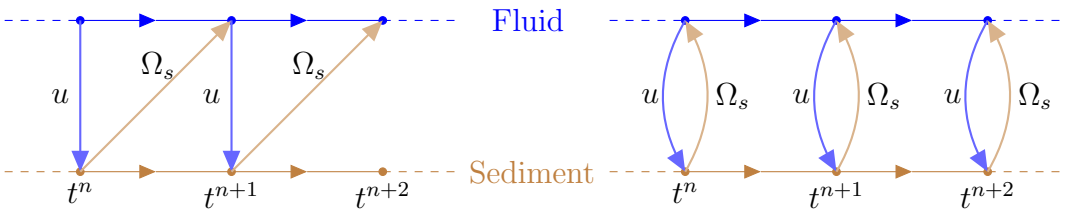

Fig. 8.2: A schematic view of the partitioned coupling algorithms modified after Brenk et al. (2008) and Wall et al. (2007). Left: In the loose or explicit coupled algorithm each solver is used successively after each other. Here, the Navier Stokes solver calculates the flow variables $(u, p)_{t^n}$ on the domain $\Omega_f(t^n)$. With the velocity u the sediment model is solved, which results in a new fluid domain $\Omega_f(t^{n+1})$ for the Navier Stokes solver in the next step t^{n+1}.
Right: The strong coupled approach solves simultaneously both models at the time step t^n. Therefore, a sub iterative method is needed, which iterates during a time step until the convergence for all variables and the fluid domain $\Omega_f(t^n)$ is reached.

For both equations the numerical solutions are given on the domains Ω_f and P which influence each other. The Navier Stokes equations are solved on Ω_f for one single time step t^{n+1} and after this the data from the solution $(u, p)_{t^{n+1}}$ is used as input parameter for the sediment models for the same time step. With the solution of the sediment model $(h, c)_{t^{n+1}}$ the new sediment surface Ω_s and the Boussinesq term $\tilde{g}$ in the Navier Stokes equations can be computed. Here, a stepwise coupling is called loose or explicit partitioned coupling algorithm. In contrast to that a strong or implicit approach solves the full system with an iterative scheme (Matthies & Steindorf (2003), Wall et al. (2007),Vierendeels et al. (2008), Degroote et al. (2009)). On the one hand the loosely coupled approach tends to produce instabilities (Degroote et al., 2008), but the approach

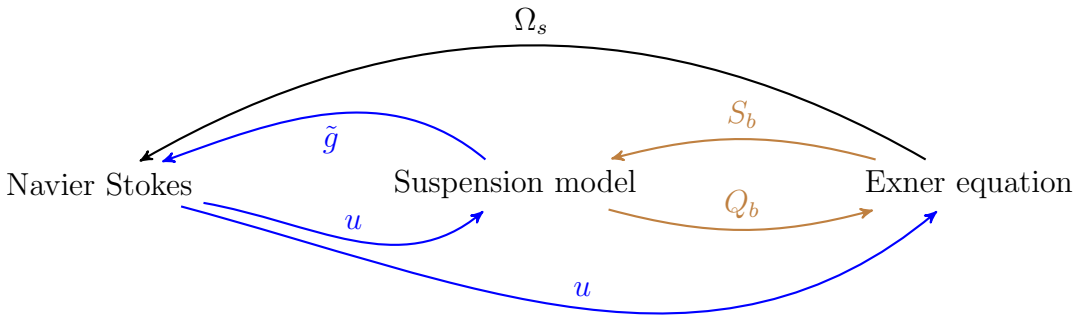

Fig. 8.3: Flow chart of the loosely partitioned coupling algorithm in each time step, the velocities from NaSt3D are used to calculate the new sediment height h which determines the new Ω_f and therefore the new fluid domain.

is easily applicable to existing black box solver. On the other hand strongly coupled algorithms are stable (Degroote et al., 2008) but need a fully integrated iterative algorithm which solves the Navier Stokes equations and the sediment models simultaneously. Figure (8.2) summarizes the basic ideas and differences between the strong and loose coupled approaches. In a schematic view in Figure (8.3) the applied loose coupling of the Navier Stokes solver with the sediment model in each time step is described. Here, the velocities calculated by the Navier Stokes solver are used in both sediment models. In these models the new sediment height is computed. At this point the coupling is realized by the boundary conditions as described before. When the new sediment height h is computed, the new sediment surface Ω_s is generated and mapped back to the fluid domain. The Navier Stokes equations are solved on this updated fluid domain $\Omega_f(t^{n+1})$. During the next time step the buoyancy term $\tilde{g}$ of the Boussinesq approximation is modelled by the density differences caused by the suspension load model of the time step t^n. Therefore, the coupling between the Navier Stokes solver and the suspension load model is realized with the loose approach. For the coupling between the sediment models the loose approach is also chosen. The suspension model calculates the source term Q_b for Exner's bed level equation and its sink term S_b in step t^n. Both terms are used in the boundary conditions during t^{n+1}.

In summary, the full temporal loose coupling of the fluid solver with the sediment models is presented in Figure (8.4). The time step restriction dt_c for the fully coupled system is

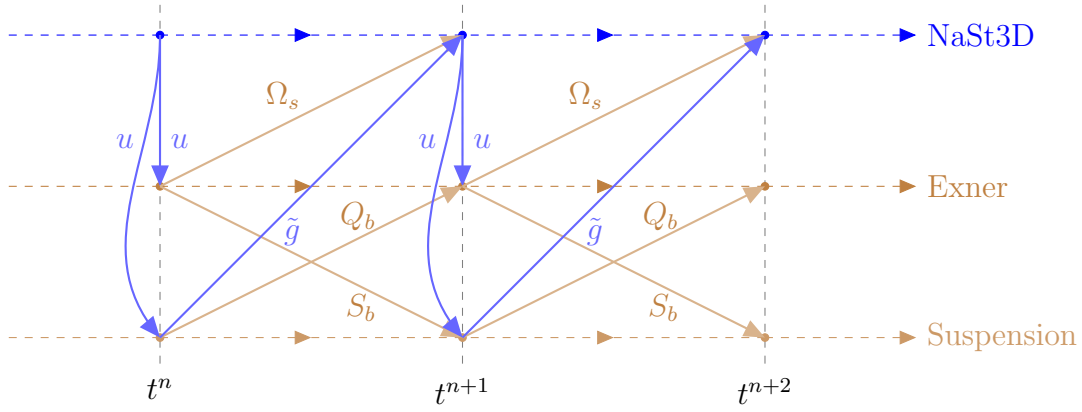

Fig. 8.4: Full temporal loose coupling of the Navier Stokes solver with both sediment models. At first the computed velocities from the fluid solver are used in the Exner equation and in the suspension model. Both models are solved simultaneously. The newly generated sediment surface Ω_s is mapped on fluid domain Ω_f for the time step t^{n+1}. The buoyancy term for the Navier Stokes equations in the step t^{n+1} is computed by the suspension load model as well. The sediment models are also coupled explicitly with each other, where the source term Q_b and the sink term S_b are calculated for the next step t^{n+1}.

calculated by

$$dt_c = \min\left(dt_{NaSt3D}, dt_{Exner}, dt_{Susp}\right) \tag{8.12}$$

where each time step denotes the time step restrictions from the involved discretized systems. In practice, the Navier Stokes time step dt_{NaSt3D} dominates the others, and is therefore sufficient for the sediment models.

8.3 Mapping and reconstruction of the new fluid domain

For the correct coupling of the sediment model and the fluid model a correct and efficient remapping of the new fluid domain Ω_f is necessary. Here, the new sediment domain Ω_s is written as three dimensional points $x \in \mathbb{R}^3$. With this information a new level set function ϕ_g for the geometry is computed, which has a zero level set contour $X_g = \{x \in \Omega \,|\, (x_1, x_3) \in P \text{ and } x_2 = h(x_1, x_3)\}$ containing the points on the sediment surface. The first approach is to calculate the minimal euclidean distance from each point $x \in \Omega$ to the set X_g

$$\phi_g(x) = \min_{x_g \in X_g} \|x - x_g\|_2. \tag{8.13}$$

With this choice a full distance relation for every point x to all points on the surface x_g is calculated in each step. During the parallelisation this procedure would require a full communication of all points x_g for each x. To reduce this enormous computational costs in this approach the reinitialisation scheme for the Hamilton-Jacobi equation (2.31) is reused. Here, the reinitialisation iterates over an initial guess ϕ_g^0 and reconstructs ϕ_g including its distance properties. Thus, the reinitialisation process does not change the zero level set contour of the initial guess of the correct distance function beside numerical errors. The major aim for an initial guess for ϕ_g is to achieve an adequate approximation of this contour. The distance properties and the computation of the normals are corrected by the iterative reinitialisation afterwards. For the initial guess a local approximation of the distance to the surface h is computed by

$$\phi_g^0(x) = \min_{x_g \in \Omega_{dx}^l(x)} \|x - x_g\|_2 \qquad x \in \Omega \tag{8.14}$$

where the minimum is computed in the local neighborhood of $(x_1, h(x_1, x_3), x_3)$

$$\Omega_{dx}^l(x_g) = \{x' \in X_g \,|\, \|\Pi(x') - \Pi(x_g)\|_\infty \leq l dx\}\,. \tag{8.15}$$

Here, $\Pi : \mathbb{R}^3 \mapsto \mathbb{R}^2$ denotes the projection of x to the underlying plane P by $\Pi(x) := (x_1, x_3) = x_p$ and l denotes the amount of cells in the neighborhood used to calculate $\phi_g^0(x)$. Throughout this work the neighborhood relation is set to $l = 1$. If l is chosen large enough, the approximation tends to the full approach from (8.13). Finally, the sign of the level set function $\phi_g(x)^0$ is determined by

$$sgn(\phi_g^0(x)) = \begin{cases} 1 & h(x_1, x_3) \leq x_2 \\ -1 & \text{else} \end{cases} \tag{8.16}$$

With this new approach an initial approximation of the distance function and a sufficient estimate of the zero level set contour are constructed and can be used for the reinitialisation. This reinitialisation corrects the errors near the zero contour during the first iteration steps. Therefore, the level set function near the zero contour is well approached after a few iterations. Note that, due to the choice of the mapping the representation of an „overlapping“ level domains is not viable. Nevertheless, the slope limiting algorithm should preserve such unphysical phenomena concerning sediments.

Table 8.1: Computational parameters and setting for the numerical convergence study in Figure (8.5).

NaSt3D							
Dimensions	Tfin	Re	it_{max}	ε	PoissonSolver	spatial	temporal
$243\,m \times 162\,m \times 162\,m$	1	100	10000	10^{-10}	BiCGStab	VONOS	Adams Bash. 2nd
Exner							
Transp.Formula		f_h	d_{50}	α_c	spatial		temporal
Engelund Hansen		10^{-10}	$0.1\,mm$	$30°$	Central		Adams Bash. 2nd

8.4 Numerical convergence of the fully coupled system

The described coupling of the bed level equation with the Navier Stokes equations is tested by a numerical convergence study. Due to the lack of an analytical solution for the Navier Stokes equations, a solution for the coupled fluid sediment system is also not available. Therefore, an overkill solution for the coupled Navier Stokes equations with the sediment models will be calculated on a very fine grid. The following example for the numerical convergence consists of a rectangular channel with two steps and a half cylindre as obstacles. All obstacles are treated by the level set geometry approach. All fluid and sediment parameters and the full setting including all used grid resolutions are described in Figure (8.5), Table (8.1), and Table (8.2).

Note, all parameters are purely artificial and are only chosen for the purpose to create an example suitable for a numerical convergence study and not to reproduce a physically correct and realistic experiment. The simulation ends after $1\,s$, and the sediment surface on each resolution is interpolated to the finest grid. After the interpolation the error is computed in the regarded rectangular domain demonstrated in Figure (8.5).

With thisrestriction to the red rectangle the extrapolation error in areas next to the obstacle is avoided. For the sediment surface h the error is approximated by

$$\|\cdot\|_1 := \frac{1}{i_m k_m} \sum_{i,k}^{i_m k_m} |h_{ik} - h_{ref\,ik}|, \tag{8.17}$$

where h_{ik} denotes the computed solution on the coarser grid which is interpolated to the fine grid of the overkill solution h_{ref} by the Matlab function interp2().

Here, the relative error

$$\varepsilon_1 := \frac{\|h - h_{ref}\|_1}{\|h_{ref}\|_1}. \tag{8.18}$$

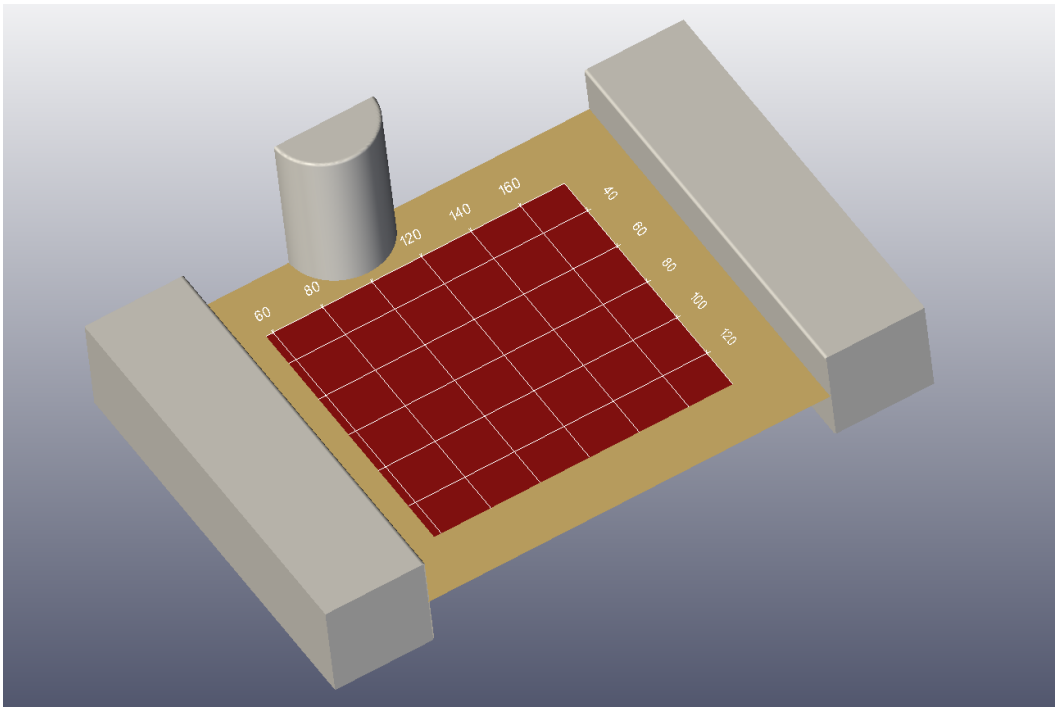

Fig. 8.5: The starting configuration for the numerical convergence study. The rectangular domain in the middle of the sediment surface is used to calculate the errors. This setting is simulated in all grid resolutions given in Table (8.2). Here, the obstacles and the sediment surface are discretized by the level set approach.

is considered.

For the finest grid resolution the simulation is carried out on a $300 \times 200 \times 200$ grid with $dx = 0.81$. The L_1 error follows an overall order of 1.4165. On the coarser grids the error rather follows a first order which is substantiated by a regression on the first four grids with a regression coefficient for the order of 0.9605. However, a second order is observed on the finer grids. Here, the regression analysis on the eight finest grids leads to 2.0139. This convergence rate is a substantial improvement of the algorithm in comparison to a geometry handling by the flag field approach. In Burkow & Griebel (2016) the geometries and the sediment surface are treated by the flag field approach, and an experiment similar to the setting presented in Figure (8.5) yielded an overall order of 0.818.

Table 8.2: Computational grid resolutions and corresponding spatial grid sizes for the numerical convergence study in Figure (8.5).

Grids					
Gridpoints	$30 \times 20 \times 20$	$48 \times 32 \times 32$	$60 \times 40 \times 40$	$72 \times 48 \times 48$	$90 \times 60 \times 60$
dx	8.1	5.0625	4.05	3.375	2.7
Gridpoints	$108 \times 72 \times 72$	$120 \times 80 \times 80$	$135 \times 90 \times 90$	$150 \times 100 \times 100$	$162 \times 108 \times 108$
dx	2.25	2.025	1.8	1.62	1.5
Gridpoints	$180 \times 120 \times 120$	$192 \times 128 \times 128$	$210 \times 140 \times 140$	$240 \times 160 \times 160$	$270 \times 180 \times 180$
dx	1.35	1.2656	1.1571	1.0125	0.9

In summary, the fully coupled algorithm leads to a convergence order between first and second order. Here, the benefits of the new level set geometry handling in comparison with the flag field are obvious. An improvement of almost a full order has been observed in this convergence experiment compared to the handling of the geometry by the flag field technique.

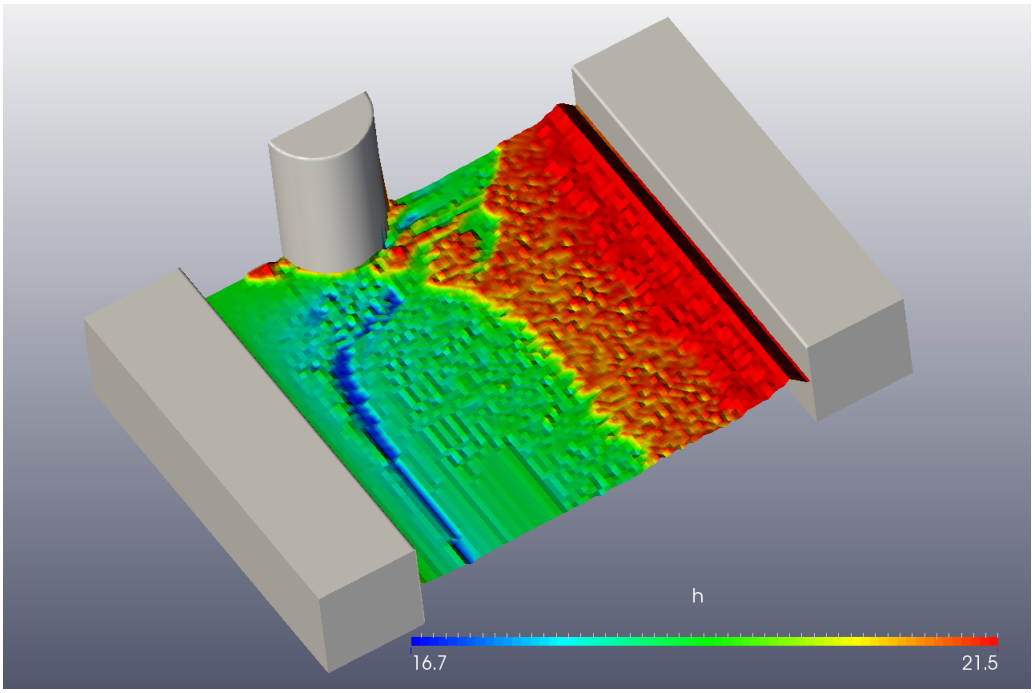

Fig. 8.6: The sediment surface after 1 s on the finest grid. Complex patterns of erosional and depositional site have emerged.

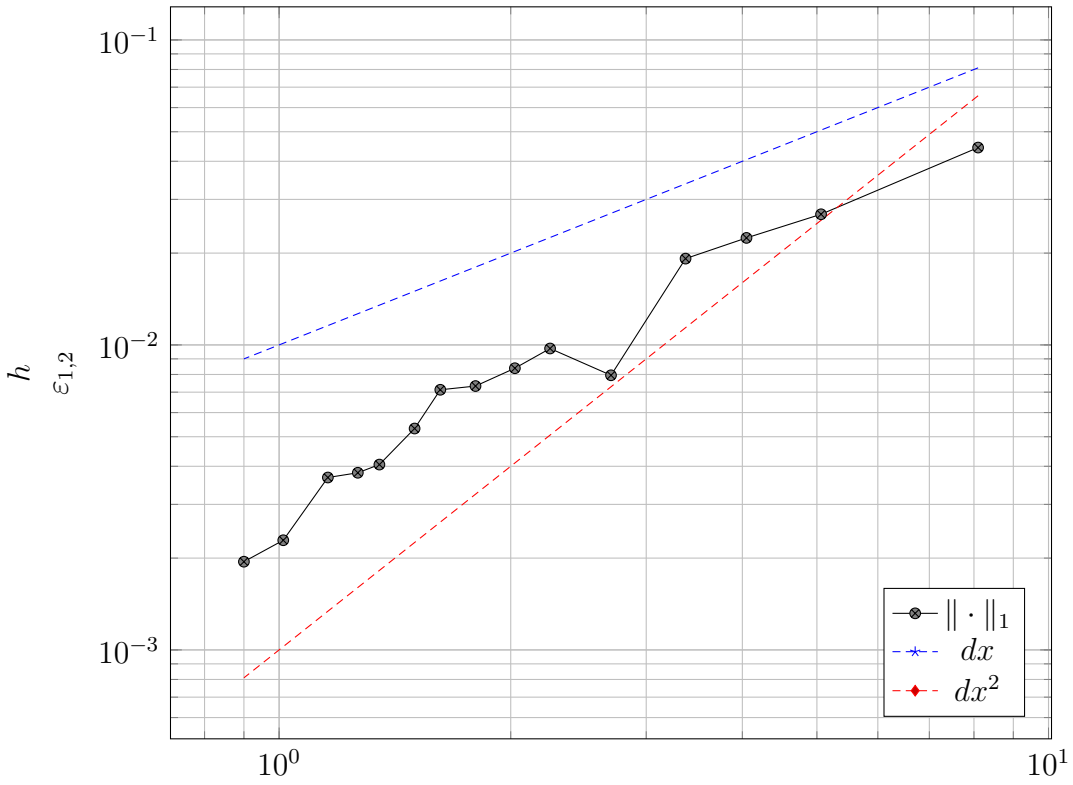

Fig. 8.7: Relative error of the numerical convergence study for the full fluid sediment model. Here, the L_1 norm of the error follows on the coarser grid a first order and on the finer grids a second order convergence.

9 Numerical results for the coupled sediment-fluid model

The numerical examples for the Navier Stokes solver demonstrated the new geometry approach and its applicability to relevant examples. In the following examples the full coupling of the new Navier Stokes solver with the aforementioned sediment model is on focus. The examples are split into two parts. In the first part the full sediment model is used in two single phase flow examples. First, a numerical simulation of a fluvial obstacle mark caused by the bed load transport is depicted. Second, the simulation of a barchanoid dune demonstrates the ability of the full sediment model, where the interaction of the suspension load and the bed load transport drives the temporal evolution of the dune. In the second part the bed load model in combination with a two phase flow is presented and showcases the wide range of field of two phase flows where sediment transport is present. Despite the lack of a turbulence model the numerical simulations all three examples are chosen to adapt phyiscally correct flows.

9.1 Single phase bed load transport example - Fluvial obstacle mark

In the first example the Navier Stokes solver is coupled with the bed level equation. Here, only the single phase flow solver for the complex obstacles treated by the level set approach is applied. The idea is to reproduce two basic features from the field of hydraulic engineering. On the one hand a flow over a backward facing step creates a recirculating vortex, which erodes the sediment bed behind the step. On the other hand the evolution of a fluvial obstacle mark at a cylinder with a hemisphere placed further downstream is simulated. This fluvial obstacle mark consists of an erosional site and a depositional site. At this point the erosion due to the horseshoe vortex system leads to

Table 9.1: Computational parameters and setting for the scour mark simulation presented in Figure (9.1).

NaSt3D							
Dimensions	Tfin	Re	it_{max}	ε	PoissonSolver	spatial	temporal
$4.5\,m \times 0.4\,m \times 1.2\,m$	240.0	10000	5000	10^{-8}	BiCGStab	VONOS	Adams Bash. 2nd
Exner							
Transp.Formula	f_h	d_{50}	α_c	spatial	temporal		
Engelund Hansen	10^{-8}	$1\,mm$	$40°$	Central	Adams Bash. 2nd		

a scour and a deposition site near the obstacle. The formation of this obstacle marks is dominated by the bed load transport. Thus, clear water conditions prevail and the bed load transport is the driving force, the suspension load can be neglected, compare Zanke (2002), Euler & Herget (2012), and Euler & Herget (2011). In the following the obstacle is fully submerged, such that the flow overflows the obstacle in addition to the flow round the obstacle.

9.1.1 Experimental setting

An elongated rectangular channel with $4.5\,m \times 0.4\,m \times 1.2\,m$ is used as the computational domain which is resolved by a $450 \times 40 \times 120$ grid and the computational grid size is $dx = 0.01\,m$. The basic obstacles in this experiment are a rectangular step ($0.2\,m \times 0.2\,m \times 1.2\,m$) at the inflow wall and a cylinder with a hemisphere which is placed further downstream. In detail, the cylindrical obstacle is composed of a cylinder with radius $r = 0.06\,m$ and height $h_{cyl} = 0.2\,m$ and a hemisphere with radius $0.06\,m$ on top of the cylinder. Thereby, the full obstacle has a spherical cap and a full height of $0.26\,m$ and is placed in the middle of the channel. An inflow velocity of $u_{in} = 0.45\,m/s$ is set above the step, and an open end at the outflow wall is imposed by Neumann boundary conditions. At the other four walls Neumann boundary conditions are imposed to model frictionless walls. The step is equipped with no slip boundary conditions. Further, the simulation starts with an initially resting fluid ($u = 0$) and an initially flat sediment surface. A sediment layer of $h = 0.1\,m$ with a particle diameter of $d = 0.001\,m$ is prescribed as sediment starting configuration. Additionally, the transport formula after Engelund & Hansen (1967) is chosen with $f_h = 10^{-8}$. All other numerical and experimental parameters are presented in Table (9.1). The starting configuration of the fluid and the obstacle

geometry in the domain are presented in Figure (9.1).

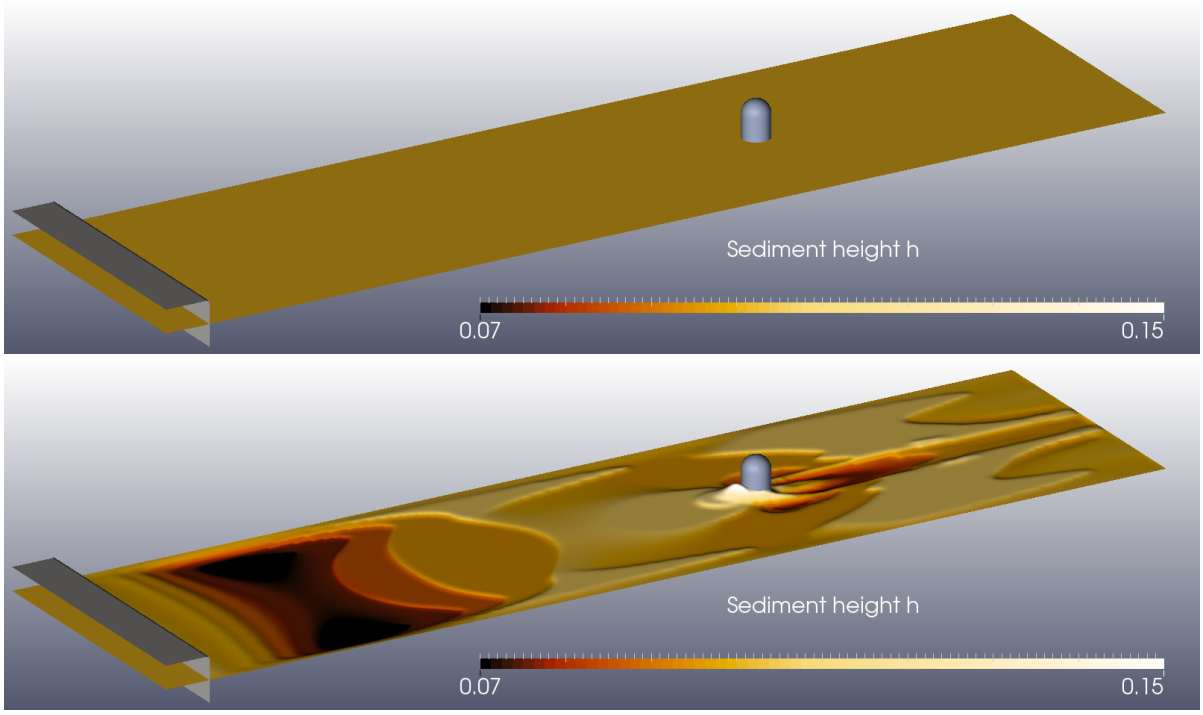

Fig. 9.1: Top: The starting configuration for the single phase flow simulation of the fluvial obstacle mark. The flow direction is from the left to the right. A constant velocity $u = 0.45\,m/s$ is set to the left wall above the step. In the middle of the channel a cylinder with hemisphere is situated, which causes the formation of the scour near the obstacle.
Bottom: Final sediment bed after $240\,s$. A complex scour mark near the cylindrical obstacle has evolved. Additionally, behind the step another erosion site is visible. Here, the recirculating vortex leads to a downward flow, which erodes the sediment over the temporal evolution. Figure (9.4) demonstrates the growth of both erosional features over time.

9.1.2 Evaluation and discussion of the numerical result

Figure (9.4) shows the close up visualisation of the fluvial obstacle mark near the cylinder and the erosion site behind the rectangular step. The four time steps illustrate the sediment surface and the flow fields at the time $t = \{0.5\,s, 25\,s, 100\,s, 200\,s\}$. The three dimensional flow round the cylindrical obstacle evolves at the beginning and causes a continuous transport of the sediment, which leads to lateral depressions and a deposition

in front of the obstacle. These depressions and the depositional ridge build up with the ongoing transport during the simulation. Here, an intense erosional phase at the beginning is followed by a constant amplification of the initially developed bed forms. The deposited material in front of the obstacle originates from the general bed load transport from further upstream. In this region, the transport is caused by the recirculation zone behind the step, which forms a downward flow eroding the sediment surface. This recirculating zone builds up in the first $3\,s$ of the simulation, which are presented in Figure (9.2). Over time the erosion site deepens and forms a three dimensional sedimentary structure in the zone where the downward flow reattaches with the sediment bed. A temporal evolution of the maximum and minimum surface height of the bed forms

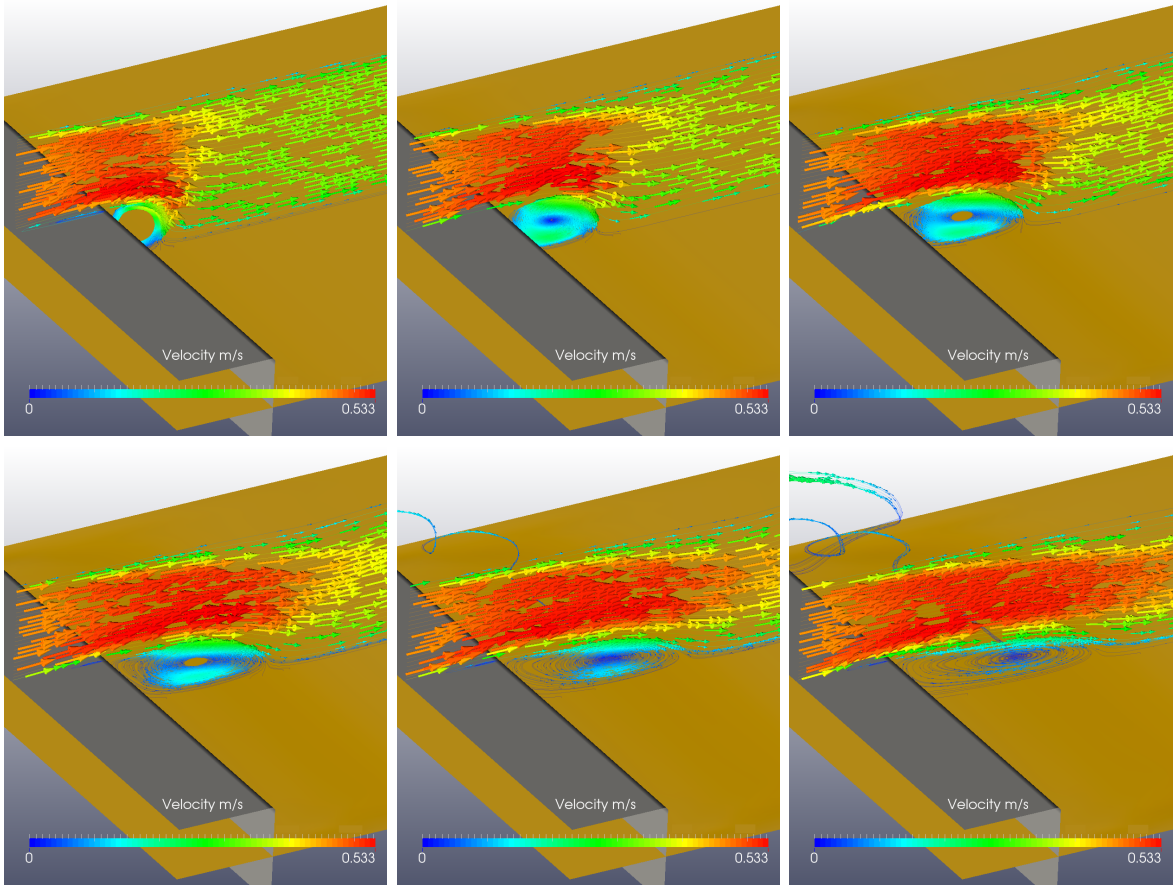

Fig. 9.2: Visualisation of the evolution of the recirculating zone behind the step. On a two dimensional cross section streamlines demonstrate the propagation of the vortex until a steady state is reached after the first $3\,s$.

is given in Figure (9.3). On the one hand a constant erosion of the sediment surface is

identified by the decreasing minimum surface height near the step. On the other hand the maximum height remains constant, which leads to the explanation that the material is transported downstream. This material is moved down the channel, where it accumulates in front of the cylindrical obstacle. This accumulation is visible in the maximum surface height in the second plot in Figure (9.3). Here, the initial build up phase is followed by a decreasing accumulation rate over time. The rest of the transported material entering the lateral scours leads to a constant depth of the depression, visible in the minimum height progress near the obstacle. These observations match qualitatively experimental observations, compare Euler & Herget (2011) and Tafarojnoruz et al. (2012).

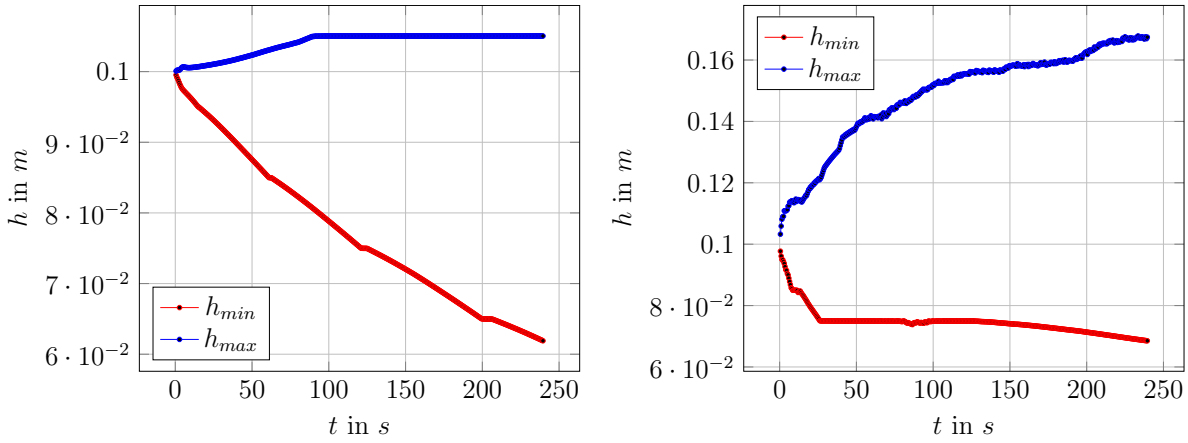

Fig. 9.3: Temporal evolution of the maximum and minimum surface height near the step (left) and the scour (right). For the evolution of the scour depth a qualitative comparison matches the results obtained in Euler & Herget (2011) or Tafarojnoruz et al. (2012).

The basic features of a fluvial obstacle mark and the erosion of the sediment behind the step are well captured by the simulation. A complex system of scours and ridges is recovered by the simulation and the concurrent flow patterns are resolved. Even the temporal evolution of the sedimentary features a qualitative comparison with experiment results. All expected features are well recovered and confirm the applicability of the solver to realistic phenomena in erosional tests.

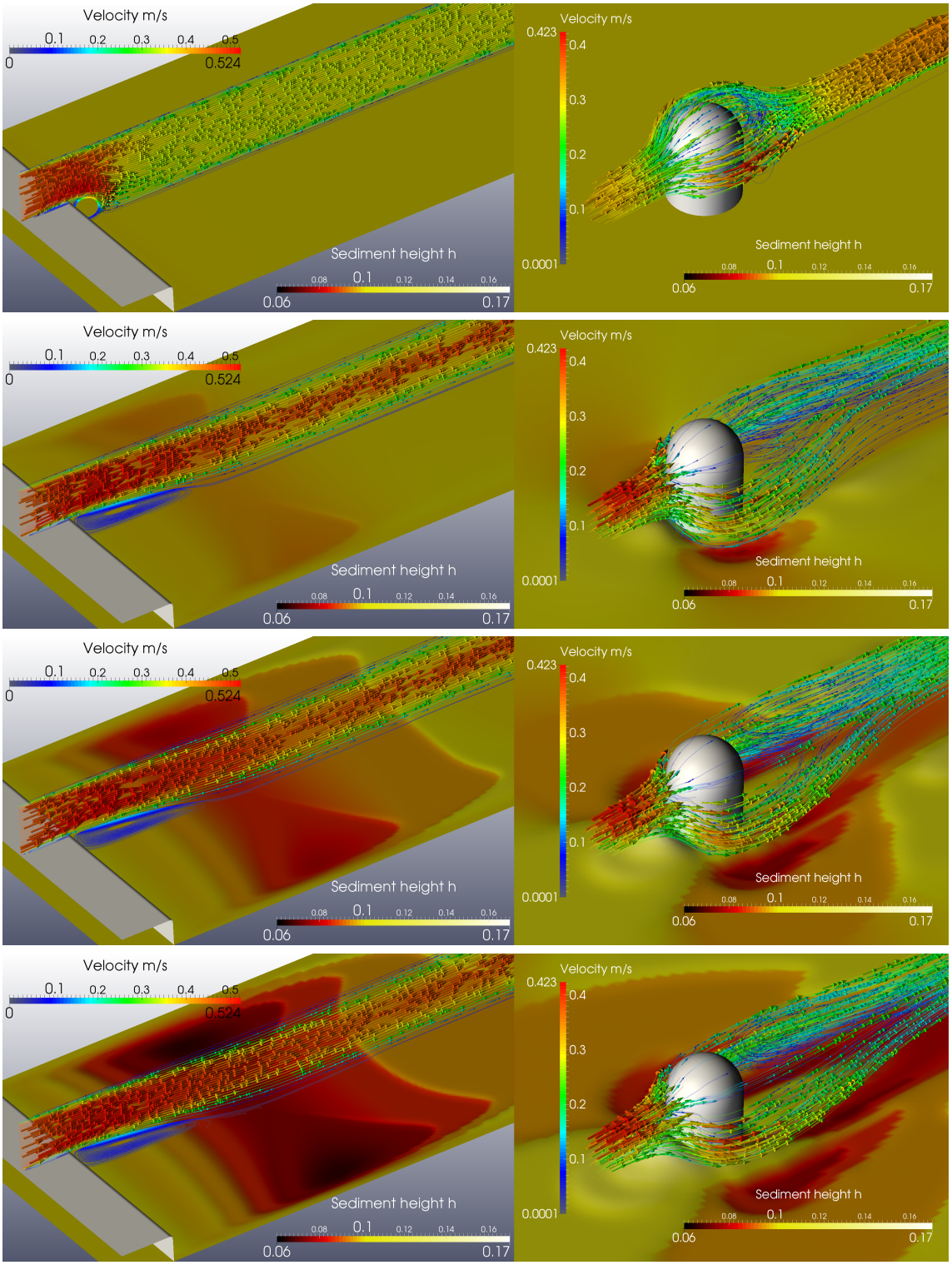

Fig. 9.4: Close up streamline and glyphs visualisation of the temporal evolution of the fluvial obstacle mark, the three dimensional sedimentary structures, and the corresponding flow fields at the time $t = \{0.5\,s, 25\,s, 100\,s, 200\,s\}$.

9.2 Single phase full sediment transport example - Barchanoid dune

In the second example the full sediment model including the suspension load model is applied in a numerical simulation, whereas in the first example only the bed load transport was regarded. Here, the bed load model and the suspension load model are applied simultaneously to simulate the complex transport processes, which lead to the evolution of a barchanoid dune. For the interchange the mass conserving coupling of both models by sink and source terms is used as explained in Section (6.3).

9.2.1 Experimental setting

The basic setting for this example is to use a channel with $20\,m \times 5\,m \times 10\,m$ and a spatial resolution of $200 \times 50 \times 100$, which results in a spatial grid size of $dx = 0.1\,m$. On the left inflow face a velocity of $u = 5\,m/s$ is set. As in the previous examples a solid step is placed at the inflow to avoid an unintended and uncontrollable sediment movement during the initial phase of the simulation. Likewise in the examples before Neumann boundary conditions at the right wall are used to model an open end. All other walls are modelled as frictionless surfaces by imposing slip boundary conditions. For the starting configuration a sand layer of $1\,m$ for the sediment surface is chosen with an initial elongated conical pile of sand. Here, the pile acts as the base material from which the dune develops. The top of this pile reaches up to $3.35\,m$. Before the start of the simulation the slope limiter algorithm is applied to ensure that the slope angle of the pile is below the critical angle of repose ($\alpha_c = 40°$). At the right face an outflow condition is used to design an open end. The particle size for the bed load transport is $d_{50} = 0.001\,m$ and for the suspension load $d_s = 0.00002\,m$. For the bed load transport the Meyer-Peter & Müller formula is used with $\tau_c = 0.047$. Further, a reference concentration in the suspension load model $c_{ref} = 2.0 \cdot 10^{-5} kg/l$ is chosen. In this large scale example, the diffusion of the suspension load is neglected $K = 0$ and sole transport is regarded. In summary, all used parameters and the whole setting are presented in Table (9.2) and in Figure (9.5).

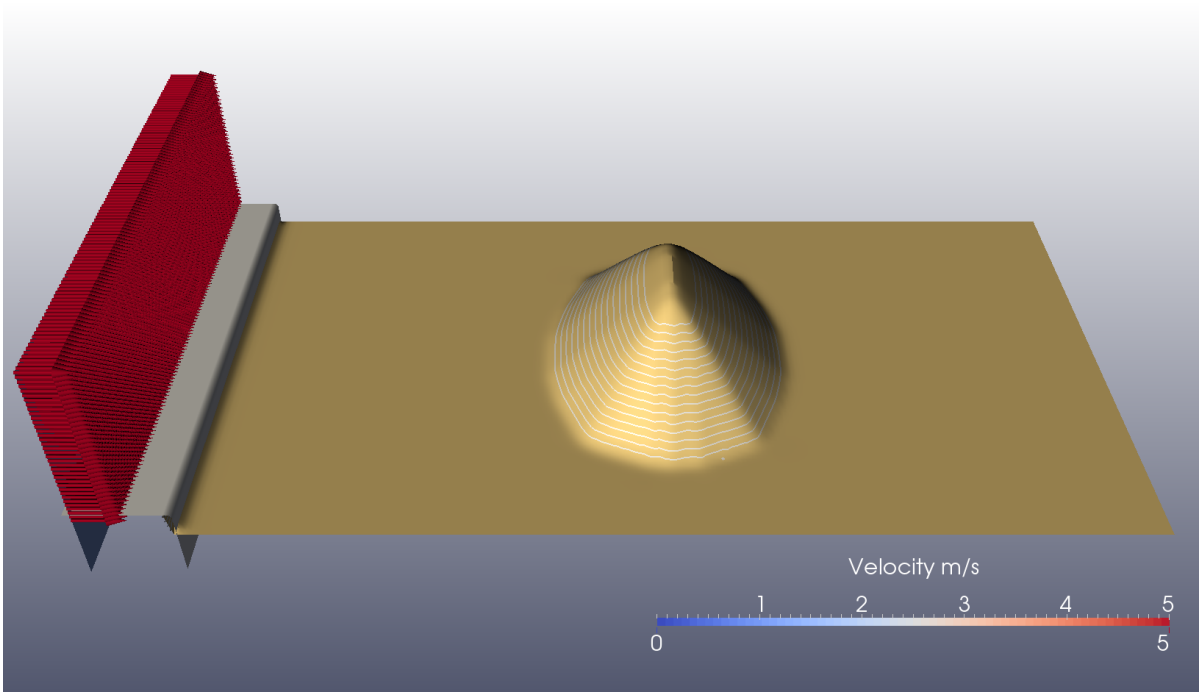

Fig. 9.5: The starting configuration for the single phase flow and the temporal evolution of the barchanoid dune. Flow direction is from the left to the right and a constant velocity $u = 5\,m/s$ is set to the left wall. In the middle of the channel there is an initial elongated sediment pile which is transported over the time and forms the dune in the channel $(20\,m \times 5\,m \times 10\,m)$.

9.2.2 Evaluation and discussion of the numerical result

In Figure (9.6) the typical shape of a barchanoid dune is presented after $250\,s$ of the simulation. The typical morphology of a barchanoid dune is defined as that the whole dune body is crescent shaped and the luv side of the body is sloping upwards, whereas the lee side is dominated by the angle of repose. In detail, the flow transports the particles over the dune body. Reaching the crest of the dune the particles slide down the lee slope and form the specific angle of repose. Additionally, the lateral parts of the dune body, the horns, advance faster than the inner parts, which results in the typical crescent shape with preceding dune horns. Due to the uniform inflow profile in this example a barchanoid dune can evolve. The inverse form of the crescent shaped dune is called a parabolic dune and is characterised by horns travelling slower than the inner parts of the sand body. In general, a parabolic dune usually develops if the velocity and therefore the transport is slower at the sides.

Table 9.2: Computational parameters and setting for the numerical simulation of a barchanoid dune presented in Figure (9.5).

NaSt3D					
Dimensions	Tfin	Re	PoissonSolver	it_{max}	ε
$20.0 \times 5.0 \times 10.0$	250	1000	BiCGStab	1000	10^{-8}
Exner + Suspension					
Transp.Formula	τ_c	d_{50}	d_s	α_c	K
Meyer-Peter-M.	0.047	$1\,mm$	$0.02\,mm$	$40°$	0
NaSt3D		Exner		Suspension	
spatial	temporal	spatial	temporal	spatial	temporal
QUICK	AdamsBash 2nd	Donor Cell	AdamsBash 2nd	Donor Cell	AdamsBash 2nd

The evolution of the dune from the initial pile of sand is demonstrated in Figure (9.7). Here, the transition from a pile with symmetric slopes to a crescent shaped dune with different luv and lee slope angles is obvious. The initial forming of the lateral horns is caused by the uniform velocity profile where there is no friction on the lateral walls. A steady bed transport leads to an asymmetric cross section of the dune body with a slightly increasing luv slope and a lee slope limited by the angle of repose. Additionally, in Figure (9.7) the chronology of the suspension load transport is visualised on a cross section in the middle of the domain which intersects the sediment body. The erosion of the material from the sediment surface and the entrainment into suspension starts at the crest of the dune. At this point the shear stress surpasses the critical value first, and therefore the material is eroded and transported into the fluid body. With the ongoing simulation the interaction of the flow with the sediment surface and the suspended material gets complicated and multi-layered. On the one hand the flow forms the moving sediment surface into the typical shape of a barchanoid dune. On the other hand the erosion from the surface into the suspension load interacts with the flow by the gravitational source term coupled by the Boussinesq approximation. Figure (9.7) compares the suspension load and the velocities on the same cross section at the same time steps. When the velocities are high enough, the suspension load is transported away, but in zones where the velocity and the transport capacity decreases, e.g. in the wake of the dune, the suspension load distributes all over the fluid. Behind the dune a recirculation zone is obviously visible in Figure (9.7). In this recirculation zone the transport capacity is high enough and sufficiently moderate to carry some suspended material with the flow.

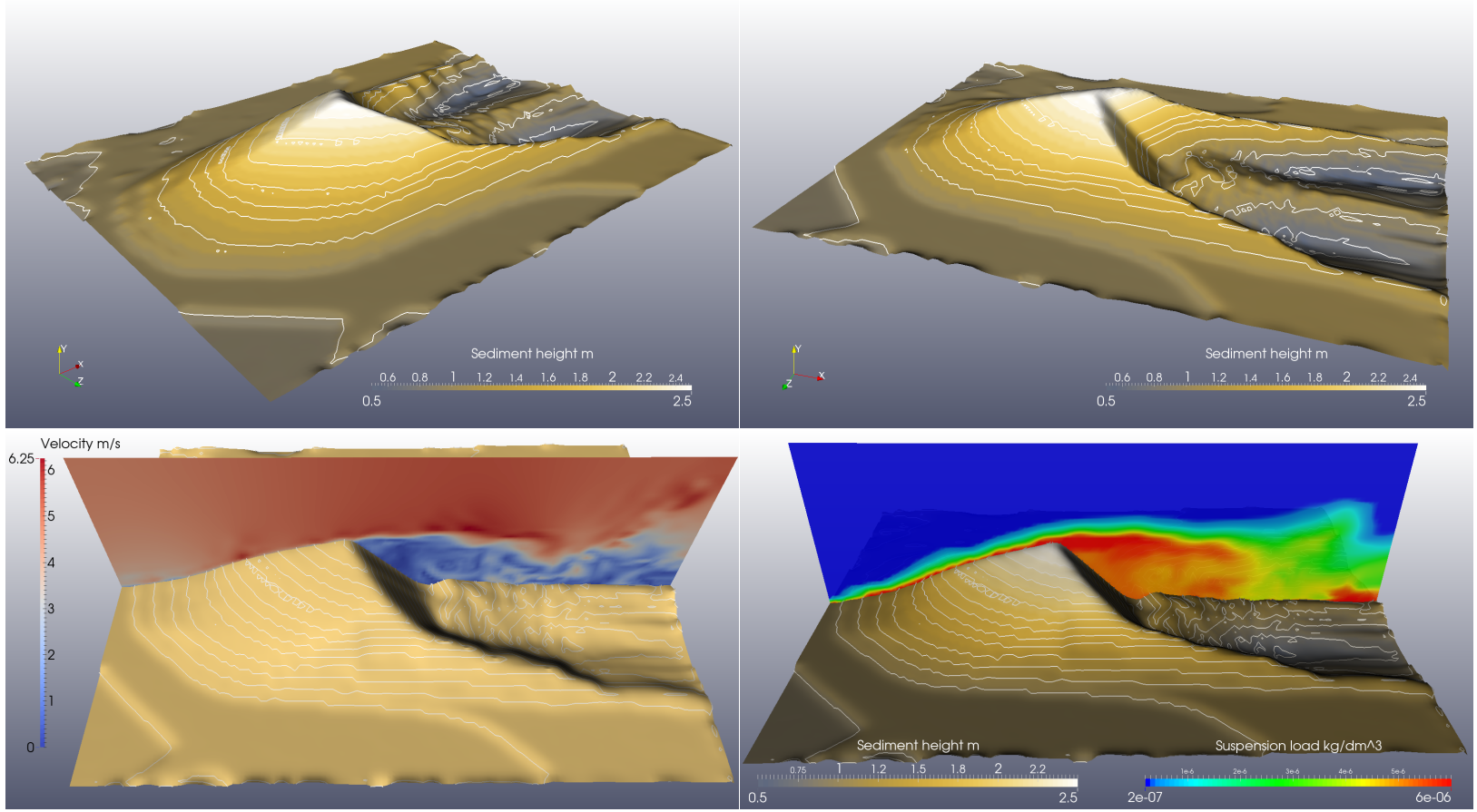

Fig. 9.6: Top: A visualisation of the final sediment surface with height isocontours indicating same height levels. The typical crescent shape is well reproduced. Additionally, the asymmetric cross profile of the dune is also well recovered.
Bottom: Illustration of the velocity field on a cross section through the middle of the domain (left). A visualisation of the suspended material on the same cross section as for the velocities (right). Here, the recirculation zone behind the dune is obvious.

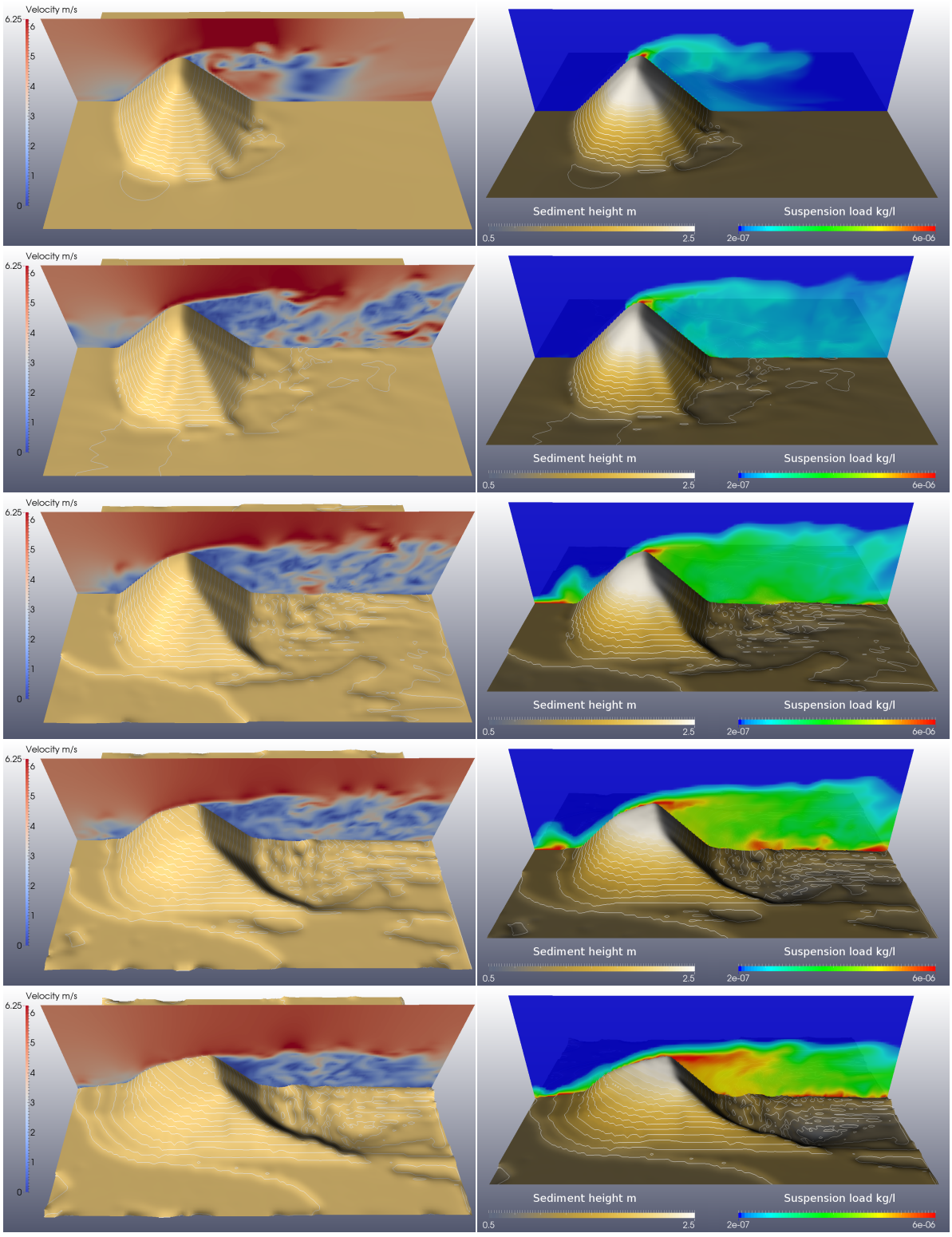

Fig. 9.7: Temporal evolution of the flow field (left) and suspension load (right) at the time steps $t = \{2\,s, 5\,s, 25\,s, 75\,s, 150\,s\}$. The visualisation of the dune surface is enhanced by isocontours for the height in both sequences.

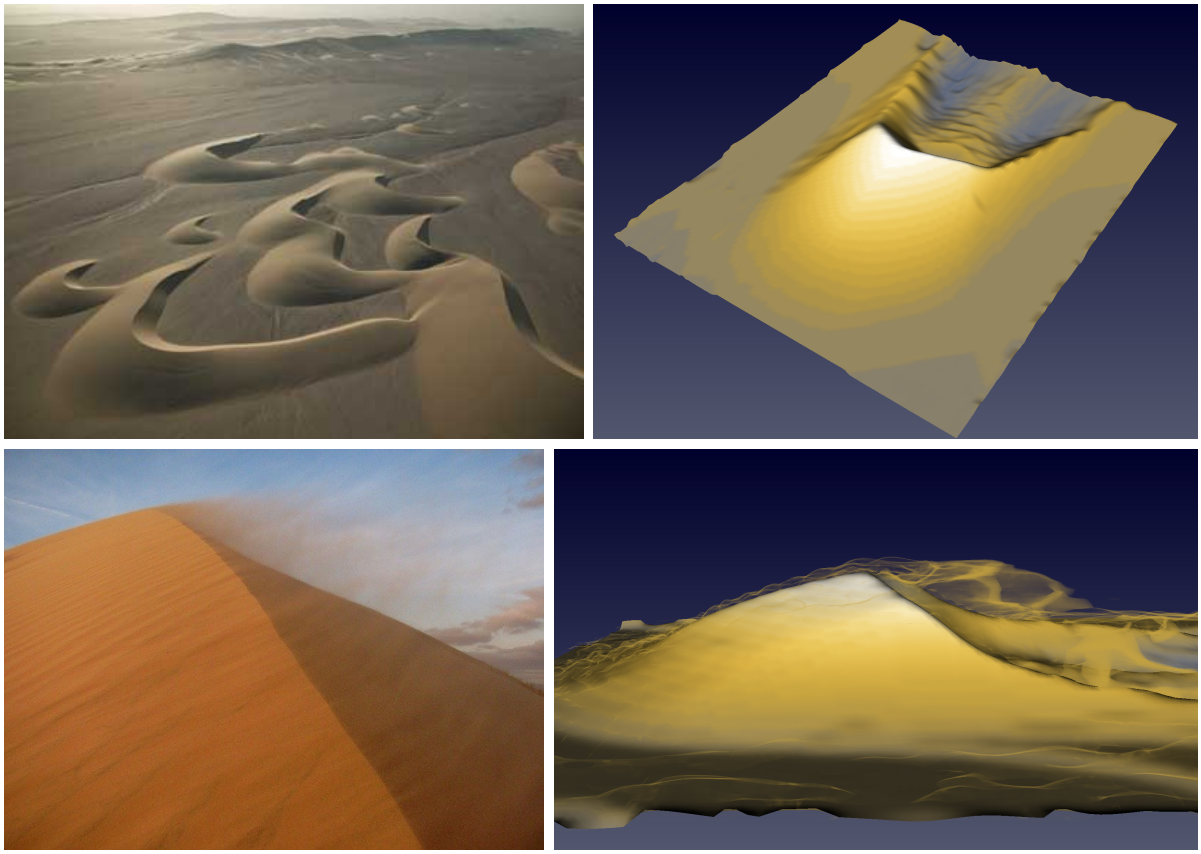

Fig. 9.8: Top: A qualitative comparison between a barchanoid dune from a dune field in Namibia (Flood, undated) (left) and the simulated dune (right). Bottom: Sand blowing off a real (Destefano, 2011) (left) and a simulated (right) dune crest.

Furthermore, Figure (9.7) illustrates the velocities on the cross section cut through the dune. Moreover, the reshaping of the sediment is represented by the visualised height function h. A qualitative comparison with real dunes confirms the realism of the simulated results, compare Figure (9.8) Here, the crescent shape an the trailing horns are well recovered. From the visualised suspension load near the dune it is obvious that the transport processes are in good agreement with the observations from field experiments, compare Sauermann et al. (2000), Sauermann et al. (2001), and Schwämmle & Herrmann (2003). Especially the temporal evolution follows the observation from field experiment, and the comparison of the suspension load blasting from the crest with a field example qualitatively confirms the numerical simulation.

Figure (9.9) presents the temporal evolution of four cross profiles of a classical dune from Groh et al. (2009) and four cross profiles from the numerical simulation. Despite

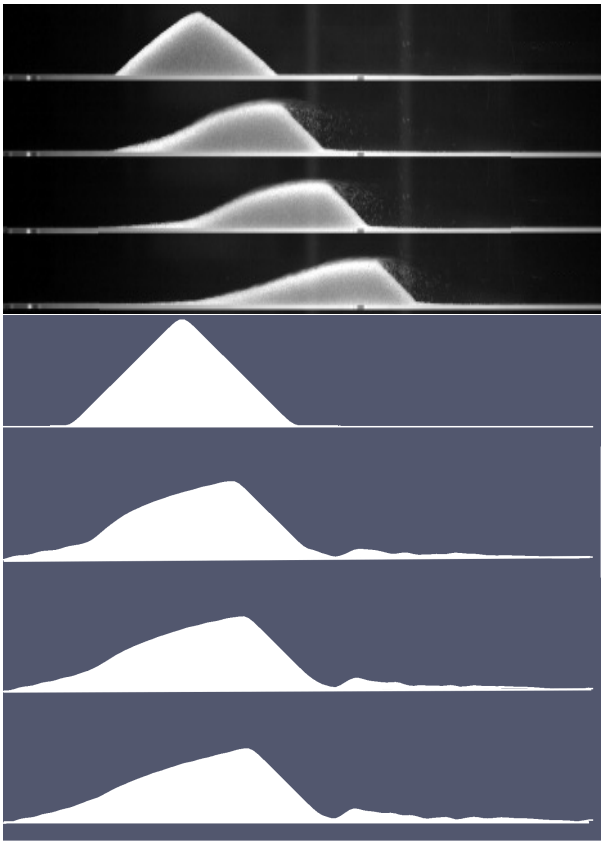

Fig. 9.9: Lateral view of a dune profile from an experiment from (Groh et al., 2009) (top) and the numerical simulation (bottom). In both experiments the dune evolves from an initially symmetric pile of sand over time. The classical dune geometry of a leeside limited by the angle of repose and a slightly increasing luvside is visible. Despite the fact that the numerical setting is different in size and physical time compared to the experimental data, the basic features of the real experiments are recovered and comparable.

of different parameters it reproduces the formation of the asymmetric shape of the dune over time. Both experimental assemblies start at the beginning with a symmetric pile of sand with identical leeside and luvside slope angles. This symmetric sand body is transformed into an asymmetric dune body with a slightly increasing luvside and a steep leeside slope. A further quantitative direct comparison in this case is not possible due to computational limitations.

In conclusion, the full numerical fluid sediment model is able to reproduce the complex transport processes leading to the formation of dunes. The transport of the suspended material as well as the morphological changes are sufficiently resolved. A further vali-

dation of the numerical model with experimental data needs more computational time on the one hand and additional informations about experimental setup in Groh et al. (2009) on the other hand.

9.3 Two phase bed load transport example - Flow round a set of bridge piers

The third and final example for the developed numerical algorithm demonstrates a two phase water and air flow round three obstacles in combination with a sediment bed which changes due to the transport. As a two phase flow is regarded the suspension load model has to be omitted because of the lack of a handling of a suspension transport across the fluid interface available. Therefore, only bed load transport is regarded and the suspended material is neglected. Nevertheless, the phase simulation with an erodible sediment bed gives some indication of the erosional and the depositional processes under a moving free fluid surface.

9.3.1 Experimental setting

Similar to the examples above, a channel with $6\,m \times 1.75\,m \times 2\,m$ is filled with water, air, a step and three obstacles. With a spatial resolution of $240 \times 70 \times 80$ the grid size results in $dx = 0.025\,m$. The step next to the left wall and the rectangular obstacle in the middle are exactly resolved by the flag field approach, whereas both cylinders further downstream are handled by the level set geometry approach, compare Figure (9.10). With the beginning of the simulation the flow is driven by an inflow velocity of $u = 1\,m/s$ above the step for the water phase and the air phase is in rest. At all obstacles Dirichlet boundary conditions are imposed and at all other walls homogeneous Neumann boundary conditions simulate frictionless slip walls. Both, the viscosity and the density of the fluids are chosen to mimic a realistic water and air fluid system. Accordingly, the surface tension for water and air is chosen as $\sigma = 7.2 \cdot 10^{-2} N/m$. The simulation ends after $8\,s$ physical time. In this time the evolution of the flow as well as the sediment bed is studied. For the sediment bed a grain size of $d = 0.001\,m$ is used. This grain size is in the range of a fine sand. The Engelund Hansen transport model is chosen to compute the bed load transport with $f_h = 3 \cdot 10^{-4}$. Equally to the other examples the critical

angle of repose is set to $\alpha_c = 40°$. The geometric setting in Figure (9.10) and the choice of the parameters in Table (9.3) simulate a flow system near a set of bridge piers with a bed of fine sand at the bottom of the domain.

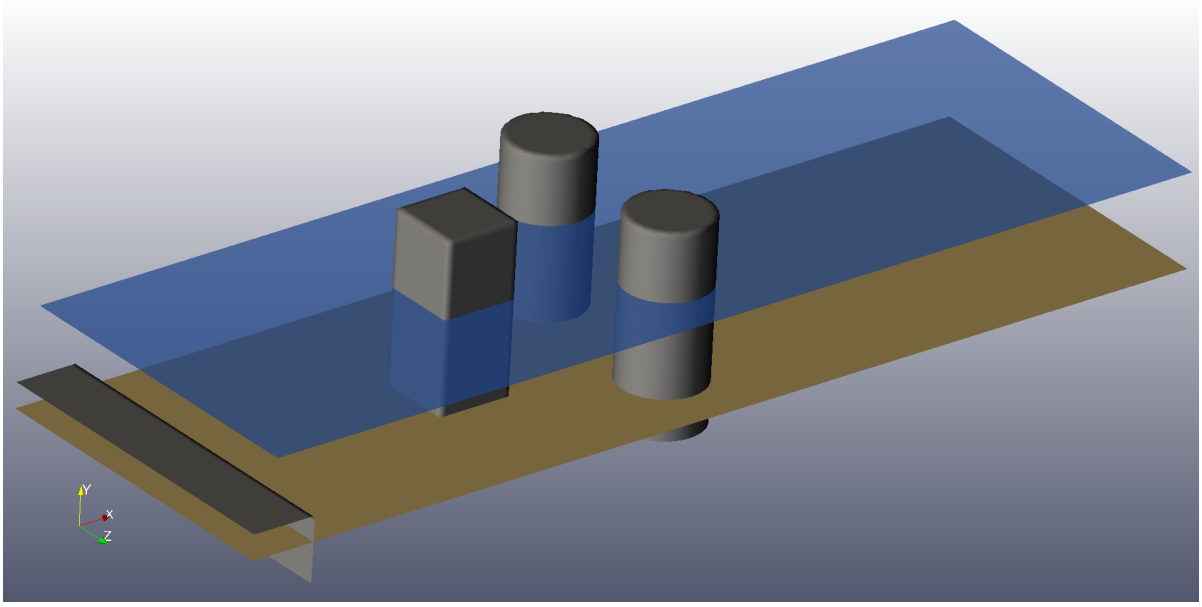

Fig. 9.10: Starting configuration for the two phase flow round three obstacles with an erodible sediment bed. The flow direction is from the left to the right. A constant velocity $u = 1\,m/s$ is set in the water phase above a rectangular step. The channel dimensions are $6\,m \times 1.75\,m \times 2\,m$. In the middle of the channel one rectangular and two cylindrical obstacles are placed to simulate bridge piers. Table (9.3) summarises the chosen parameters to reproduce a realistic water and air system.

9.3.2 Evaluation and discussion of the numerical result

Figure (9.13) demonstrates the temporal evolution of the free surface in comparison with the underlying and changing sediment bed. During the initial phase a wave flows round the three obstacles and forms a wake system which decreases with progressing time. This wave is caused by the inflow velocity at the left wall in combination with an initially resting fluid. After that a complex combination of several wakes establishes near the bridge piers. At the same time the originally flat sediment bed is transformed. Several erosional and depositional sites develop near the obstacles. These complicated scours and ridges influence and interact with each other. In front of the piers a deposition of the

Table 9.3: Computational parameters and setting for the two phase flow and the sediment simulation presented in Figure (9.10).

NaSt3D					
Dimensions	Temporal scheme	Convective scheme	PoissonSolver	it_{max}	ε
$6.0\,m \times 1.75\,m \times 2.0\,m$	AdamsBashforth 2nd	QUICK	BiCGStab	12000	10^{-8}
surface tension σ	μ_l	μ_g	ρ_l	ρ_g	Tfin
$7.2 \cdot 10^{-2} N/m$	$10^{-3} kg/(m \cdot s)$	$1.7 \cdot 10^{-5} kg/(m \cdot s)$	$1000 kg/m^3$	$1.3 kg/m^3$	$8.0 s$
Exner					
Transp.Formula	temporal	spatial	f_h	d_{50}	α_c
Engelund Hansen	AdamsBashforth 2nd	central diff.	$3 \cdot 10^{-4}$	$1\,mm$	$40°$

transported material is visible. Adjacent to the depositional site three deeper depressions build up at the side of the cylindrical obstacles. Here, the deepest point is found between both cylinders and immediately behind the rectangular pier. This depression combines the lateral erosional sites of the cylinders and the rear scour of the rectangular pier. Three depositional ridges are observed further downstream. These forms are built by the eroded material from the scours. A snapshot of the free surface at time $t = 6\,s$ is visualised in Figure (9.11).

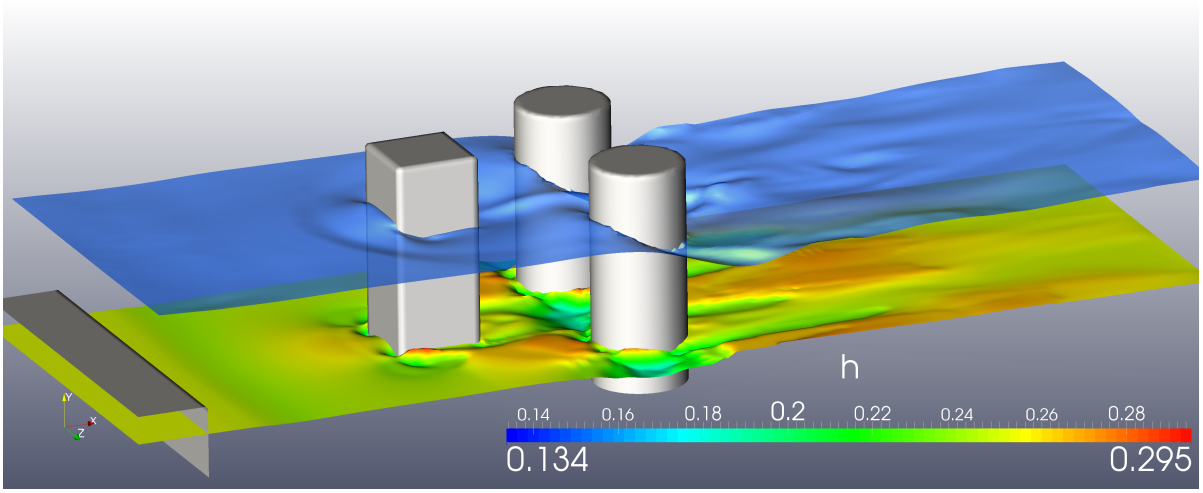

Fig. 9.11: A visualisation of the free fluid surface and the sediment bed height after $6\,s$. A wake system forms near the piers and the sediment bed is transformed simultaneously by a the flow induced transport.

The free surface visualisation in Figure (9.13) illustrates a wake evolving near the bridge piers. This wake passes the three obstacles and resolves behind the cylinders. Moreover, the morphology of the sediment bed shows the various combinations of depressions and ridges. Figure (9.12) demonstrates the flow system and the resulting sediment transport rates. Here, the visualisation of the velocities presents the complex flow patterns and the vortices next to the obstacles. Furthermore, a symmetric flow round the rectangular pier separates and transitions into two vortex systems near both cylinders. A combination of upward and downward flows at varying speeds develops behind these cylinders.

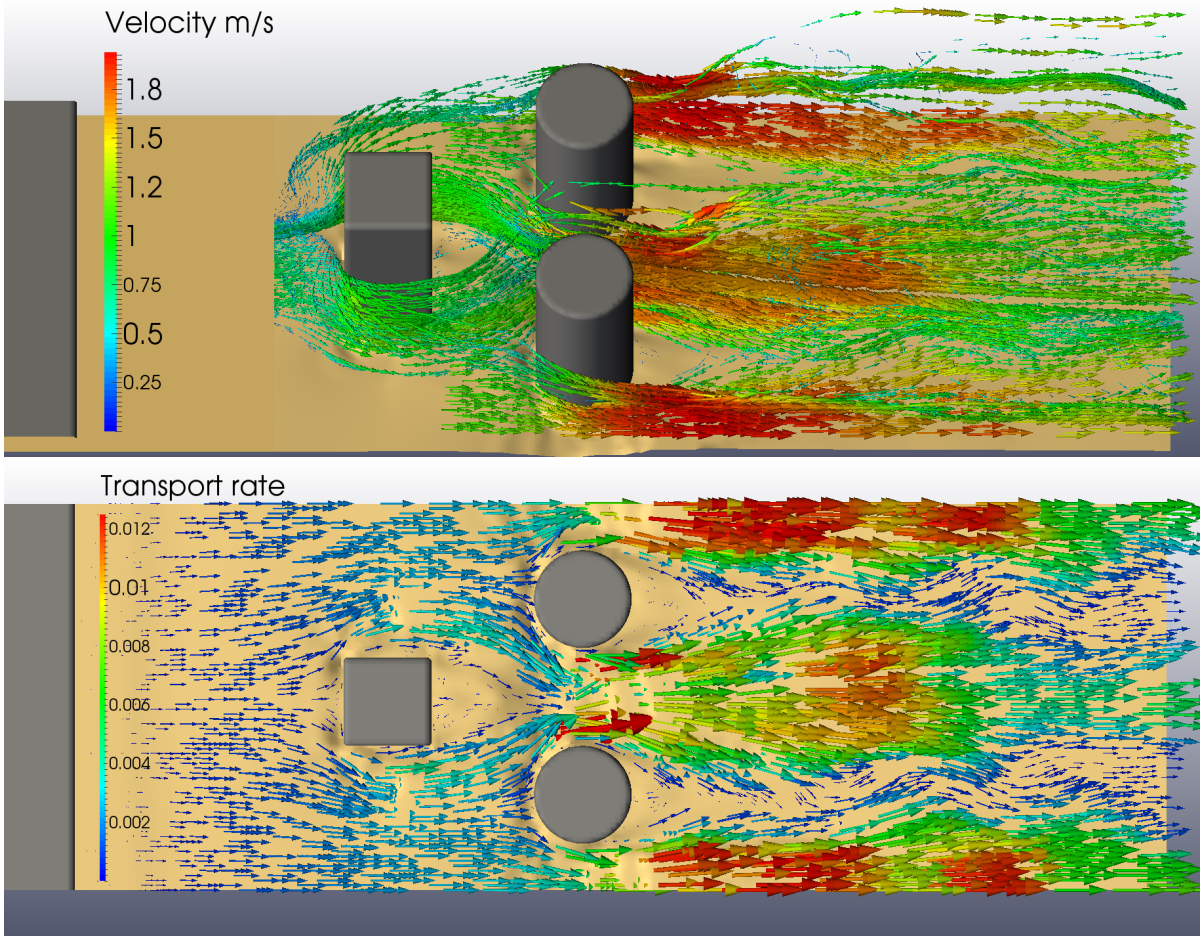

Fig. 9.12: The illustration of the the flow situation and the resulting transport rate at $t = 6\,s$. Top: Illustration of the flow field round the obstacle. The Glyph() filter provided in Paraview is used to visualise the velocities near the bridge piers. Only the flow field round the obstacles and further downstream is illustrated. Bottom: A vector visualisation of the transport rates calculated from the velocity field at the bottom.

The second illustration in Figure (9.12) shows a Glyph() visualisation of the sediment transport rates which result from the described flow and the velocity field. Therefore, a similar vortex situation for the transport rates arises as in the fluid velocities. Equally, a symmetric transport of the sediment at the rectangular pier transitions into two symmetric sediment transport regimes. Behind the obstacles the magnitude of the transport varies with the maxima near the lateral walls. Two transport patterns behind the cylinder are similar to the vortex street known from the flow itself. These patterns are symmetric and show a sinusoidal characteristic.
In summary, the fully coupled algorithm is applied to a two phase flow round arbitrarily shaped obstacles with a movable sediment surface. Accordingly, the evolution of the free surface in interaction with the simultaneously changing sediment surface during the flow is well recovered. The typical erosional features like the scours and the ridges are reproduced by the simulation. An extensive comparison with engineering fluid studies is necessary to validate the presented approach and to further investigate the range of applicability to a two phase flow simulation including the sediment transport.
In conclusion, this example is designed to demonstrate all parts developed in this thesis together in one simulation. First, the Navier Stokes solver for a two phase flow on a level set bounded fluid domain yields a sufficiently well resolved flow and velocities which are used to calculate the transport rates, compare Figure (9.12). Second, the transport rates enter into the bed level equation which in turn determines the new sediment height which is mapped back onto the new fluid domain for the Navier Stokes solver. Third, the slope limiter algorithm ensures the strict observance of the critical angle of repose for the sediment.

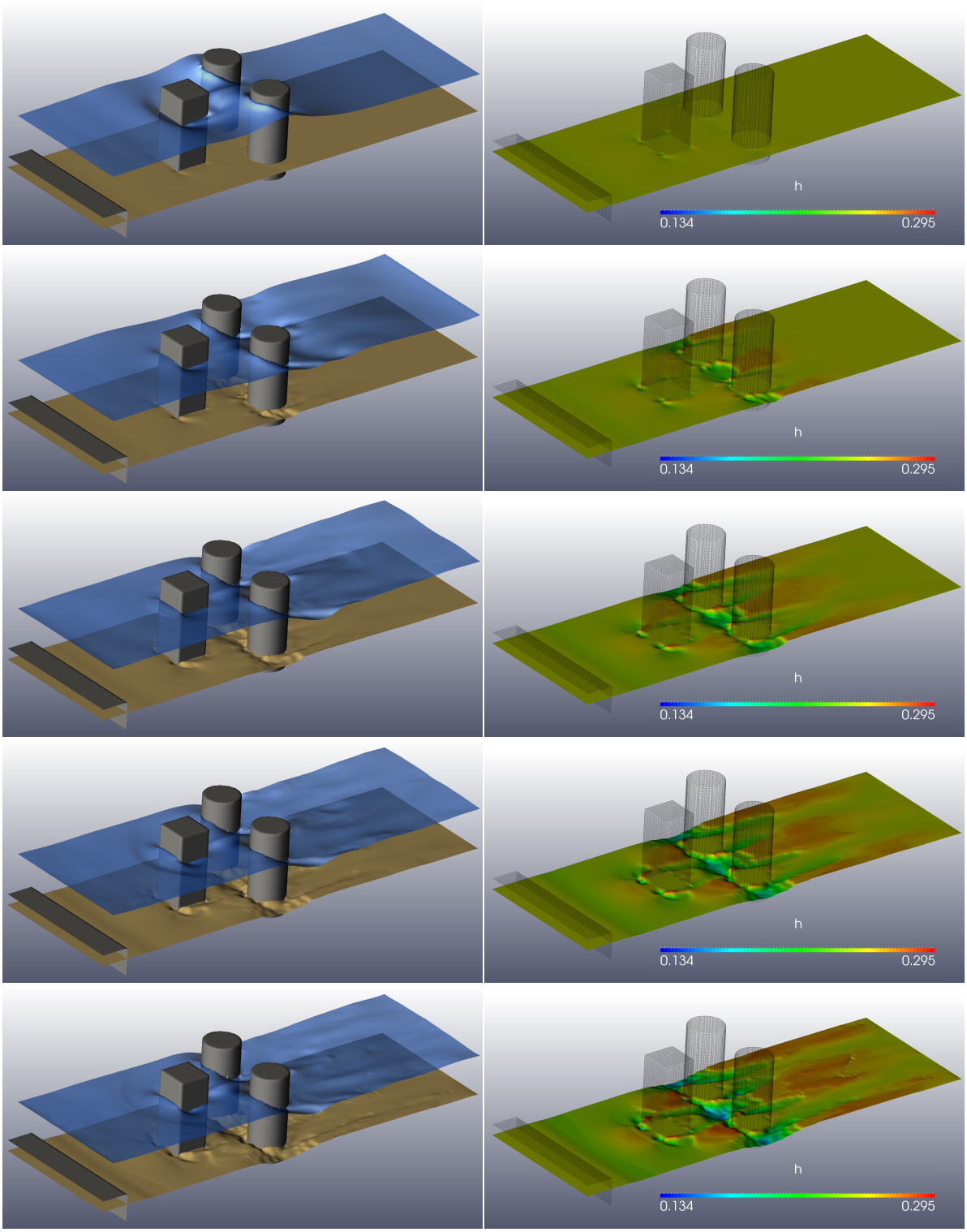

Fig. 9.13: The temporal evolution of the two phase interface with the underlying sediment bed (left) and sediment height (right) at the time steps $t = \{1.25\,s, 2.75\,s, 4.25\,s, 5.75\,s, 7.25\,s\}$. For a better visibility of the sediment height the obstacles are presented as wireframe geometries.

10 Conclusion

The introduction outlined the focus of this thesis: The aim was to provide a numerical algorithm which is able to simulate the flow of two fluids and the sedimentary processes driven by this flow. A sophisticated treatment of a flow with complex geometries and the physically correct simulation of the concurrent sediment transport was necessary. Therefore, the theory and the implementation of these two major parts were discussed. On the one hand it was able to expand the two phase flow solver NaSt3D for the incompressible Navier Stokes equations by a treatment for the level set geometries. On the other hand it was possible to implement a full sediment transport model and the coupling with NaSt3D.

In the first part of this thesis the main topic was to improve the geometry handling in the fluid solver NaSt3D. The existing flag field approach could be replaced by a level set formulation for the geometries. With this setting it was possible to reformulate the pressure projection method used in NaSt3D in two major positions.

First, the Poisson equation with homogeneous Neumann boundary conditions on the prescribed level set geometries had to be solved. The presented approach utilized the boundary normals given by the gradient of the level set function to formulate an appropriate interpolation and discretization scheme for the Neumann boundary conditions. At this point the resulting discretization of the gradient of the level set function was of second order which supersedes the previous geometry handling by the flag field approach. With the new interpolation of the boundary conditions it was able to achieve a new and flexible incorporation of the Neumann boundary conditions into the discretized Poisson system matrix. Here, it was significant to stabilize the resulting linear system including the adapted Poisson matrix and to solve the system efficiently by a stabilized BiCG solver. At this point the stabilization technique preserved the efficient parallelization of the solver. Convergence results for an analytical test function showed a second order convergence inside the domain and a first order convergence near the boundary.

Second, it was possible to construct a technique which allows to impose Dirichlet boun-

dary conditions for the fluid velocities at the level set geometries. With a near boundary interpolation technique following the normals, a finite difference discretization of the Dirichlet boundary conditions was prescribed for the velocity components in the prediction and projection steps. In the computation of the right hand side of the Poisson problem, the implementation of the Dirichlet conditions was applied to the divergence of the predicted velocities. With this step the divergence free condition on the predicted velocities was implicitly fulfilled beside the intrinsic interpolation error. It was able to conduct a convergence study for a three dimensional flow round a spherical obstacle, which yielded a second order convergence for the velocity components.

The second part of this thesis introduced a detailed description of a full sediment transport model and its coupling to the aforementioned fluid solver on the level set geometries. First, the evolution of the morphology of the sediment bed was modelled by the bed level equation from Exner (1925). Here, the bed load transport was calculated either by the formulas after Meyer-Peter & Müller (1948) or Engelund & Hansen (1967). Moreover, the suspension load transport was described by an advection diffusion model with an additional term to take any gravitational settling into account. In detail, for this gravitational settling a model for a spherical particle was used to predict the settling velocity of the particles, which entered the suspension load model. It was managed to realize a mass conserving interchange of the material between the bed load and the suspension load models by the source and the sink terms near the sediment bed boundary. Both models were discretized on a staggered grid with second order finite difference schemes in space and time. The third part in the sediment modeling focused on the limiting of the slope angles. Here, it was essential to develop a non linear heat equation with discontinuous coefficients and to solve the model on the same grid as the sediment model. A finite difference discretization with central differences was applied and yielded a first order convergence for an analytical convergence test case.

Second, the described sediment model allowed a coupling with the previously developed fluid solver on the level set geometries. Both the bed load and the suspension load transport model used the fluid velocities from the solver to calculate the transport of the material or the new sediment height. The opposite direction in the coupling involved the effects of the sediment concentration on the fluid and the change of the fluid domain. A Boussinesq approximation was used to calculate an additional force in the momentum equation of the Navier Stokes equations which results from a buoyancy force in the term for the volume forces. Furthermore, it was possible to construct a remapping of the new

sediment surface and its level set formuation of the fluid domain. Here, a local initial approximation of the distance property was improved by a reinitialization procedure leading to a new level set function for the fluid domain. All the three parts of this computation, the fluid velocities, the buoyancy term, and the new sediment surface, were fully coupled by a loosely partitionend coupling approach. This lead to an explicit coupling formulation for the full system consisting of a flow solver, the bed level equation, and the suspension load model. Herein, the smallest time step restriction of all three parts was used for the full approach. Equally to all other newly developed parts in this thesis a convergence study for the fully coupled system yielded a pre-asymptotic first order convergence which seems to improve into an asymptotic second order convergence.

Overall, a series of numerical simulations brought this thesis to a conclusion introducing different parts of the full algorithm step by step. Erosional and depositional features without any suspension load were tested numerically and analysed in a first single phase example with a flow round a cylindrical obstacle with hemisphere. Further, it was able to simulate the temporal evolution of a barchanoid dune from a initial cross pile of sand with the full model. Here, it was possible to compare qualitatively the numerical simulation with laboratory results from the literature. Finally, a simulation of a two phase flow round obstacles imitating a set of bridge piers was demonstrated the ability of the algorithm to simulate complex two phase flows with a moveable sediment bed beneath the fluid surface.

In summary, a new three dimensional model for a fluid sediment system was developed, discretized, and solved in this thesis. The numerical simulation of a flow through level set geometries and a sediment model were developed, implemented, and tested successfully. The morphological change, the transport of a sediment concentration, the interchange of mass, the slope behaviour, and the fluid flow itself were well recovered and produced convincing results. Each part was tested numerically and showed satisfying convergence rates. All together the numerical examples proved the applicability of the presented algorithm to realistic phenomena from engineering and geosciences.

Outlook

Following the presented algorithm there are a lot of conceivable applications, improvements, and extensions.

First, all the modeling which had not been tackled in this thesis are possible extensions for

future projects. For example a model for the interchange of suspended material across the fluid interface would be a challenging and interesting topic that would widen the range of applicability. Ecological, oceanic or meteorological sciences show a strong interest in the transition from dust particles from the air into the ocean and its deposition or transport. Related topics like the fertilization of the ocean and its nutrient cycle or the deposition of contaminamts in the body of water are possible practical applications. Furthermore, the coupling of the concentration transport with the Navier Stokes equations is limited to small density differences. Here, the density dependence of the Navier Stokes equation and an appropriate coupling would offer the possibility to simulate gravity currents like underwater avalanches or turbidity currents on the seafloor. In this context the water saturated sediment could be modelled and simulated as a non newtonian fluid. The first step how to add a non newtonian model to NaSt3D was described by Griebel & Rüttgers (2014). Additionally, a model to couple the slope limiter with the Navier Stokes system could include the forces acting on the fluid during the sliding of the sediment and vice versa.

Second, the improvements of the applied discretization schemes and techniques in the Navier Stokes equations as well as in the sediment models are always desirable. Especially, stable higher order schemes would enhance the performance of the algorithm in general. In detail, higher order discretization schemes for the slope limiter algorithm could possibly increase the rate of the full algorithm in the pre-asymptotic regime, since the slope limiter influences the simulation on coarse grids more than on fine grids. In general, the most computational time is spent in the Poisson solver. Therefore, a full analysis of the possible stabilization techniques for the Poisson solver could lead to a more sophisticated understanding of the iteration behaviour and to the possible performance enhancements.

Third, there is an enormous variety of further applications. Engineers and technicians would benefit from a numerical simulation of the erosion and the sediment transport under coastal waves. A wave generator was previously realised in NaSt3D by Peuker (2014) and could be added to the presented algorithm from this thesis. In this context, an optimization study concerning the shape of structures could be tackled. Shape optimization studies were previously conducted with NaSt3D by Behm (2014). Generally, a full fluid structure interaction as presented in Croce (2010) could enable a wide range of engineering applications. Moreover, a quantification of the uncertainty in the parameters in this context was presented by Zaspel (2015) and would be applicable to the sediment

and the fluid parameters as well. Other topics like soil erosion, pollutant deposition, the reconstruction of the genesis of morphological features, and many other applications from different disciplines are worth to reflect more closely.
All in all, the introduced tools could be easily adapted to a large variety of problems and fields. Someone just has to pick up the existing threads.

Acknowledgement

I would like to thank all the people that helped me to complete this thesis. First of all, I would like to thank my advisor Prof. Dr. Michael Griebel for introducing me to this topic. The excellent working conditions and the opportunity to participate in the scientific community at several scientific conferences were an essential step towards this thesis. Furthermore, I would like to thank the committee member Prof. Dr. Marc Alexander Schweitzer for providing the second opinion on this dissertation.
Big thanks go to the last survivors of the fluid dynamics section at the INS: Alexander Rüttgers and Peter Zaspel. Both provided a very helpful proof reading and endless hours of great discussions over the last years. Moreover, the biggest thanks go to Hanna who carefully read the whole thesis and almost became exasperated with the „math stuff“. Moreover, all numerical simulations were impossible without the great students and Ralph Thesen from our IT–Team who maintained the workstations and the cluster system at the INS. Thanks a lot.
Last but not least, I thank my family for the all the support and encouragement.
At this point I would like to express my deep gratitude to Hanna for all her patience, encouragement, and support in every situation.

Literature

Ackers, P., & White, W. (1973). Sediment transport: New approach and analysis. *Journal of the Hydraulics Division*, *99*(11), 2041–2060.

Adelsberger, J., Esser, P., Griebel, M., Groß, S., Klitz, M., & Rüttgers, A. (2014). 3D incompressible two-phase flow benchmark computations for rising droplets. In *Proceedings of the 11th World Congress on Computational Mechanics (WCCM XI), Barcelona, Spain*. Also available as INS Preprint No. 1401 and as IGPM Preprint No. 393.

Amann, H. (2000). On the strong solvability of the Navier Stokes equations. *Journal of Mathematical Fluid Mechanics*, *2*(1), 16–98.

Amann, H. (2003). Navier-Stokes equations with nonhomogeneous Dirichlet data. *Journal of Nonlinear Mathematical Physics*, *10*(sup1), 1–11.

Bagnold, R. A. (1966). An approach to the sediment transport problem from general physics. *U.S. Geological Survey Professional Paper*, *422-1*, v+37.

Barrett, J. W., Garcke, H., & Nürnberg, R. (2015). Stable finite element approximations of two-phase flow with soluble surfactant. *Journal of Computational Physics*, *297*, 530–564.

Batschelet, E. (1952). Über die numerische Auflösung von Randwertproblemen bei elliptischen partiellen Differentialgleichungen. *Zeitschrift für angewandte Mathematische Physik*, *3*, 165–193.

Bayram, A., Larson, M., Miller, H. C., & Kraus, N. C. (2001). Cross-shore distribution of longshore sediment transport: Comparison between predictive formulas and field measurements. *Coastal Engineering*, *44*(2), 79–99.

Bechteler, W. (2008). *Sediment sources and transport processes*. Inst. für Wasserwesen.

Behm, O. (2014). *Shape optimization in incompressible Navier-Stokes flows*. Masterarbeit, Institut für Numerische Simulation, Universität Bonn.

Benjamin, T. B. (1968). Gravity currents and related phenomena. *Journal of Fluid Mechanics*, *31*(02), 209–248.

Boeker, P., Wittkowski, M., Wallenfang, O., Koster, F., Croce, R., Griebel, M., Diekmann, B., & Schulze-Lammers, P. (2001). Tracerverfahren zur Validierung von Ausbreitungsmodellen für Geruchsemissionen. *Agrartechnische Forschung, Landtechniknet*, (pp. 92–97).

Bonnecaze, R. T., Huppert, H. E., & Lister, J. R. (1993). Particle-driven gravity currents. *Journal of Fluid Mechanics*, *250*, 339–369.

Borazjani, I., Ge, L., & Sotiropoulos, F. (2008). Curvilinear immersed boundary method for simulating fluid structure interaction with complex 3D rigid bodies. *Journal of Computational Physics*, *227*(16), 7587–7620.

Bouchon, F., & Peichl, G. H. (2007). A second-order immersed interface technique for an elliptic Neumann problem. *Numerical Methods for Partial Differential Equations*, *23*(2), 400–420.

Boussinesq, J. (1903). *Theorie analytique de la chaleur*, vol. 2. Gathier–Villars.

Brackbill, J., Kothe, D., & Zemach, C. (1992). A continuum method for modeling surface tension. *Journal of Computational Physics*, *100*(2), 335–354.

Bramble, J. H., & Hubbard, B. E. (1965). A finite difference analog of the Neumann problem for Poisson's equation. *SIAM Journal on Numerical Analysis*, *2*, 1–14.

Brenk, M., Bungartz, H.-J., Mehl, M., Muntean, I. L., Neckel, T., & Weinzierl, T. (2008). Numerical simulation of particle transport in a drift ratchet. *SIAM Journal on Scientific Computing*, *30*(6), 2777–2798.

Burkow, M., & Griebel, M. (2015). Towards the three-dimensional numerical simulation of fluvial geomorphological processes. *Zeitschrift für Geomorphologie*, *58*(3), 15–32.

Burkow, M., & Griebel, M. (2016). A full three dimensional numerical simulation of the sediment transport and the scouring at a rectangular obstacle. *Computers & Fluids*, *125*, 1–10.

Campos, R. (2001). *Three-dimensional reservoir sedimentation model*. Ph.D. thesis, University of Newcastle, Faculty of Engineering.

Chanson, H. (1999). *The Hydraulics of Open Channel Flow - An Introduction*. London: Edward Arnold.

Cheng, N. (1997). Simplified settling velocity formula for sediment particle. *Journal of Hydraulic Engineering*, *123*(2), 149–152.

Chorin, A. J. (1967). A numerical method for solving incompressible viscous flow problems. *Journal of Computational Physics*, *2*(1), 12–26.

Chorin, A. J. (1968). Numerical solution of the Navier-Stokes equations. *Journal: Math. Comp.*, *22*, 745–762.

Coleman, S. E., & Nikora, V. I. (2009). Exner equation: A continuum approximation of a discrete granular system. *Water Resource Research*, *45*, 1–8.

Croce, R. (2002). *Ein paralleler, dreidimensionaler Navier-Stokes-Löser für inkompressible Zweiphasenströmungen mit Oberflächenspannung, Hindernissen und dynamischen Kontaktflächen*. Diplomarbeit, Insitut für Numerische Mathematik, Universität Bonn.

Croce, R. (2010). *Numerische Simulation der Interaktion von inkompressiblen Zweiphasenströmungen mit Starrkörpern in drei Raumdimensionen*. Dissertation, Institut für Numerische Simulation, Universität Bonn, Bonn, Germany.

Croce, R., Griebel, M., & Schweitzer, M. A. (2004). A parallel level-set approach for two-phase flow problems with surface tension in three space dimensions. Preprint 157, Sonderforschungsbereich 611, Universität Bonn.

Croce, R., Griebel, M., & Schweitzer, M. A. (2009). Numerical simulation of bubble and droplet-deformation by a level set approach with surface tension in three dimensions. *International Journal for Numerical Methods in Fluids*, *62*(9), 963–993.

Daintith, J. (2009). *A Dictionary of Physics*. Oxford Paperback Reference. OUP Oxford.

D'Alessio, S., Moodie, T. B., Pascal, J., & Swaters, G. (1996). Gravity currents produced by sudden release of a fixed volume of heavy fluid. *Studies in Applied Mathematics*, *96*(4), 359–386.

Degroote, J., Bathe, K.-J., & Vierendeels, J. (2009). Performance of a new partitioned procedure versus a monolithic procedure in fluid - structure interaction. *Computers & Structures*, *87*(11-12), 793–801. Fifth MIT Conference on Computational Fluid and Solid Mechanics.

Degroote, J., Bruggeman, P., Haelterman, R., & Vierendeels, J. (2008). Stability of a coupling technique for partitioned solvers in FSI applications. *Computers & Structures*, *86*(23-24), 2224–2234.

Deriaz, E. (2012). Stability conditions for the numerical solution of convection-dominated problems with skew-symmetric discretizations. *SIAM J. Numerical Analysis*, *50*(3), 1058–1085.

Destefano, L. (2011). http://gadling.com/tag/mojave-desert/.

Diamant, H., Ariel, G., & Andelman, D. (2001). Kinetics of surfactant adsorption: The free energy approach. *Colloids and Surfaces A: Physicochemical and Engineering Aspects*, *183-185*, 259–276.

Dietrich, W. E. (1982). Settling velocity of natural particles. *Water Resour. Res.*, *18*(6), 1615–1626.

Dixen, M., Sumer, B. M., & Fredsoe, J. (2013). Numerical and experimental investigation of flow and scour around a half-buried sphere. *Coastal Engineering*, *73*, 84–105.

Einstein, H. A. (1950). *The bed-load function for sediment transportation in open channel flows*. No. 1026 in Technical bulletin. U.S. Dept. of Agriculture, United States. Dept. of Agriculture.

Engelund, F., & Hansen, E. (1967). *A monograph on sediment transport in alluvial streams*. Kopenhagen: Teknisk Forlag.

Euler, T., & Herget, J. (2011). Obstacle-Reynolds-number based analysis of local scour at submerged cylinders. *Journal of Hydraulic Research*, *49*(2), 267–271.

Euler, T., & Herget, J. (2012). Controls on local scour and deposition induced by obstacles in fluvial environments. *Catena*, *91*, 35–46.

Exner, F. M. (1925). Über die Wechselwirkung zwischen Wasser und Geschiebe in Flüssen. *Sitzungsbericht Akademie der Wisssenschaft Wien*, *134*, 165–180.

Farhat, C., Lesoinne, M., & Maman, N. (1995). Mixed explicit/implicit time integration of coupled aeroelastic problems: Three-field formulation, geometric conservation and distributed solution. *International Journal for Numerical Methods in Fluids*, *21*(10), 807–835.

Farwig, R. (1992). The stationary exterior 3 D-problem of Oseen and Navier-Stokes equations in anisotropically weighted Sobolev spaces. *Mathematische Zeitschrift*, *211*(1), 409–447.

Farwig, R., Kozono, H., & Sohr, H. (2007). Very weak solutions of the Navier-Stokes equations in exterior domains with nonhomogeneous data. *Journal of the Mathematical Society of Japan*, *59*(1), 127–150.

Fefferman, C. L. (2000). Existence and smoothness of the Navier-Stokes equation. The Clay Mathematics Institute – Millenium Problems.

Feireisl, E., & Novotný, A. (2012). Weak-strong uniqueness property for the full Navier-Stokes-Fourier system. *Archive for Rational Mechanics and Analysis*, *204*(2), 683–706.

Felippa, C. A., & Geers, T. L. (1988). Partitioned analysis for coupled mechanical systems. *Engineering Computations*, *5*(2), 123–133.

Felippa, C. A., Park, K., & Farhat, C. (2001). Partitioned analysis of coupled mechanical systems. *Computer Methods in Applied Mechanics and Engineering*, *190*(24-25), 3247–3270. Advances in Computational Methods for Fluid-Structure Interaction.

Ferguson, R. I., & Church, M. (2004). A simple universal equation for grain settling velocity. *Journal of Sedimentary Research*, *74(6)*, 933–937.

Flood, S. (undated). http://www.gettyimages.co.uk/detail/photo/namibia-skeleton-coast-sand-dunes-high-res-stock-photography/sb10067261u-001.

Galdi, G. (1994). *An Introduction to the Mathematical Theory of the Navier-Stokes Equations: Linearized steady problems*. An Introduction to the Mathematical Theory of the Navier-Stokes Equations. Springer-Verlag.

Garcke, H., Lam, K. F., & Stinner, B. (2014). Diffuse interface modelling of soluble surfactants in two-phase flow. *Communications in Mathematical Science*, *12*(8), 1475–1522.

Griebel, M., Dornseifer, T., & Neunhoeffer, T. (1998). *Numerical Simulation in Fluid Dynamics, a Practical Introduction*. Philadelphia: SIAM.

Griebel, M., & Klitz, M. (2013). Simulation of droplet impact with dynamic contact angle boundary conditions. In *Singular Phenomena and Scaling in Mathematical Models*, (pp. 297–325). Springer International Publishing Switzerland. INS Preprint No. 1302.

Griebel, M., & Rüttgers, A. (2014). Multiscale simulations of three-dimensional viscoelastic flows in a square-square contraction. *Journal of non-Newtonian Fluid Mechanics*, *205*, 41–63. Also available as INS Preprint No. 1313.

Griebel, M., & Zaspel, P. (2010). A multi-GPU accelerated solver for the three-dimensional two-phase incompressible Navier-Stokes equations. *Computer Science - Research and Development*, *25*(1–2), 65–73.

Groh, C., Rehberg, I., & Kruelle, C. A. (2009). How attractive is a barchan dune? *New Journal of Physics*, *11*(2), 023014.

Guermond, J., Minev, P., & Shen, J. (2006). An overview of projection methods for incompressible flows. *Computer Methods in Applied Mechanics and Engineering*, *195*(44-47), 6011–6045.

Guermond, J.-L. (1994). Sur l'approximation des equations de Navier-Stokes instationnaires par une methode de projection. *C.R. Acad. Sci. Paris*, *319*, 887–892.

Guermond, J.-L., & Quartapelle, L. (1998). On the approximation of the unsteady Navier-Stokes equations by finite element projection methods. *Numerische Mathematik*, *80*(2), 207–238.

Hackbusch, W. (1992). *Elliptic differential equations : Theory and numerical treatment*. Springer.

Hallermeier, R. J. (1981). Terminal settling velocity of commonly occurring sand grains. *Sedimentology*, *28*, 859–865.

Heathershaw, A. (1981). Comparisons of measured and predicted sediment transport rates in tidal currents. In C. Nittrouer (Ed.) *Sedimentary Dynamics of Continental Shelves*, vol. 32 of *Developments in Sedimentology*, (pp. 75–104). Elsevier.

Hjulstroem, F. (1955). Transportation of Detritus by moving water. In *Recent Marine Sediments*, vol. 4, (pp. 5–31). Society for Sedimentary Geology (SEPM).

Hopf, E. (1950). Über die Anfangswertaufgabe für die hydrodynamischen Grundgleichungen. Erhard Schmidt zu seinem 75. Geburtstag gewidmet. *Mathematische Nachrichten*, *4*(1-6), 213–231.

James, S. C., Jones, C. A., Grace, M. D., & Roberts, J. D. (2010). Advances in sediment transport modelling. *Journal of Hydraulic Research*, *48*(6), 754–763.

Jamet, P., Lascaux, P., & Raviart, P.-A. (1970). Une méthode de résolution numérique des équations de Navier-Stokes. *Numerische Mathematik*, *16*(2), 93–114.

Jomaa, Z., & Macaskill, C. (2005). The embedded finite difference method for the Poisson equation in a domain with an irregular boundary and Dirichlet boundary conditions. *Journal of Computational Physics*, *202*(2), 488–506.

Jomaa, Z., & Macaskill, C. (2010). The Shortley-Weller embedded finite-difference method for the 3D Poisson equation with mixed boundary conditions. *Journal of Computational Physics*, *229*(10), 3675–3690.

Julien, P. (1995). *Erosion and Sedimentation*. Cambridge: Cambridge University Press.

Kammerer, W. J., & Nashed, M. Z. (1972). On the convergence of the conjugate gradient method for singular linear operator equations. *SIAM Journal on Numerical Analysis*, *9*(1), 165–181.

Kantoush, S. A., Bollaert, E., & Schleiss, A. J. (2008). Experimental and numerical modelling of sedimentation in a rectangular shallow basin. *International Journal of Sediment Research*, *23*(3), 212–232.

Kato, T. (1972). Nonstationary flows of viscous and ideal fluids in $\mathbb{R}^3$. *Journal of Functional Analysis*, *9*(3), 296–305.

Kato, T. (1984). Strong lp-solutions of the Navier-Stokes equation in $\mathbb{R}^m$, with applications to weak solutions. *Mathematische Zeitschrift*, *187*, 471–480.

Khosronejad, A., Kang, S., Borazjani, I., & Sotiropoulos, F. (2011). Curvilinear immersed boundary method for simulating coupled flow and bed morphodynamic interactions due to sediment transport phenomena. *Advances in Water Resources*, *34*(7), 829–843.

Khosronejad, A., Kang, S., & Sotiropoulos, F. (2012). Experimental and computational investigation of local scour around bridge piers. *Advances in Water Resources*, *37*(0), 73–85.

Klitz, M. (2014). *Numerical Simulation of Droplets with Dynamic Contact Angles*. Dissertation, Institut für Numerische Simulation, Universität Bonn.

Knighton, D. (1998). *Fluvial Forms and Processes: A New Perspective*. A Hodder Arnold Publication. Arnold.

Kubatko, E. J., & Westerink, J. J. (2007). Exact discontinuous solutions of Exner's bed evolution model: Simple theory for sediment bores. *Journal of hydraulic engineering*, *133*(3), 305–311.

Kubatko, E. T., Westerink, J. J., & Dawson, C. (2006). An unstructured grid morphodynamic model with a discontinuous Galerkin method for bed evolution. *Ocean Modelling*, *15*, 71–89.

Ladyzhenskaya, O. A. (1969). *The Mathematical Theory of Viscous Incompressible Flow*. Gordon and Breach.

Leray, J. (1934). Sur le mouvement d'un liquide visqueux emplissant l'espace. *Acta Mathematica*, *63*(1), 193–248.

Link, O. (2006). *Untersuchung der Kolkung an einem schlanken zylindrischen Pfeiler in sandigem Boden*. Ph.D. thesis, Fachbereich Bauingenieurwesen und Geodäsie der Technischen Universität Darmstadt.

Long, W., Kirby, J. T., & Shao, Z. (2008). A numerical scheme for morphological bed level calculations. *Coastal Engineering*, *55*, 167–180.

Mahr, L. (1986). On the shallow motion approximations. *J. Atmos. Sci*, *43*, 1036–1044.

Malcherek, A. (2004). Sedimenttransport und Morphodynamik. lecture notes.

Manning, R. (1891). On the flow of water in open channels and pipes. *Transactions of the Institution of Civil Engineers of Ireland*, *20*, 161–207.

Marek, M. (2001). *Simulation des Sedimenttransports in Suspension und als Geschiebe - Ein Vergleich für das Jade-Weser-Astuar*. Master's thesis, Insitut für Wasserwirtschaft und Kulturtechnik, Universität Karlsruhe.

Masuda, K. (1984). Weak solutions of Navier-Stokes equations. *Tohoku Mathematical Journal*, *36*(4), 623–646.

Matsunaga, N., & Yamamoto, T. (2000). Superconvergence of the Shortley-Weller approximation for Dirichlet problems. *Journal of Computational and Applied Mathematics*, *116*(2), 263–273.

Matthies, H. G., & Steindorf, J. (2003). Partitioned strong coupling algorithms for fluid-structure interaction. *Computers & Structures*, *81*(8-11), 805–812. K.J Bathe 60th Anniversary Issue.

Metsch, B. (2013). *Algebraic Multigrid (AMG) for Saddle Point Systems*. Dissertation, Institut für Numerische Simulation, Universität Bonn.

Mewis, P. (2002). *Morphodynamisch-numerische Modellierung von Flusskurven*, vol. 1. Technische Uni Darmstadt Inst. f. Wasserbau u. Wasserwirtschaft.

Mewis, P. (2009). Morphodynamische Simulation der Entwicklung von Flusskurven. In *1. Darmstädter Ingenieurkongress Bau und Umwelt*. TU Darmstadt, FB Bauingenieurwesen und Geodäsie, Darmstadt.

Meyer-Peter, E., & Müller, R. (1948). Formulas for bed-load transport. In *Proceedings of the 2nd Meeting of the International Association for Hydraulic Structures Research*, (pp. 39–64). IAHR, Stockholm, Sweden.

Möller, L. E., Kuhlman, K. R., Marshall, J. R., & Towner, M. C. (2002). The snoopy angle of repose experiment: Calibration of an instrument to determine the angle of repose of Martian dust. *Lunar and Planetary Science*, *33*.

Moodie, T. (2002). Gravity currents. *Journal of Computational and Applied Mathematics*, *144*(1-2), 49–83. Selected papers of the Int. Symp. on Applied Mathematics, August 2000, Dalian, China.

Mulder, W., Osher, S., & Sethan, J. A. (1992). Computing interface motion in compressible gas dynamics. *Journal of Computational Physics*, *100*(2), 209–228.

Officer, C. B. (1982). Fluid and material diffusion coefficient determinations from sediment cores. *Estuarine, Coastal and Shelf Science*, *14*(4), 459–464.

Osher, S., & Fedkiw, R. (2003). *Level set methods and dynamic implicit surfaces*. Applied mathematical sciences. Springer.

Pacheco-Ceballos, R. (1989). Transport of sediments: Analytical solution. *Journal of Hydraulic Research*, *27*(4), 501–518.

Paola, C., & Voller, V. (2005). A generalized Exner equation for sediment mass balance. *Journal of geophysical Research: Earth Surface*, *110*(F4).

Parker, G. (2004). *1D Sediment Transport Morphodynamics with Applications to Rivers and Turbidity Currents*. e-book.

Peuker, C. (2014). *High-dimensional Design Optimization of Wave Energy Converters with Computational Fluid Dynamics*. Masterarbeit, Institut für Numerische Simulation, Universität Bonn.

Raudkivi, A. (1998). *Loose Boundary Hydraulics*. Taylor & Francis.

Razmi, A., Firoozabadi, B., & Ahmadi, G. (2009). Experimental and numerical approach to enlargement of performance of primary settling tanks. *Journal of Applied Fluid Mechanics*, *2 No. 1*, 1–12.

Roberson, J., Cassidy, J., & Chaudhry, H. (1998). *Hydraulic engineering*. Wiley.

Rolinski, S. (1999). On the dynamics of suspended matter transport in the tidal river Elbe: Description and results of a lagrangian model. *Journal of Geophysical Research: Oceans*, *104*(C11), 26043–26057.

Roulund, A., Sumer, B. M., Fredsoe, J., & Michelsen, J. (2005). Numerical and experimental investigation of flow and scour around a circular pile. *Journal of Fluid Mechanics*, *534*, 351–401.

Rüttgers, A., Griebel, M., Pastrik, L., Schmied, H., Wittmann, D., Scherrieble, A., Dinkelmann, A., & Stegmaier, T. (2015). Simulation of the oil storage process in the scopa of specialized bees. *Computers & Fluids*, *119*, 115–130. Also available as INS Preprint No. 1404.

Sauermann, G., Kroy, K., & Herrmann, H. J. (2001). Continuum saltation model for sand dunes. *Phys. Rev. E*, *64*, 031305.

Sauermann, G., Rognon, P., Poliakov, A., & Herrmann, H. (2000). The shape of the barchan dunes of southern Morocco. *Geomorphology*, *36*(1-2), 47–62.

Schwämmle, V., & Herrmann, H. J. (2003). Modelling transverse dunes. *arXiv:cond-mat/0301589v1*.

Sedimentation & River Hydraulics Group (2006). *Erosion and Sedimentation Manual*. , U.S. Department of the Interior Bureau of Reclamation, Denver, Colorado.

Shields, A. (1936). *Anwendung der Ähnlichkeitsmechanik und der Turbulenzforschung auf die Geschiebebewegung*. Ph.D. thesis, Preußische Versuchsanstalt für Wasserbau und Schiffbau Berlin.

Shin, J., Dalziel, S., & Linden, P. (2004). Gravity currents produced by lock exchange. *Journal of Fluid Mechanics*, *521*, 1–34.

Shortley, G., & Weller, R. (1938). The numerical solution of Laplace's equation. *Journal of Applied Physics*, *9*, 334–348.

Sleijpen, G., & Fokkema, D. (1993). Bicgstab(l) for linear equations involving unsymmetric matrices with complex spectrum. *Eletronic Transactions on Numerical Analysis*, *1*, 11–32.

Sleijpen, G., van der Vorst, H., & Fokkema, D. (1994). Bicgstab(l) and other hybrid bi-cg methods. *Numerical Algorithms*, *7*(1), 75–109.

Smagorinsky, J. (1963). General circulation experiments with the primitive equations. *Mon. Wea. Rev.*, *91*, 99–164.

Spiegel, E. A., & Veronis, G. (1960). On the Boussinesq approximation for a compressible fluid. *Astrophysical Journal*, *131*.

Strickler, A. (1923). Beiträge zur Frage der Geschwindigkeitsformel und der Rauhigkeitszahlen für Ströme, Kanäle und geschlossene Leitungen. *Mitteilungen des Amtes für Wasserwirtschaft*, *16*.

Strybny, J., Thorenz, C., Croce, R., & Engel, M. (2006). A parallel 3D free surface Navier-Stokes solver for high performance computing at the german waterways administration. In *The 7th Int. Conf. on Hydroscience and Engineering (ICHE-2006)*. Philadelphia, USA.

Sussman, M., & Puckett, E. G. (2000). A coupled level set and volume-of-fluid method for computing 3d and axisymmetric incompressible two-phase flows. *Journal of Computational Physics*, *162*(2), 301–337.

Sussman, M., Smereka, P., & Osher, S. (1994). A level set approach for computing solutions to incompressible two-phase flow. *J. Comput. Phys.*, *114*, 146–159.

Sussman, M., Smith, K., Hussaini, M., Ohta, M., & Zhiwei, R. (2007). A sharp interface method for incompressible two-phase flows. *Journal of Computational Physics*, *221*(2), 469–505.

Tafarojnoruz, A., Gaudio, R., & F., C. (2012). Bridge pier scour mitigation under steady and unsteady flow conditions. *Acta Geophysica*, *60*, 1076–1097.

Teigen, K., Song, P., Lowengrub, J., & Voigt, A. (2011). A diffuse-interface method for two-phase flows with soluble surfactants. *J. Comput. Phys.*, *230*(2), 375–393.

Temam, R. (1968). Une méthode d'approximation de la solution des équations de Navier-Stokes. *Bull. Soc. Math. France*, *96*, 115–152.

Temam, R. (1977). *Navier-Stokes equations: Theory and numerical analysis*. Studies in Mathematics and its Applications. Amsterdam: North-Holland.

Temam, R. (2001). *Navier-Stokes Equations: Theory and Numerical Analysis*. AMS/Chelsea publication. AMS Chelsea Publications.

van der Pijl, S. P., Segal, A., Vuik, C., & Wesseling, P. (2005). A mass-conserving level-set method for modelling of multi-phase flows. *International Journal for Numerical Methods in Fluids*, *47*(4), 339–361.

van der Vorst, H. A. (1992). Bi-cgstab: A fast and smoothly converging variant of bi-cg for the solution of nonsymmetric linear systems. *SIAM Journal on Scientific and Statistical Computing*, *13*(2), 631–644.

Van Driest, E. R. (1956). On turbulent flow near a wall. *Journal of the Aeronautical Sciences*, *23*, 1007–1011.

Van Rijn, L. C. (1984). Sediment transport, Part I: Bed load transport. *Journal of hydraulic engineering*, *110*(10), 1431–1456.

Van Rijn, L. C. (1993). *Principles of sediment transport in rivers, estuaries and coastal seas*, vol. 1006. Aqua publications Amsterdam.

Verleye, B., Klitz, M., Croce, R., Griebel, M., Lomov, S., Roose, D., & Verpoest, I. (2006). Predicting the permeability of textile reinforcements via a hybrid Navier-Stokes/Brinkman solver. In Binetruy (Ed.) *Proceedings of the 8th International Conference on Flow Processes in Composite Materials (FPCM-8)*, (pp. 65–72). Ecole des Mines de Douai, Douai.

Vierendeels, J., Dumont, K., & Verdonck, P. (2008). A partitioned strongly coupled fluid-structure interaction method to model heart valve dynamics. *Journal of Computational and Applied Mathematics*, *215*(2), 602 – 609. Proceedings of the Third International Conference on Advanced Computational Methods in Engineering (ACOMEN 2005).

Wall, W. A., Genkinger, S., & Ramm, E. (2007). A strong coupling partitioned approach for fluid-structure interaction with free surfaces. *Computers & Fluids*, *36*(1), 169 – 183. Challenges and Advances in Flow Simulation and Modeling.

White, F. (2003). *Fluid Mechanics*. McGraw-Hill international editions. McGraw-Hill.

Wu, A., B. Molinas, & Julien, P. (2004). Bed-material load computations for nonuniform sediments. *Journal of Hydraulic Engineering*, *130*(10), 1002–1012.

Wu, W., Shields, F. D., Bennett, S. J., & Wang, S. S. Y. (2005). A depth-averaged two-dimensional model for flow, sediment transport, and bed topography in curved channels with riparian vegetation. *Water Resources Research*, *41*(3), n/a–n/a.

Yang, C. (1972). Unit stream power and sediment transport. *Journal of the Hydraulics Division*, *98*(10), 1805–1826.

Yang, J., Preidikman, S., & Balaras, E. (2008). A strongly coupled, embedded-boundary method for fluid-structure interactions of elastically mounted rigid bodies. *Journal of Fluids and Structures*, *24*(2), 167–182.

Yang, J., & Stern, F. (2009). Sharp interface immersed-boundary/level-set method for wave - body interactions. *Journal of Computational Physics*, *228*(17), 6590–6616.

Yoon, J.-Y., & Kang, S.-K. (2005). A numerical model of sediment-laden turbulent flow in an open channel. *Canadian Journal Civil Engineering*, *32*, 233–240.

Zanke, U. (2002). *Hydromechanik der Gerinne und Küstengewässer - Für Bauingenieure, Umwelt- und Geowissenschaftler*. Parey Buchverlag, Berlin.

Zaspel, P. (2015). *Parallel RBF Kernel-Based Stochastic Collocation for Large-Scale Random PDEs*. Dissertation, Institut für Numerische Simulation, Universität Bonn.

Zaspel, P., & Griebel, M. (2013). Solving incompressible two-phase flows on multi-GPU clusters. *Computers & Fluids*, *80*(0), 356–364. Selected contributions of the 23rd International Conference on Parallel Fluid Dynamics ParCFD2011, also available as INS Preprint no. 1113.

Zhang, H., Nakagawa, H., Ishigaki, T., Muto, Y., & Baba, Y. (2005). Three-dimensional mathematical modeling of local scour. *Journal of Applied Mathematics*, *8*, 803–812.